Proximity effect between a high temperature superconductor and graphene

David Perconte

▶ **To cite this version:**

David Perconte. Proximity effect between a high temperature superconductor and graphene. Condensed Matter [cond-mat]. Sorbonne Université, 2018. English. NNT : 2018SORUS119 . tel-02926057

HAL Id: tel-02926057
https://theses.hal.science/tel-02926057

Submitted on 31 Aug 2020

HAL is a multi-disciplinary open access archive for the deposit and dissemination of scientific research documents, whether they are published or not. The documents may come from teaching and research institutions in France or abroad, or from public or private research centers.

L'archive ouverte pluridisciplinaire **HAL**, est destinée au dépôt et à la diffusion de documents scientifiques de niveau recherche, publiés ou non, émanant des établissements d'enseignement et de recherche français ou étrangers, des laboratoires publics ou privés.

THÈSE DE DOCTORAT
DE L'UNIVERSITÉ PIERRE ET MARIE CURIE

Spécialité : Physique

École doctorale : "Physique chimie des matériaux"

réalisée

à l'Unité Mixte de Physique CNRS-Thales

présentée par

David Perconte

pour obtenir le grade de :

DOCTEUR DE L'UNIVERSITÉ PIERRE ET MARIE CURIE

Sujet de la thèse :

Proximity effect between a high temperature superconductor and graphene

Effet de proximité entre un supraconducteur à haute température critique et du graphene

soutenue le 8 mars 2018, devant le jury composé de :

devant le jury composé de :

M.	Alexandre Bouzdine	Rapporteur
M.	Bernard Plaçais	Rapporteur
M.	Clemens Winkelmann	Examinateur
M.	Christophe Brun	Examinateur
M.	Pierre Seneor	Codirecteur de thèse
M.	Javier Villegas	Directeur de thèse

Contents

I – Introduction

The quest for novel materials with tunable physical properties is key for future electronic applications. For example graphene, a two dimensional crystal of carbon atoms, is an atomically thin and flexible conducting material. Graphene can be used to build a transistor because its electrical resistance is tunable with an external gate voltage. Young et. al. [**?**] studied a graphene based transistor type device, they showed that electrons in graphene are able to cross an energy step which they would be forbidden to pass in a metal. Another type of materials with tunable properties are superconductors. The pairing of electrons in superconductors allow these materials to transport an electrical current without any dissipation at low temperature, the discovery of a room temperature superconductor would have a major technological impact by reducing dramatically the energy consumption of electronic devices. Graphene and superconductor properties are very interesting and combining them together leads to new properties. For example, the reflection of an electron at the interface between a superconductor and graphene is very different from the reflection at a superconductor metal interface, this reflection is also tunable with an external gate voltage. D. Efetov et. al. [**?**] studied this phenomenon experimentally with a low temperature superconductor. In this thesis, we combine graphene with a high temperature superconductor in the search for new physical phenomena at their interface.

This thesis is a study of the conduction across the interface between a high-T_c superconductor and graphene. The outline of the thesis is the following.

In this first chapter, we review the theoretical concepts useful for the rest of the thesis. We describe: the high-T_c superconductor $YBa_2Cu_3O_7$ (YBCO) electrical properties, the superconducting proximity effect, the Andreev reflection both for a d-wave superconductor and for graphene, and the Klein tunneling of electrons in graphene. We then describe some key experiments combining superconductivity with graphene.

In the second chapter, we present the fabrication procedure of our YBCO/graphene junctions which includes oxygen irradiation of a YBCO substrate to obtain planar superconducting YBCO electrodes within an insulating matrix, transfer of a single sheet of Chemically Vapor Deposited (CVD) graphene and the fabrication of back and top gate used to vary the graphene's doping.

We study in the third chapter YBCO/graphene devices to understand the electrical current conversion occurring at the interface between a high-temperature superconductor (YBCO) and graphene. We measured oscillations of the interface conductance with gate voltage. We compare this experiment to a numerical model of the interface conductance and we interpret these interferences as Klein tunneling of superconducting pairs at the superconductor/graphene interface.

In the fourth chapter, we study the transport inside nanometric YBCO/graphene junctions. We observed on some devices a conductance modulation with gate voltage similar to the modulation expected for the transition between Andreev retro reflection and specular Andreev reflection, which is an unusual form of the Andreev reflection expected to occur in graphene or other gapless semiconductors. We also observed oscillations in the differential conductance as a function of both bias and gate voltages. These oscillations are related to

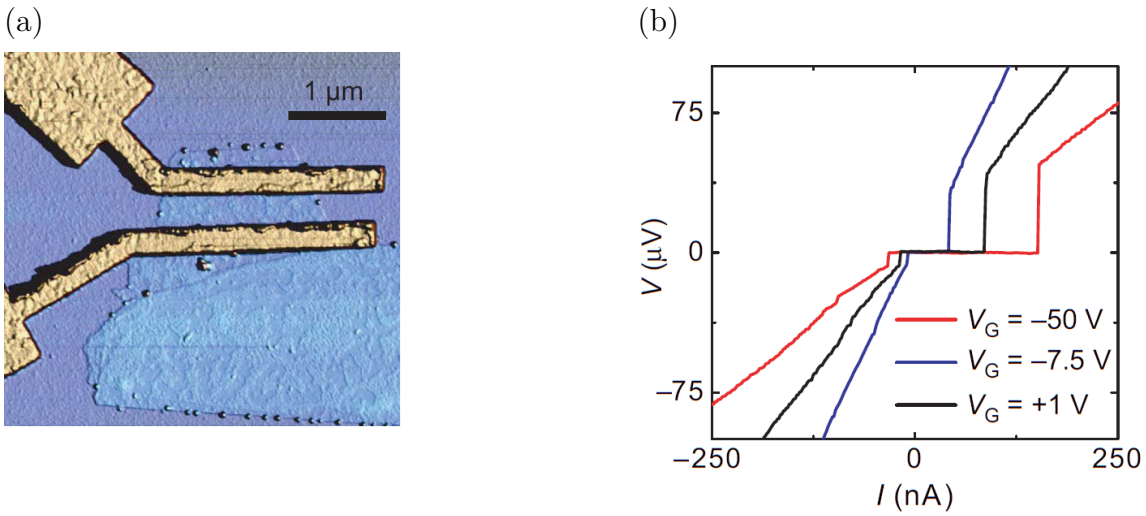

Figure I.1 – (a) Schematic of the device used in [?]. A graphene sheet is connected by two superconducting electrodes made of aluminum. (b) Several conductance curves at different gate voltages. The superconducting branch is the horizontal part of the I-V curve, the critical current shows a clear dependance as a function of the gate voltage. Images taken from [?].

particles interferences inside the graphene channel.

In the last chapter, we present an ongoing work on a fabrication method to obtain $Bi_2Sr_2CuO_{6+x}$ (BSCCO) ϕ-junctions.

I.1 Motivation

Experimentalists constructed the first graphene based Josephson junction [?] with aluminum shortly after graphene's isolation in 2005 [?]. The junction critical current is the maximum current the junction can sustain before becoming resistive. The critical current of the device studied in [?] is modulated by gate voltage and thus graphene doping as seen on figure I.1. The critical current evolution with magnetic field showed a regular Fraunhoffer pattern which is an indication of the current distribution uniformity in the graphene. This proved in a conclusive manner that the graphene between the aluminum electrodes becomes superconducting by proximity effect at low temperature. This proof of principle opened interesting perspectives for applications by adding to graphene one property it was lacking: superconductivity. It was followed by many fundamental studies [?, ?, ?, ?] exploring the interplay between superconductivity and other graphene's properties. We detail these studies in the next section I.3.4.

We chose to investigate high-T_c superconductor/graphene junctions, on which few works existed, because they offer key characteristics as compared with respect to low-T_c superconductor/graphene junctions. On the one hand, the large superconducting gap Δ of high-T_c superconductor ($\Delta = 20$ meV for YBCO compared to $\Delta = 1$ meV for $NbSe_2$ or $\Delta = 0.3$ meV

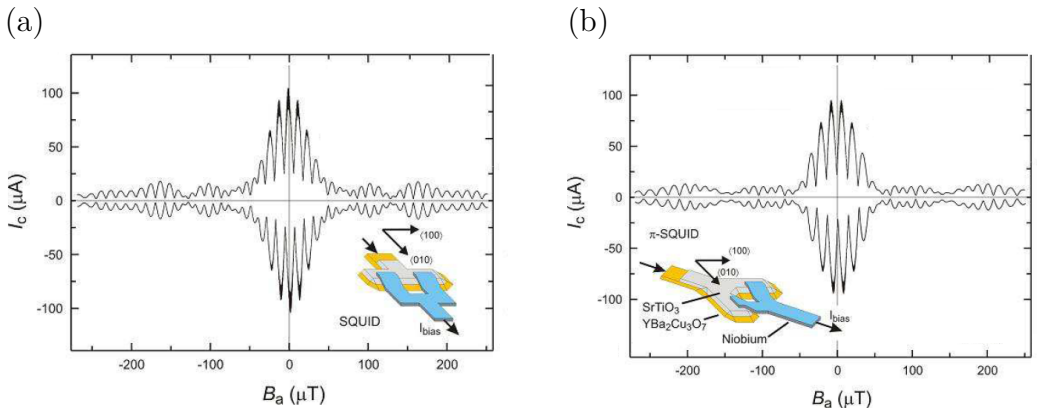

Figure I.2 – (a) Scheme of a standard SQUID and its critical current evolution as a function of the magnetic field, the critical current is maximum at zero magnetic field. (b) Scheme of a π-SQUID and its critical current evolution with a magnetic field, the critical current is minimum at zero magnetic field. Images taken from [**?**].

for Al) could allow to explore an unusual form of the Andreev reflection, the so-called specular Andreev reflection regime, which has been predicted specifically for graphene [**?**]. The specular Andreev reflection regime requires the graphene Fermi energy to be small $E_F < \Delta$ which can be achieved experimentally by tuning graphene carrier density with a gate. This condition $E_F < \Delta$ should be fulfilled everywhere in the graphene sheet such that the Fermi energy dispersion in the graphene sheet should also be small: $\delta E_F < \Delta$. This is very difficult to achieve, the smallest Fermi inhomogeneities obtained are typically of the order of 5 meV [**?**] which is still much bigger than the gap of Al for example ($\Delta = 0.3$ meV). On the other hand, the d-wave order parameters of high-T_c superconductors allow to build exotic Josephson junctions such as "ϕ-junctions " [**?**]. These junctions sustain a supercurrent without an external source as shown on figure I.2. A current is trapped inside the ϕ-junction when it is cooled down below T_c without magnetic field, this is due to the phase gradient of the superconducting wave function. This current at virtually no cost is very promising for applications using high-T_c superconductors.

However, it is challenging to obtain high-T_c superconductor/graphene Josephson junctions. On the one hand, because it is not possible to use the same fabrication technique as for low-T_c junctions. High-T_c superconductors are crystalline oxides which are usually grown with pulsed laser deposition on an adapted crystalline material at a high temperature and in an oxygen atmosphere. They cannot be deposited by metallic evaporation on graphene as it is usually done with low-T_c superconductors. On the other hand, obtaining transparent interfaces between superconducting oxides and graphene has proven challenging [**?**].

I.2 Key concepts for the proximity effect between graphene and a high-T_c superconductor

Below, we review the key concepts related to the proximity effect between graphene and a high-T_c superconductor: the $YBa_2Cu_3O_7$ (YBCO) properties, the Andreev reflection between a superconductor and a normal metal, the superconducting coherence length, the conductance of a superconductor/normal metal interface, the conductance of a d-wave superconductor/normal metal interface, the Andreev reflection at a superconductor/graphene interface.

When a superconductor is in contact with a normal material, the normal material might acquire superconducting properties if the interface between the two materials is sufficiently transparent. The transfer of the superconducting properties is mediated by the so-called Andreev reflection, which creates phase coherent electron/hole pairs in the normal material. This superconducting proximity effect can be theoretically described by the Eilenberger equations [**?**] which were simplified in the dirty limit by Usadel equations [**?**]. When the interface is perfect, the Andreev reflection is the only mechanism at the interface. When the interface is not transparent, normal electrons can be reflected from the interface without charge transfer into the superconductor. These phenomena are theoretically described by a phenomenological transport model from Blonder, Tinkham and Klapwijk [**?**]. We will see later that this work has been extended to the case of high-T_c superconductors by Kashiwaya et al. [**?**]. When the normal material is graphene, the Andreev reflection is modified as Cooper pairs can be split into the conduction and the valence band of graphene. Hence, the interface conductance is a fingerprint of this effect.

I.2.1 $YBa_2Cu_3O_7$ electronic properties

$YBa_2Cu_3O_7$ (YBCO) is an electronic oxide with a perovskite structure. The crystallographic lattice is orthorombic as shown on figure I.3. The YBCO crystal consists of the stacking of CuO planes, BaO_2 planes, CuO_2 planes and Y^{3+} planes. YBCO is grown by pulsed laser deposition in our lab, the pulsed laser deposition technique is explained in chapter 2. The orthorhombic structure is grown at a temperature above 680 °C for which the orthorhombic lattice structure is more stable thermodynamically.

YBCO has a superconducting transition temperature controlled by its oxygen content. YBCO superconducting transition temperature has a maximum of 93 K for a hole doping of 0.15 as shown in [**?**] and on figure I.4. Decreasing the oxygen content of YBCO decreases its superconducting critical temperature and for doping below 6.2 YBCO is an insulator. As we will see, our YBCO films lose oxygen during our device fabrication reducing the YBCO critical temperature from its pristine value of 85-90 °C until 60-70 °C.

The YBCO superconducting coherence length ξ is about 2 nm in the horizontal plane and 0.4 nm in the vertical direction. The superconducting pairing interaction has a d-wave symmetry, as it has been shown by phase sensitive measurement in [**?**]. Kirtley et. al. [**?**] measured the spontaneous magnetization of a two junction ring of Nb and YBCO. The

(a) (b)

Figure I.3 – (a) $YBa_2Cu_3O_7$ crystallographic structure. (b) $YBa_2Cu_3O_7$ superconducting order parameter.

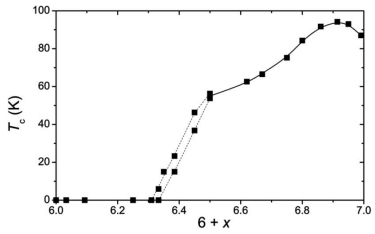

Figure I.4 – $YBa_2Cu_3O_{6+x}$ critical temperature as a function of the hole doping x. Image taken from [**?**]

YBCO d-wave order parameter imposes a phase gradient to the electronic wave function across the ring. This phase gradient induces a spontaneous current which was detected using a superconducting quantum interference device.

I.2.2 Andreev reflection at a superconductor/metal interface

The mechanism by which a current carried by normal carriers (electrons or holes) is converted into a supercurrent at the interface between a normal material and a superconductor is the Andreev reflection [**?**] depicted in figure I.5. This process can be described in the following way: when an electron from the normal material impinges on the superconductor, it can either be reflected as an electron if there is scattering at the interface or it can be transmitted as a Cooper pair. In the second case, a hole has to be reflected back into the normal material due to the Cooper pair transfer and charge conservation. By momentum conservation along the direction of the interface, the hole traces back the same path that was first traced by the incoming electron. The electronic trajectories are depicted in figure I.6, where the path followed by the incoming electron is in red and the path followed by the reflected hole is in green.

The Andreev reflection process implies a geometrical condition between incident angle θ_i and reflected angle θ_f: $\theta_i = -\theta_f$. Magnetic field focusing of electronic trajectories was

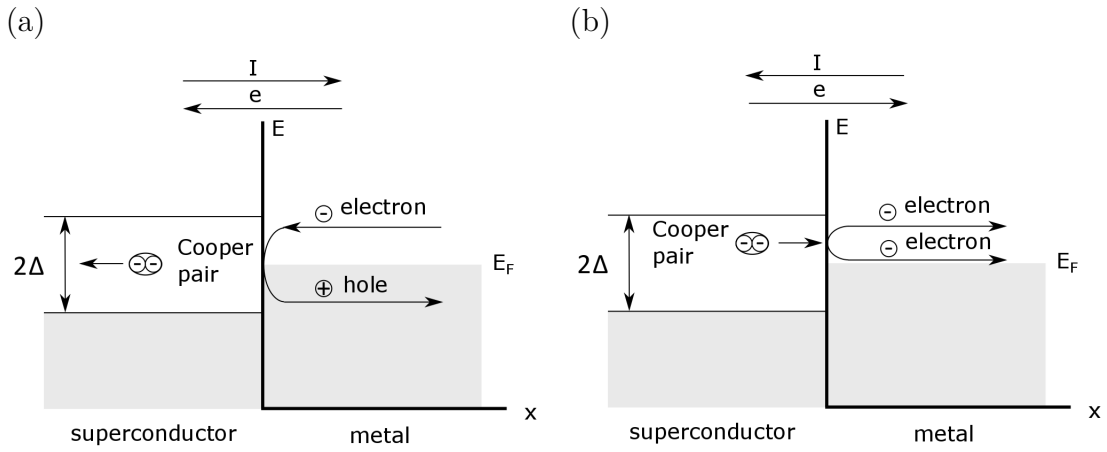

Figure I.5 – Schematic of the Andreev reflection process. (a) The current is flowing from the left to the right, therefore the incident electron comes from the right. This is the case for all figures in this chapter (except here in (b)). An electron impinging on a superconductor creates a Cooper pair inside the superconductor and a hole is reflected in the metal. (b) The current is flowing from the right to the left, therefore the incident electron comes from the left. In the same manner, if a Cooper pair impinges on a normal material it can be split into two electrons propagating inside the normal metal. The propagation of this correlated pair transport the superconducting properties in the metal and leads to a supercurrent in the case where the metal is sandwiched between two superconductors.

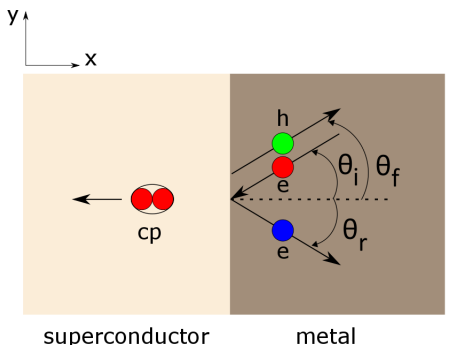

Figure I.6 – Scattering mechanisms occurring at a superconductor/metal interface. An electron (in red) impinges on a superconductor. If the interface is opaque, the electron is specularly reflected on the interface (in blue). If the interface is transparent, the electron creates a Cooper pair inside the superconductor and a hole (green) is retro reflected in the metal. This is the Andreev reflection.

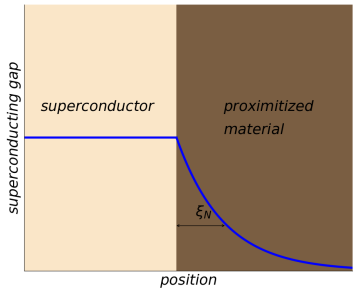

Figure I.7 – The superconducting order parameter extends into a normal material by proximity effect with a superconductor. The order parameter is also weakened inside the superconductor (not shown), this happens on the length ξ_S with $\xi_S \sim 3$ nm in the case of YBCO.

used to probe the scattering angle of electrons from a metal to a superconductor [**?**, **?**]. The conductance as a function of magnetic field was measured before and after a superconductor was deposited at the interface of the normal material. Before the deposition, the conductance showed resonances corresponding to electronic trajectories being specularly reflected at the normal metal boundary. After deposition, the conductance showed the appearance of a new resonance corresponding to electronic trajectories being Andreev reflected at the normal metal superconductor boundary.

I.2.3 Coherence length

The length scale governing the proximity effect is the superconducting coherence length in the normal material ξ_N. The coherence length inside the superconductor ξ_S governs the size on which superconductivity is affected or suppressed, for example by a defect. In a type-II superconductor, the vortex which appear inside the superconductor when a magnetic field is applied have a radius of the order of ξ_S. In the normal material, there is also a superconducting coherence length ξ_N which indicates on which distance the Cooper pairs can propagate into the material without losing their coherence as shown on figure I.7. This length corresponds to the distance traveled by the pairs during a dephasing time τ. The dephasing time τ is related to an energy by $\tau = \hbar/E$. This energy corresponds to the largest energy between the thermal noise $E = k_B T$, the superconducting gap $E = \Delta$ or the exchange field if the normal material is ferromagnetic [**?**]. In a ballistic material, the coherence length is given by

$$\xi_N = v_F \tau$$
$$\xi_N = \hbar v_F / E.$$

In a diffusive material, the coherence length is given by

$$\xi_N = \sqrt{D\tau}$$
$$\xi_N = \sqrt{\hbar D / E}.$$

In diffusive graphene, $D = l_{mfp} v_F / 2$ with l_{mfp} the mean-free path in graphene. We will see later that the coherence length ξ_N increases with the mean free path and superconductivity

survives on a longer scale when the material is cleaner. In the case of our graphene YBCO junctions, the graphene size is always larger than the mean free path such that we are in the diffusive limit and the energy is dominated by thermal contribution, thus the coherence length is given by

$$\xi_N = \sqrt{\hbar D/k_B T}.$$

A thin layer of metal is often inserted in experiments to improve the electrical contact between a superconductor and a normal metal, for example between a superconductor and a carbone nanotube [**?**], or a semiconductor nanowire [**?**] or graphene [**?**]. If this layer is thin enough, it can be considered to be a superconductor itself due to the proximity effect. In the case of a d-wave superconductor, the metallic layer has to be smaller than the electronic mean free path. This effect cannot be described by a mean field theory level, it requires the Eilenberger equations [**?**] which are based on the Green function formalism. A simplification of this theory obtained by averaging over distances of the order of the mean free path was done by Usadel [**?**].

I.2.4 Effect of the transparency: Blonder-Tinkham-Klapwijk model

It is complicated to take into account the interface transparency in order to calculate a superconductor/metal interface conductance. This was done phenomenologically by Blonder, Tinkham and Klapwik (BTK model) in [**?**]. The conductance is calculated by matching the electronic and Cooper pairs wave function at the interface, a mismatch between the wave functions is described by a parameter Z which represents scatterers at the interface. A low Z value corresponds to a transparent interface and a large Z value correspond to an opaque interface. The interface differential conductance G can be related to the normal state conductance G_N, and to the reflection r^2 and Andreev reflection r_A^2 probabilities:

$$G = G_N(1 - r^2 + r_A^2).$$

As shown on figure I.8a, the effect of a decrease of the interface transparency is a decrease of the conductance. This is due to an increase of normal carriers reflection at the interface on impurities or scatterers. We recognize a signature of the Andreev reflection on figure I.8b: the conductance is twice as high below the superconducting gap Δ than above Δ when the interface is fully transparent (Z = 0). Indeed, one electron (charge e) in the normal metal produce a Cooper pair (charge 2e) in the superconductor in the Andreev reflection process. In the transparent case (Z = 0), if there were a superconductor on the other side of the normal metal, there could be a supercurrent traversing the junction. When the interface is fully opaque (high Z), the conductance is much smaller below the superconducting gap than above. This corresponds to a tunneling regime. In between these two extreme cases, there is a gradual decrease of the subgap conductance while the conductance at the superconducting gap stays constant. The normal material band structure is not considered in this phenomenological description as long as the normal material is conducting. Experimental observations of the conductance doubling in the transparent regime has been challenging. One needs a very good contact between the metal and the superconductor to be in the low Z limit of the BTK formalism. For instance, it has been measured in two dimensional electron gas connected to Al [**?**] as seen on figure I.9.

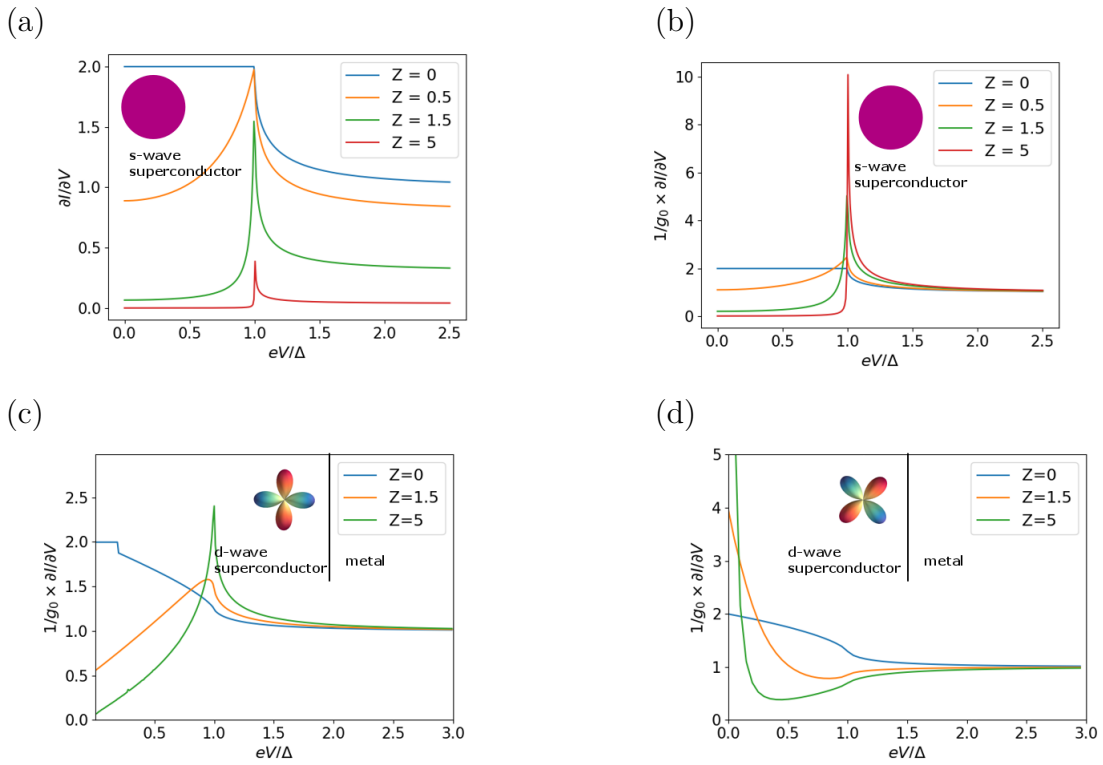

Figure I.8 – Differential conductance of a superconductor/normal metal interface for different interface transparencies. A low value of Z corresponds to a transparent interface, a high value of Z corresponds to an opaque interface. (a-b) Case of an s-wave superconductor. For (b-d) the differential conductance is normalized with respect to its normal state value which corresponds to the high bias limit where the transport is governed by normal charge carriers. (c) Case of a d-wave superconductor with $\alpha = 0$, the order parameter nodes are orthogonal to the interface. The result is similar to the s-wave case. (d) Case of a d-wave superconductor with $\alpha = \pi/4$. At high transparency (Z = 0) the conductance is similar to the s-wave case shown on figure I.8b. At low transparency (Z = 5) a peak at zero bias reflects the formation of bound states at the interface.

I.2.5 High-T_c superconductor/normal metal interface

The pairing symmetry of the high-T_c cuprates was an open question for many years. It was believed that this symmetry would discriminate between different theories and help to understand the origin of high-T_c superconductivity. C.-R. Hu [**?**] showed that a d-wave order parameter symmetry would lead to bound states at zero energy at the interface between a d-wave superconductor and a normal material. If the interface is not transparent, particles will indeed be reflected multiple times before crossing the interface. The particles acquire a phase $\arccos(E/\Delta)$ when being Andreev reflected from the superconductor. In the d-wave case, the phase acquired by an electron and a hole can cancel leading to an effectively transparent interface. As shown on figure I.10, electrons and holes impact the superconductor with different angles θ_e and θ_h. We note $\theta = \theta_e = -\theta_h$ in the following. Electrons and holes

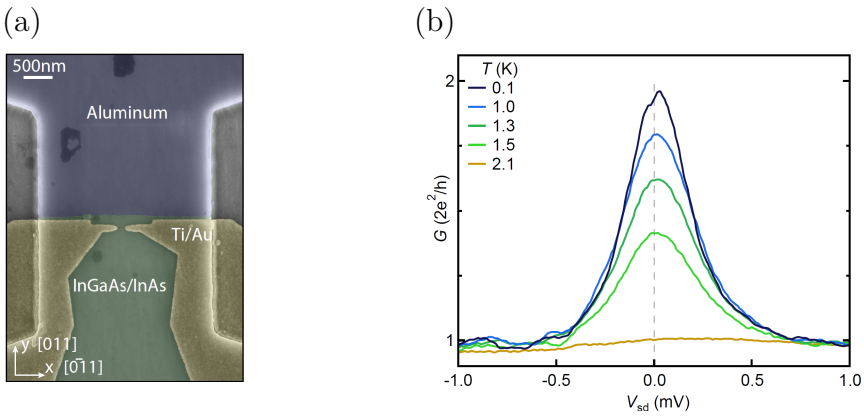

Figure I.9 – (a) Electron microscope image of the device used in [?], a two-dimensional electron gas of InGaAs/InAs is connected to a superconductor (Al) trough a constriction. (b) Differential conductance as a function of the temperature, the conductance measures the superconductor/two dimensional electron gas interface. In the superconducting state (low bias, low temperature) the conductance is doubled compared to the normal state (high bias or high temperature) as expected from the Blonder Tinkham Klapwijk theory. Images taken from [?].

are thus sensitive to the angular dependance of the order parameter $\Delta(\theta)$. The total phase acquired by the particles on a round-trip is:

$$\varphi = 2L(k_e - k_h) + \arccos(E/\Delta(\theta)) + \arccos(E/\Delta(-\theta))$$

which reduces to

$$\varphi = \arccos(E/\Delta(\theta)) + \arccos(E/\Delta(-\theta))$$

when the barrier width L tends to zero. The order parameter has to change sign with the direction θ in order to have constructive interferences inside the normal barrier at zero energy: $\varphi = 0$ if $\Delta(\theta) = -\Delta(-\theta)$. These constructive interferences correspond to an effectively transparent interface. In particular, there is no constructive interferences (bound states) at zero energy in the s-wave case ($\Delta(\theta) = \Delta(-\theta)$), and they are bound states at zero energy in the d-wave case ($\Delta(\theta) = -\Delta(-\theta)$ if the superconducting order parameter node is orthogonal to the interface). The constructive interference results in a peak in the differential conductance of the superconductor normal metal structure.

Kashiway et al. [?, ?] refined the Blonder, Tinkham, Klapwijk theory to calculate the normal reflection r^2 and Andreev reflection probability r_A^2 as a function of the transparency Z and of the order parameter $\Delta(\theta)$. The differential conductance of the interface between a d-wave superconductor and a metal is given by the general formula $G = G_N(1 - r^2 + r_A^2)$ (as in the s-wave case). The bound states at the interface between this superconductor and a normal metal appear as a Zero Bias Conductance Peak (ZBCP) in the differential conductance of the structure as shown on figure I.8d. There is no peak at zero bias when the interface is orthogonal to the superconducting node (figure I.8c) because the phase acquired

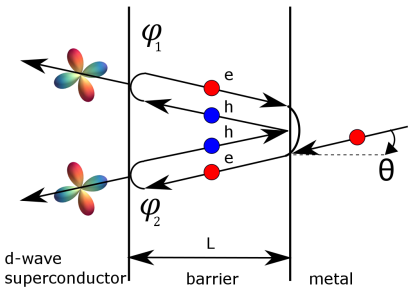

Figure I.10 – Bound states at the interface between a superconductor and a normal material with a thin interface in between. Electrons (red) and holes (blue) see a different order parameter while being reflected by a d-wave superconductor: $|\Delta|cos(2\theta+\alpha)$ and $|\Delta|cos(-2\theta+\alpha)$ respectively. Therefore, they do not acquire the same phase when being Andreev reflected. The phases φ_1 and φ_2 can be opposite in which case there is a bound state at zero energy in the limit of an infinitely thin barrier.

by the electrons and holes are the same after being Andreev reflected. There is however a peak around the superconducting gap which corresponds to bound states. The doubling of the conductance at zero bias is only observed for a transparent interface (Z=0). The peak height increases as the interface transparency decreases [**?**].

I.2.6 Andreev reflection at a graphene/superconductor interface

The Andreev reflection is modified in graphene. The band crossing at the Dirac point in the graphene band structure affects the conductance of a superconductor/graphene interface conductance [**?**]. When an electron impinges on the superconducting interface, it can be either reflected in which case no current crosses the interface. Or the electron can create a Cooper pair on the superconducting side, in which case a hole has to be reflected onto the graphene just as in the metallic case. Now contrary to the metallic case, the hole can be in the conduction band if the graphene is doped as depicted on figure I.11a and I.11b ($E_F > \Delta$) or it can be in the valence band if the graphene is close to the charge neutrality point as depicted on figure I.11c and I.11d ($E_F < \Delta$). If the hole is in the conduction band as in the metallic case, it will trace back the trajectory followed by the incoming electron (figure I.11b). If the hole is in the valence band, it will be specularly reflected from the interface compared to the incoming electron also by momentum conservation (figure I.11d). For intermediate doping, the angle of the reflected hole is given by the Fermi energy and the bias voltage as shown on figure I.11e. The relation between the incoming electron angle with the interface θ_i and the hole trajectory angle with the interface θ_f is then given by a Snell-Descartes type law:

$$(eV + E_F)\sin\theta_i = (eV - E_F)\sin\theta_f.$$

In particular, when the incoming electron energy eV is equal to the graphene Fermi energy E_F, there is no incoming angle for which this relation is satisfied, it is the analogue of total reflection in optics. Therefore no electron can be reflected and the conductance has to vanish at the point $eV = E_F$ as shown on figure I.12.

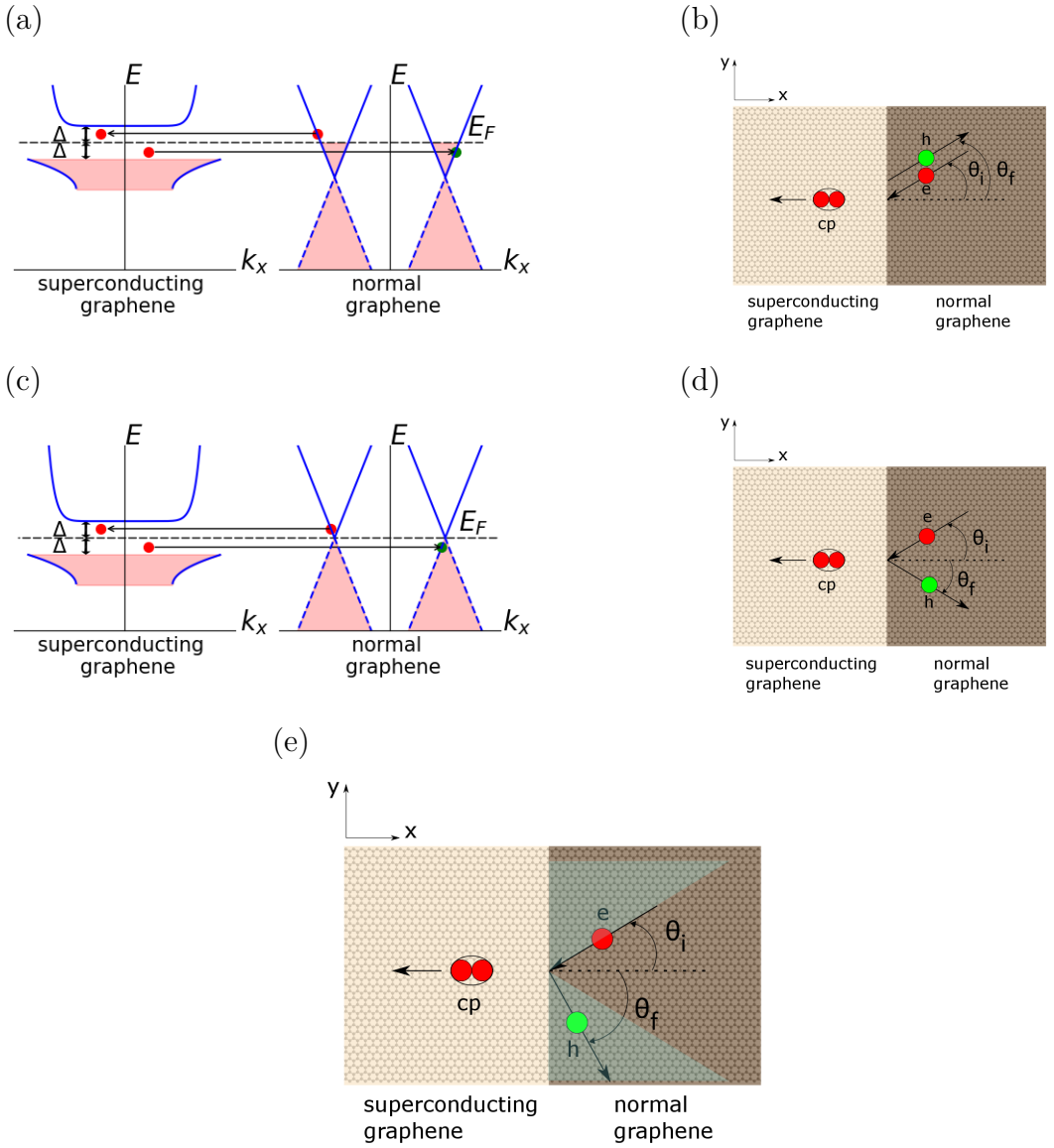

Figure I.11 – Andreev reflection occuring at a superconductor/graphene interface. When an electron coming from the graphene (red) impinges on the superconductor interface it can either be reflected as an electron or it can create a Cooper pair inside the superconductor. In the second case, a hole (green) has to come back on the graphene side. (a) The hole is in the same band as the incoming electron at high graphene doping. (b) The hole is thus retro reflected. (c) and (d) Specular Andreev reflection. (c) The hole is in the valence band when the graphene doping is low. (d) The hole is thus specularly reflected. (e) For intermediate doping, the hole reflection angle is fixed by equation I.9. The blue shaded region corresponds to the angle allowed by equation I.9.

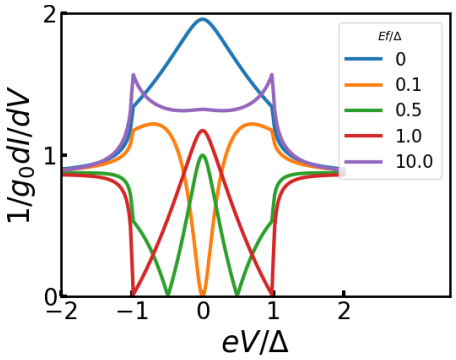

Figure I.12 – Differential conductance of an s-wave superconductor/graphene interface for different value of the graphene Fermi energy E_F. When $E_F < \Delta$ specular Andreev reflected particles contribute to the transport. In that case, the conductance vanishes at $eV = E_F$. If $E_F > \Delta$, the electrons are either reflected or Andreev retro-reflected at the interface.

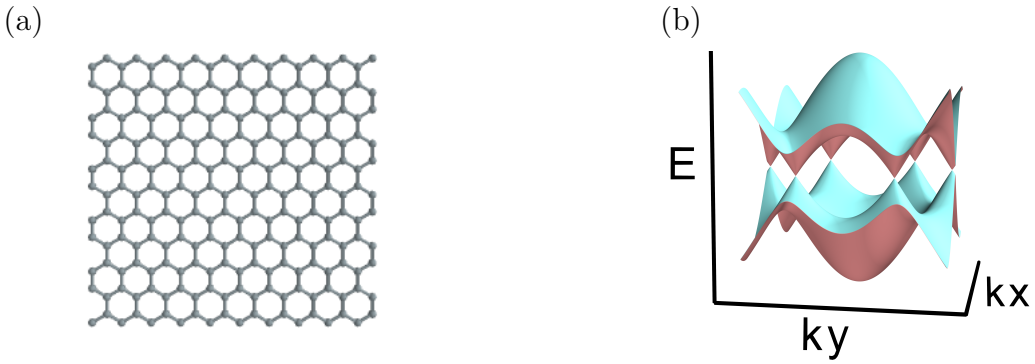

Figure I.13 – (a) Graphene is a two dimensional hexagonal lattice of carbon atoms. We use single layer graphene in this thesis. (b) Graphene band structure in the tight binding approximation as calculated by Wallace [**?**].

To conclude, a simple phenomenon such as the Andreev reflection becomes more sophisticated when it happens between a high-T_c superconductor and graphene.

I.3 State of the art

I.3.1 Electronic properties of graphene

Graphene is a two dimensional hexagonal array of carbon atoms, such an array looks like a honeycomb as shown on figure I.13a. Graphene usually refers either to a single layer of this array or to the superposition of a few layers of this array [**?**, **?**]. In the following, we will only use single layer graphene which we will refer to as graphene without possible confusion. The graphene's band structure was calculated in 1947 by Wallace [**?**] using a tight binding approximation with an empirical value for the hopping parameter t. The energy dispersion

is:

$$E(\vec{k}) = \pm t|1 + e^{i\sqrt{3}a/2(k_x+\sqrt{3}k_y))} + e^{i\sqrt{3}a/2(-k_x+\sqrt{3}k_y))}|,$$

t is the tunneling amplitude between nearest neighbors, $t \sim 2.7\ eV$ from ab initio calculations, a is the distance between carbon atoms $a \sim 142\ pm$, $\vec{k}$ is the electronic wavevector. The energy dispersion is shown on figure I.13b, it consists of two bands touching at six points in the first Brillouin zone. The graphene's density of states vanishes when the conduction band is filled, this can be achieved by tuning graphene electronic density externally by using the field effect. The graphene's band structure is thus the one of a gapless semiconductor. The band touching points are called Dirac points. The band structure is well approximated by a cone close to the Dirac points where the energy dispersion is linear:

$$E(\vec{k}) \sim \pm\hbar v_f|\vec{k}|.$$

This approximation is valid up to energy of the order of 1 eV. This energy dispersion relation is called the Dirac equation because it is the same as for relativistic electrons or photons in vacuum. There is thus an analogy between electrons in graphene and photons, for example there is an analogue of Snell-Descartes law for the transmission of electrons in graphene between two regions of different electrical potential. Phenomena predicted to occur in high energy physics have been observed in graphene, for example Klein tunneling [**?**, **?**, **?**]. The electron velocity is independent of the wavevector:

$$v = \frac{1}{\hbar}\frac{\partial E}{\partial k}.$$

This velocity is about 1×10^6 m.s^{-1} in graphene.

I.3.2 Graphene transport

Graphene carriers' concentration can be controlled with an external capacitive gate. This possibility generated much interest [**?**, **?**, **?**] as it is the basic property of a transistor, unfortunately the finite value of graphene conductivity at the charge neutrality point has prohibited such an application up to now. The experimentally measured graphene conductivity at the charge neutrality point was much higher than the conductance value calculated in the case of a perfect ballistic sheet. The reason is that the transport was limited by graphene Fermi energy's inhomogeneities [**?**]. These inhomogeneities might be induced by resist residues or by graphene corrugation. Indeed, graphene doping depends on its electrical environment because a difference in work function between two materials leads to a charge accumulation at their interface. New techniques such as the encapsulation of graphene between hexagonal boron nitride sheets or the suspension of graphene, allow to obtain a ballistic transport on much longer scale. In these devices, the mobility can be as high as 500 000 cm^2.(V.s)$^{-1}$ in CVD graphene [**?**] and in encapsulated graphene [**?**].

I.3.3 Klein tunneling

The dispersion relation of both graphene (equation I.11) and photons is linear, such that the relation between the angles of an incident electron θ_i and of the refracted electron θ_f at a

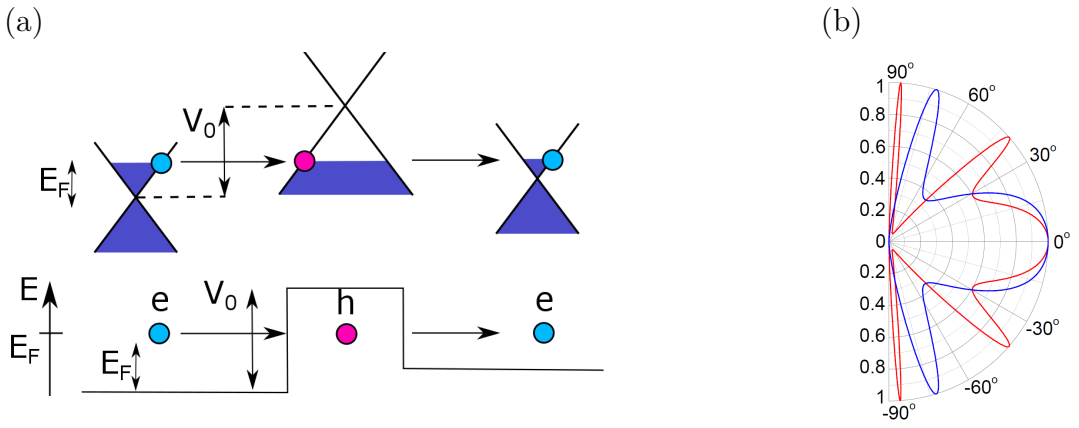

Figure I.14 – (a) Electrons in graphene can tunnel through very high potential step, contrary to the metallic case where the tunneling probability decays exponentially with the step height. They are electronic conducting states at all energies in graphene. When an electron enters a high energy step (left panel), it can be converted into a hole (central panel) which travels through the step without attenuation, this hole can be converted into an electron when exiting the potential step (right panel). This process is called Klein tunneling by reference to an analog effect in high energy physics studied originally by O. Klein [**?**]. (b) Transmission through the potential step as a function of the incident angle. The transmission is perfect at normal incidence, blue and red curves correspond to different potential height V_0. Image taken from [**?**].

pn interface in graphene is "identical" to Snell law in optic:

$$k_i sin(\theta_i) = k_f sin(\theta_f),$$

with k_i, k_f the Fermi wavevectors in the p and n regions respectively, equivalently:

$$E_{F,i} sin(\theta_i) = E_{F,f} sin(\theta_f),$$

with $E_{F,i}$, $E_{F,f}$ the Fermi energies in the p and n regions respectively. The transmission probability across a symmetric pn junction is given by:

$$T \sim \exp^{-\pi k_F d sin^2 \theta_i},$$

with k_F the Fermi wave-vector, d the junction width.

Klein tunneling is the mechanism by which electrons cross an energy barrier in graphene pnp junctions [**?**, **?**, **?**]. O. Klein studied how relativistic electrons can cross an energy barrier. The equation of motion of relativistic electrons is the same Dirac equation (equation I.11) that describes charge carriers in graphene. This is the reason why the crossing of a potential step in graphene is also called Klein tunneling. The transmission probability across an energy step (pnp) in graphene is not exponentially suppressed with barrier height. There are indeed available states at all energy in graphene contrary to the metallic case as shown on figure

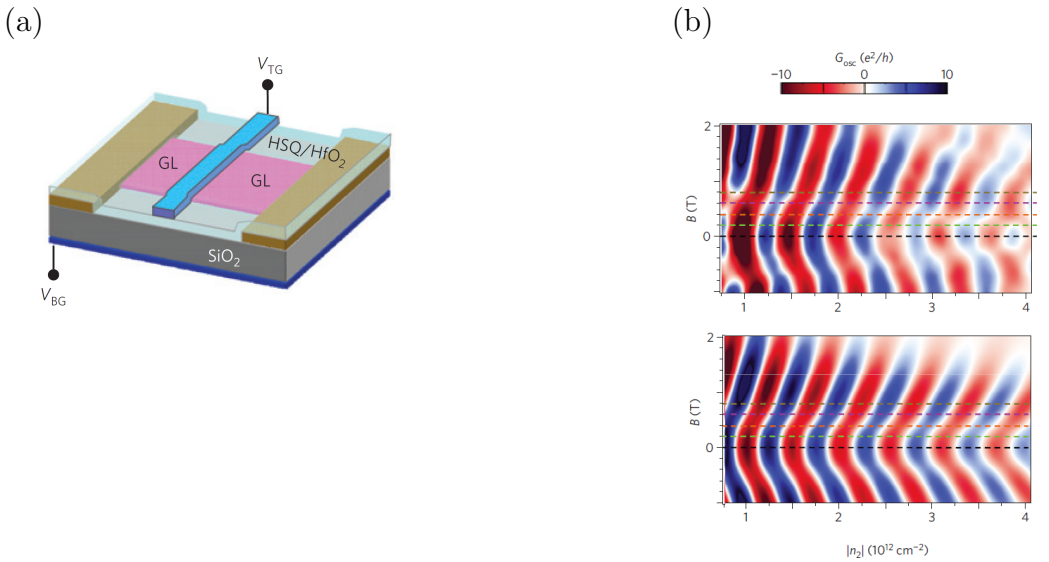

Figure I.15 – (a) Schematic of the device used in [**?**] to study Klein tunneling in graphene. An electrostatic gate of 20 nm width creates a tunable potential step in graphene. (b) Conductance curves as a function of magnetic field and graphene doping (top experiment, bottom numerical simulation). Several conductance curves at different magnetic field. The electron trajectories are closed loops in k-space which encircle the origin only at high magnetic field. This results in a non-trivial Berry phase which can be seen as a global phase shift between high and low magnetic field. Images taken from [**?**].

I.14. Klein tunneling through an npn region is analogous to the transmission of photons through an optical cavity. The resonance condition for electrons in graphene is given by:

$$2k_F w = 2\pi N$$
$$2\sqrt{\pi n} w = 2\pi N,$$

with k_F the Fermi wavevector, w the barrier width, n the carrier density in the barrier, N the number of crossings of the barrier. The resonance condition and thus the cavity resistance are modulated with graphene carrier density.

Klein tunneling has been studied in [**?**]: a top gate of 20 nm width defines a potential step smaller than the electronic mean free path (100 nm) on the graphene sheet. The interferences between the different electronic trajectories inside the potential step result in conductance oscillations of the graphene npn junction as a function of the carrier density as shown on figure I.15.

One of the first "electron optics" experiment in graphene [**?**] used magnetic field focusing to determine the probability of electron reflection at the graphene interface. The magnetic focusing principle (through a pn junction) is illustrated on figure I.16a. An emitter sends electrons which are deflected by a magnetic field towards the graphene interface, depending on the electron position and on the reflection angle, the electrons are then collected or not

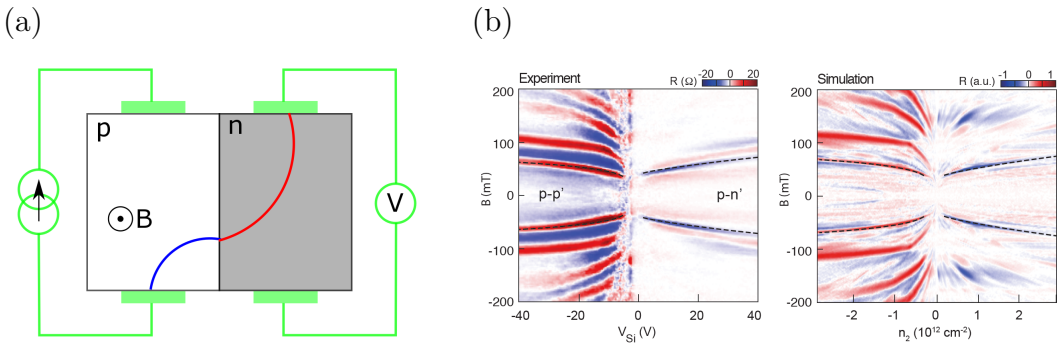

Figure I.16 – Experiment used to study the transmission probability and transmission angle across a graphene p-n junction [?]. (a) Electron (blue) and hole (red) trajectories at the interface between graphene regions with different doping. Compared to optics, the refraction is negative when the two regions have opposite polarity (p-n junction). (b) Experimental and simulation resistance mapping as a function of magnetic field and bias voltage. The resonances correspond to the focusing of the trajectories from the emitter to the collector. The dashed black lines correspond to the resonance condition calculated with equation I.13. Images taken from [?].

by another electrode. Depending on the magnetic field, electrons have to bounce once, twice or more at the graphene interface before reaching the collector. The ratio between the resistance values for one, two or more bounces is proportional to the reflection probability. Here, between 20% and 50% of the electrons are specularly reflected by the interface.

Graphene p-n junctions and Klein tunneling can be studied with these "electron optics" methods. Chen et al. [?] fabricate a graphene Hall bar around a p-n junction as shown on the figure I.16. The authors of [?] extract the transmission of the junction dependance on the incident angle from the resistance when the magnetic field focuses the electrons from the emitter to the collector. The incident angle θ_i is known from the magnetic field and doping value in the first region. The measured transmission follows closely the theoretical equation I.15.

The resistance variations between emitter and collector as a function of the magnetic field are a fingerprint of the transmission through the junction. This is used to verify the equation I.13. The Fermi wave-vector is related to the doping: $k = \sqrt{\pi n}$, such that k_i and k_f are experimentally known. The refraction angle θ_f is obtained by mapping out the resonance condition as a function of doping in the second region.

I.3.4 Graphene/superconductor junctions

The interest in superconductor/graphene system is very vivid, many excellent studies have been carried out and published already. Without being exhaustive, we describe the most striking one hereafter.

The tunability of the Andreev reflection regime with gate voltage [?] is a motivation to

study experimentally [?, ?, ?, ?] graphene in contact with a superconductor. The prospect of controlling the reflection angle of the Andreev reflected hole with gate voltage shown on figures I.11 would be a useful tool for "electron optics" experiments. Thanks to bilayer graphene's low Fermi energy dispersion ($\delta E_F < 1$meV) and its gapless band structure, Efetov et al. [?] showed conclusive evidence of the unusual specular Andreev reflection by performing measurements of the interface conductance of a graphene bilayer in contact with $NbSe_2$. The agreement between their theoretical model and their measurement shown on figure I.17b is a strong evidence for the observation of specular Andreev reflection.

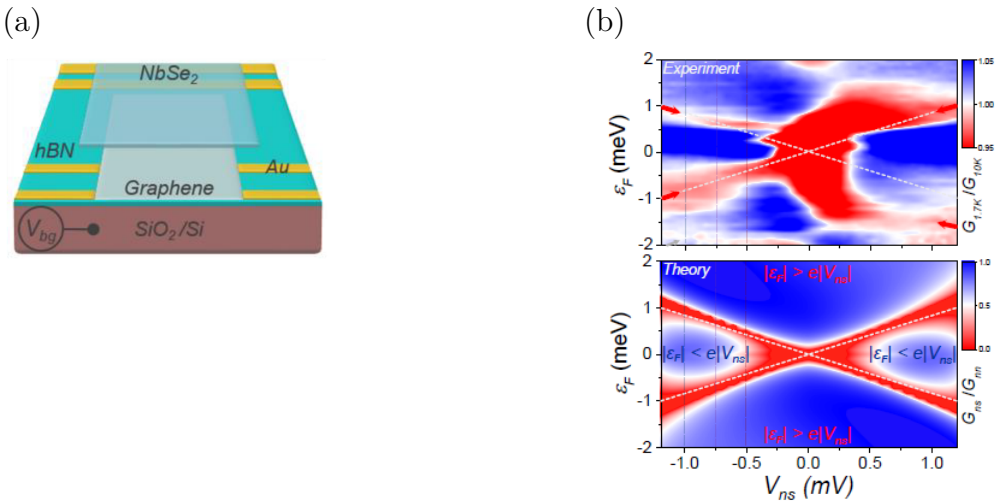

Figure I.17 – (a) Schematic of the device used in [?], a bilayer graphene sheet is in contact with the exfoliated superconductor $NbSe_2$. The device geometry allows to measure the interface conductance in a 4-points configuration. (b) Conductance map as a function of bias voltage and gate voltage, top pannel experiment, bottom pannel theory. The central region corresponds to the specular Andreev reflection regime. Images taken from [?].

Many studies exist on conventional superconductor/graphene structure [?, ?, ?, ?, ?, ?, ?]. An experiment probed recently the density of states of graphene between two superconductors [?]. Allen et al. [?] studied the current distribution in the graphene sheet as a function of gate voltage. This distribution was extracted from the critical current behavior as a function of magnetic field. Edge states are present at graphene boundaries due to band bending. The authors of [?] showed that bulk states dominate the conduction far from the Dirac point, but that edge states dominate the transport close to the Dirac point. In the supplementary information (section S9) of [?], similar Fraunhoffer patterns as in [?] are shown for different dopings. They are relatively similar but the authors argue that the current distribution in the device is uniform for all graphene doping. The transport in [?] could be dominated by charge inhomogeneities around the Dirac point as shown in [?].

The current distribution evolution has an even more dramatic effect on the superconductivity when a high magnetic field is applied. The authors of [?] could study this regime thanks to their high graphene mobility. Their device shows an unusual reentrance of super-

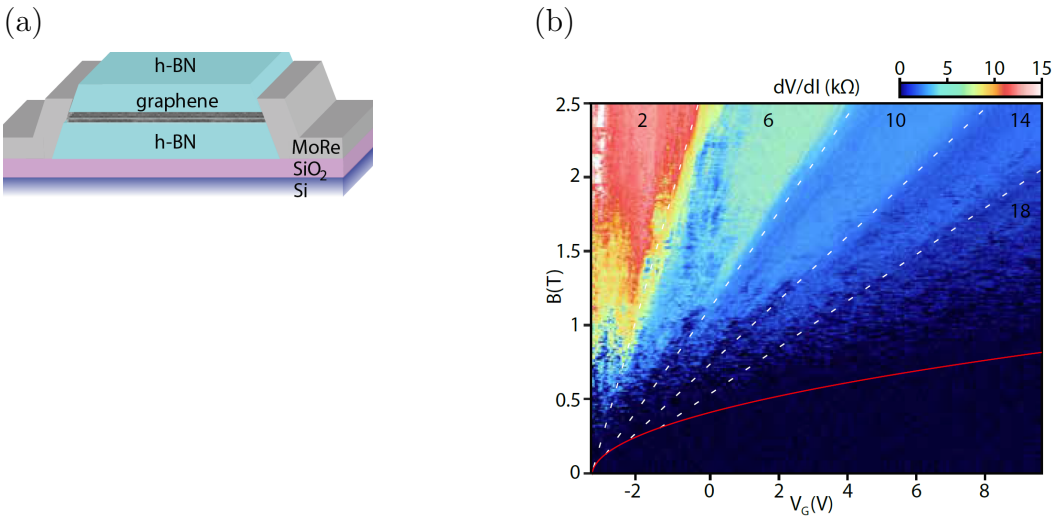

Figure I.18 – (a) Schematic of the device used in [**?**], graphene is encapsulated between boron nitride and laterally connected with superconducting electrodes in MoRe. (b) Differential resistance of the device as a function of gate voltage and magnetic field. In the quantum Hall regime (above the red line) re-entrance modulations of the superconductivity appear. Images taken from [**?**].

conductivity at high magnetic field while the usual Fraunhoffer pattern is observed at low magnetic field. This is due to diffusive conduction along the graphene edges where cyclotron orbits are deflected. The authors of [**?**] reproduced the same effect but they more particularly focused their study on the interplay between the superconductivity and the quantum Hall effect. Since there are no states in the bulk of the sample in the quantum Hall regime (QH), the critical current such a sample can sustain is smaller than the same sample in the classical Hall regime. Indeed the normal state resistance is higher in the quantum Hall regime thus the critical current is smaller. Hybrid electron hole modes have to couple the superconducting electrodes in the QH regime because only the edges are conducting. The paper focuses on one specific region of gate voltage and magnetic field, however they show a very interesting and extensive map (figure I.18b) of the resistance as a function of the magnetic field and gate voltage.

A recent paper [**?**] studied the same phase diagram region where superconductivity coexists with quantum Hall effect in graphene. They study a previously predicted phenomenon called the crossed Andreev reflection. Their system consists of a superconductor of dimension comparable to the superconducting coherence length ξ contacting graphene on the edge. In the crossed Andreev conversion, an electron is converted into a Cooper pair inside the superconductor and a hole is reflected on the other side of the superconductor. The signature of this phenomenon is a negative resistance in a non-local measurement which was observed by the authors of [**?**].

The authors of [**?**] used an original geometry consisting of an array of Josephson junctions to study how the superconductor to metal transition can be driven by temperature,

magnetic field and disorder. The proximity effect between two superconductors depends on the resistance of the normal part between them. Their system consists of an array of superconducting disks deposited on top of graphene, so that the gate voltage tuned their system from metallic to superconducting through a percolation of isolated superconducting region.

Few studies exist on the proximity effect between a high-T_c superconductor and graphene because it is challenging to achieve good electrical contacts between graphene and a high-T_c superconductor [**?**]. The YBCO graphene devices studied in [**?**] show a tunneling behavior. The most recent high-T_c superconductor/graphene study is an experimental investigation by scanning tunneling spectroscopy of the order parameter induced in graphene when deposited on the superconductor $Pr_{2-x}Ce_xCuO_4$ (PCCO) [**?**]. They show that the density of states of graphene on PCCO is different from both the density of states of graphene alone and the density of states of PCCO alone. The orientation of the superconductor with respect to the graphene crystallographic axes favors theoretically p-wave superconductivity, this is consistent with the conductance spectra presenting zero bias conductance peaks. However it is difficult to know if the scanning tunneling microscope probes part of the density of states of the superconductor beneath the graphene. We do not probe the density of states in the proximitized graphene in this thesis, instead we study the transport across a high-T_c superconductor/graphene interface.

II – Sample fabrication and characterization

We present in this chapter the general fabrication procedure of our electrical devices. We describe the fabrication of planar YBCO/graphene junctions: we start by patterning superconducting electrodes by doing an irradiation of a $Au/YBa_2Cu_3O_7$ (YBCO)/$SrTiO_3$ stack with oxygen ions, we then transfer graphene onto these prepatterned YBCO sample, we pattern the graphene layer with an oxygen plasma. We use $SrTiO_3$ and Al_2O_3 dielectric gates to modulate graphene charge carrier's density in these YBCO/graphene devices. We then describe the fabrication of graphene Hall bars used to characterize the $SrTiO_3$ (STO) and Al_2O_3 dielectric gates. The lithography recipes are given in the appendix B.

II.1 YBCO/graphene junctions fabrication

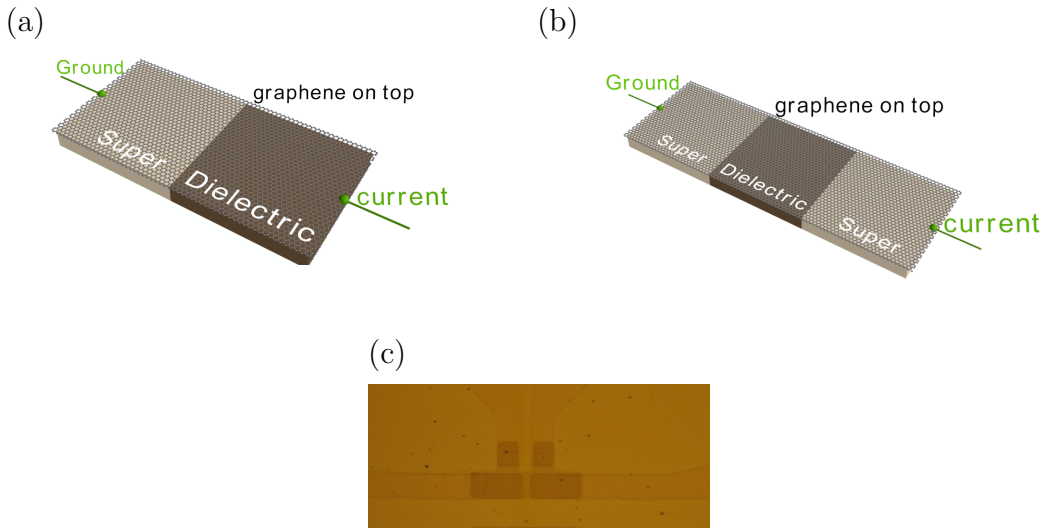

Figure II.1 – The type of devices we want to fabricate. (a) A sheet of graphene is at the interface between a superconductor and and insulator (dielectric) such that it is possible to measure the interface between the proximitized graphene part and the normal graphene part. (b) A sheet of graphene makes a bridge between two superconducting electrodes such that one can measure a superconductor/graphene/superconductor junction. In both cases, a dielectric gate should allow to change the charge carrier density in the normal graphene part. (c) Picture of a YBCO graphene device, four YBCO electrodes (dark yellow) are connected by a graphene sheet (grey).

The devices we aim to fabricate are schematically shown on the figures II.1a and II.1b. In both cases, graphene becomes superconducting by proximity effect on top of the superconductor if the interface between the superconductor and graphene is transparent. The device consists either of a superconducting electrode connected to a graphene sheet, in which case we can measure only the normal graphene/superconducting graphene interface as shown on figure II.1a. Or it consists of two superconducting electrodes connected by a graphene sheet, in which case we can measure the superconducting graphene/normal graphene/superconducting graphene junction as shown on figure II.1b. A picture of the actual device is shown on figure II.1c. The device consists of four YBCO superconducting electrodes inside an insulating

matrix, the superconducting electrodes are connected through a graphene sheet. We use either the substrate (STO) as a back gate or an alumina top gate (not fabricated on the device of figure II.1c). Depending on the distance between the superconducting electrodes, we can be either in the configuration of figure II.1a or in the configuration of figure II.1b.

Figure II.2 – Structure of Josephson junctions reported in the literature, a low-Tc superconductor is deposited on top of a graphene sheet. (a) The superconductor MoRe is contacting a graphene sheet on the side, image taken from [**?**]. (b) The superconductor $NbSe_2$ is deposited on a graphene sheet, image taken from [**?**].

While several methods to fabricate graphene superconductor junction are reported in the literature, they are not compatible with YBCO. Indeed, graphene Josephson junctions are usually fabricated by depositing superconducting electrodes on top of a graphene sheet as shown on figure II.2. This is the case in complex device geometries with encapsulated (shown on figure II.2a) or suspended graphene [**?**, **?**]. This is also the case when the superconductor is exfoliated and transferred onto the graphene [**?**] as shown on figure II.2b. These techniques are incompatible with YBCO, first because the attractive force between the YBCO layers is too strong for YBCO to be exfoliated. Second YBCO growth conditions are incompatible with graphene: graphene would be burned at the YBCO growth conditions (680 °C in pure O_2 atmosphere), so that YBCO cannot be grown on graphene. We therefore do a wet transfer of graphene onto a piece of previously patterned YBCO. The main fabrication steps are depicted on figure II.3.

II.1.1 Stack growth

We start the graphene/YBCO device fabrication with the growth by Pulsed Laser Deposition (PLD) of a stack of Au (4 nm)/YBCO (50 nm) on an STO (500 μm) substrate[1]. PLD is done in a vacuum chamber which pressure and gas content are controlled manually, the PLD principle is schematized on figure II.4. A laser[2] hits the target which atoms are ejected in a plasma which then hits the substrate. Some atoms stick to the substrate and reorganize themselves into an orthorhombic crystal in the case of YBCO. For superconducting YBCO, the growth conditions are around 680 °C and 0.36 mbar oxygen pressure. The PLD machine contains both a YBCO and a Au target on a support which allow to deposit a Au layer on YBCO without breaking the vacuum. We deposit first 50 nm of (001) YBCO on a commercial STO substrate followed by the deposition of 4 nm of amorphous Au. The YBCO growth

[1]The stacks used for the study of graphene YBCO interface conduction in chapter 3 were grown in our laboratory by Rozenn Bernard and Anke Sander.

[2]The laser has a typical power of 700 mW, a repetition rate of 5 Hz, and a pulse duration of 25 ns.

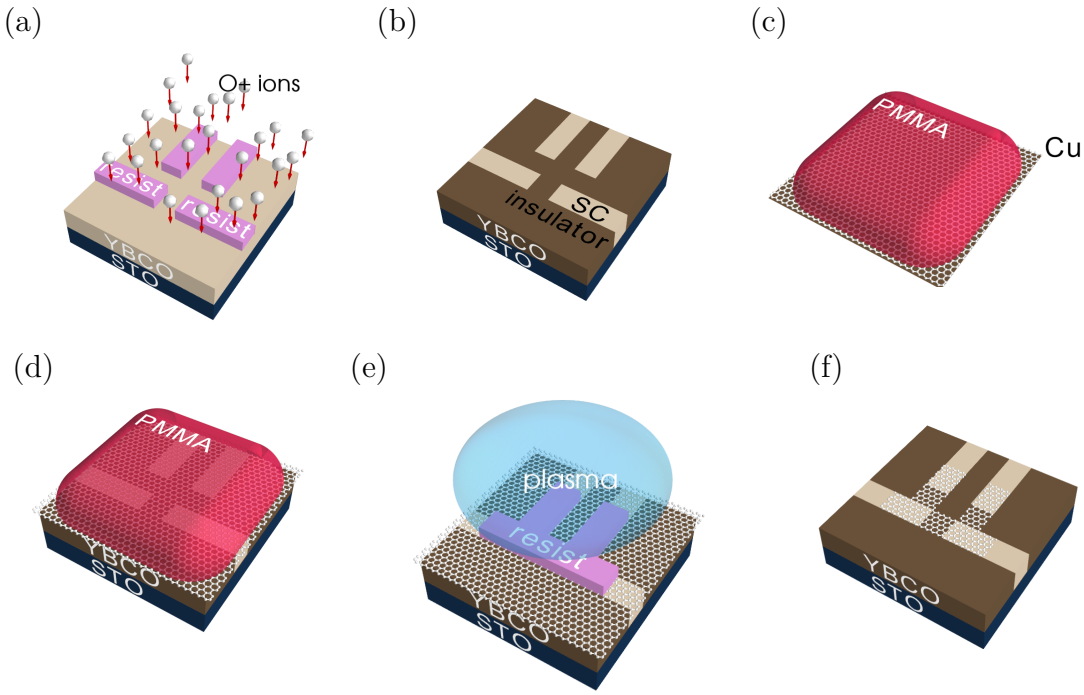

Figure II.3 – Schematic of the fabrication process steps to obtain a YBCO/graphene junction. (a) Oxygen ions render the YBCO part non covered by resist insulating, (b) we obtain four superconducting YBCO electrodes separated by an insulating region. (c) A single sheet of graphene is grown on copper, (d) it is then transferred onto the prepatterned YBCO. (e) A plasma step etch the graphene part non covered by resist. (f) Scheme of the final device, a single graphene sheet makes an electrical connection between superconducting YBCO leads.

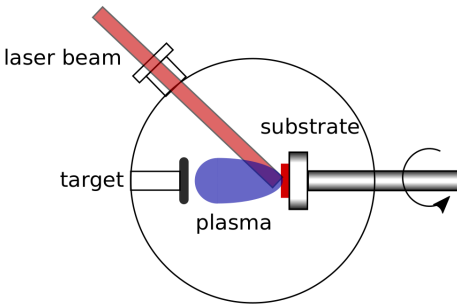

Figure II.4 – Scheme of a pulsed laser deposition set-up. An intense pulsed laser is focused onto a substrate which is a non crystalline mixture containing the different atoms we want to deposit. The laser ejects those atoms in a plasma onto the substrate target. The substrate temperature and the pressure inside the chamber are adjusted to obtain an epitaxial growth. The target is displaced during the deposition to ensure an homogeneous use of the target. The substrate is rotated during the deposition to ensure an homogeneous crystalline growth.

is monitored in situ by Reflection High-Energy Electron Diffraction. The crystallographic purity is then controlled ex situ by x-ray diffraction and the YBCO roughness is checked by

atomic force microscopy, the root mean square roughness of such sample is about 3 nm. The Au layer protects the YBCO from deoxygenation and improves the contact between YBCO and graphene. The resistance of YBCO/graphene devices without the gold layer was higher than 10 MΩ.

The Au/YBCO/STO stacks used in the chapter 4 are commercial samples from Ceraco. The commercial samples are a stack of 50 nm Au/50 nm YBCO/500 micrometer STO. We reduce the gold thickness down to 4 nm by ion beam etching.

II.1.2 YBCO lithography

We then fabricate junction of superconducting YBCO electrodes separated by insulating YBCO. We therefore define by lithography YBCO regions which will remain superconducting, the non resist covered part will become insulating after the oxygen ions irradiation step. The lithographic pattern consists of four parts shown in pink on figure II.5a which will be the superconducting electrodes. We use the same scheme to fabricate devices with a large gap between superconducting electrodes by optical lithography shown schematically on figure II.6a and devices with a small gap which picture is shown on figure II.6b.

The aim of the devices with a large gap is to measure the graphene/YBCO interface using a three terminal measurement. The smaller devices aim is the observation of a supercurrent across these junctions. The small junctions were fabricated by Christian Ulysse in the Centre de Nanosciences et de Nanotechnologies (C_2N) in Marcoussis. The distance between superconducting electrodes varies from 50 nm to 700 nm. The electron beam lithography markers allow afterward to align both the graphene lithography step made by optical lithography as well as the top gate lithography step made by electron beam lithography.

II.1.3 YBCO irradiation by oxygen ions

We then irradiate the sample with oxygen ions to render insulating the YBCO parts non-covered by resist as shown on figure II.5a. The oxygen ions create a large amount of disorder in the YBCO crystal [**?**] which makes it fully insulating. The ions are stopped by the resist: the oxygen ion penetration depth in the resist layer (about 600 nm as calculated in [**?**]) is smaller than the resist thickness. The YBCO irradiation by oxygen ions process was first described in [**?**]. We irradiate the sample at the INESS facility in Strasbourg. Oxygen molecules are ionized in a vacuum chamber at 10^{-6} mbar. The oxygen ions are directed to the sample with an energy of 110 keV. The ions energy is high enough to cross the 4 nm Au layer covering the YBCO. A dose of 2×10^{15} ions.cm^{-2} is sufficient to make the bare YBCO parts fully insulating, its resistance measured in a two point geometry is higher than 10 MΩ. At the end of the fabrication procedure, including the transfer of graphene described in the next section, the critical temperature of the superconducting YBCO parts is reduced from 90 K to typically 70-80 K.

After the irradiation, an Ion Beam Etching (IBE) step with Ar removes the gold which is on top of the insulating YBCO. The Au part on top of the superconducting YBCO is still covered with resist which protects the Au layer from the etching. The ion beam etching

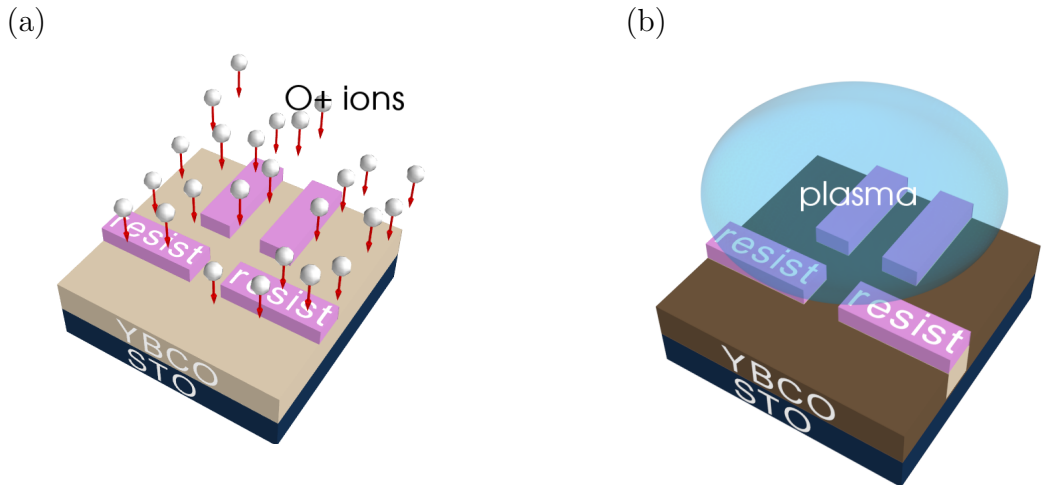

Figure II.5 – (a) Irradiation by oxygen ions causes enough disorder in the YBCO layer to render it completely insulating. The resist is thick enough to prevent the oxygen ions from penetrating the YBCO layer such that the YBCO covered parts stay insulating. (b) The resist upper part hardens during the irradiation process, an oxygen plasma removes this hardened resist part.

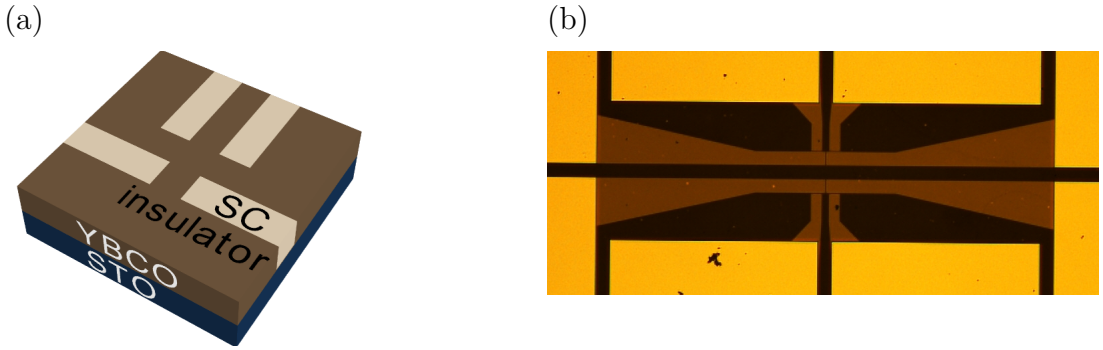

Figure II.6 – Schemes of the superconducting YBCO electrodes separated by insulating parts. (a) Schematic of the planar device after the resist has been removed, superconducting YBCO electrodes (beige) are separated by insulating YBCO parts (brown). (b) Optical image of a YBCO device prepared by e-beam lithography, the distance between electrodes is 350 nm. They are 70 devices on a chip prepared by e-beam lithography, the YBCO electrodes spacing ranges from 50 nm to 700 nm.

parameters are 280 V, 60 mA, the etching takes about 30 seconds. The IBE machine model is the Mu 600 S from Plassys. The etching time is long such that it starts to thin the insulating YBCO part but this assures that no gold is remaining on top of the insulating YBCO (such a remaining gold layer would short-cut electrically the graphene). The resist upper part hardened during the oxygen irradiation and ionic beam etching, this hardened resist does not dissolve in acetone. As shown on figure II.5b, a plasma step - of parameters 1000 W, 200 mT, 100 mT O_2, 14 mT Ar, for a duration of 10 minutes - removes the resist's

upper part. We then remove the remaining resist in acetone. A picture of the device before the graphene transfer is shown on figure II.6b. A last plasma step is done right before the graphene transfer to increase the electrical contact between YBCO and graphene.

II.1.4 Graphene transfer and patterning

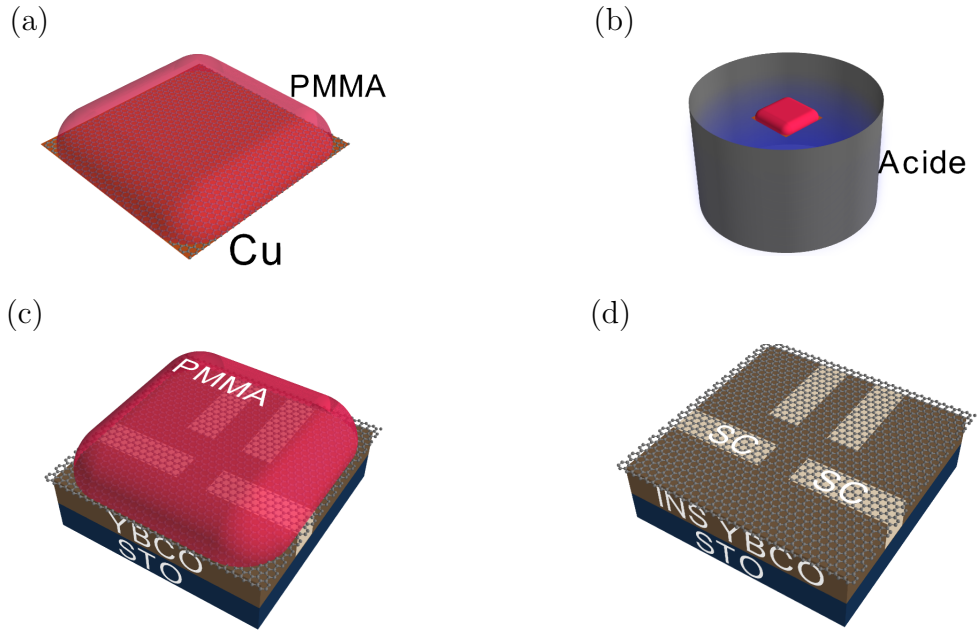

Figure II.7 – Schematic of the graphene transfer onto the YBCO chip. (a) A single layer of graphene is grown on a Cu foil in Cambridge by chemcial vapor deposition [**?**]. We deposit a drop of PMMA to protect the graphene on top of the Cu. (b) The Cu is selectively etched in a periodic acid Schiff bath. The acid bath do not etch the graphene and the PMMA. The graphene is then transferred into a deionized water bath (not shown). (c) The graphene is finally transferred into the prepatterned YBCO, a baking at 70 °C for 5 minutes remove the water which would else be trapped between the graphene and the YBCO. (d) Sketch of the device at the end of the transfer process after the PMMA has been removed in an acetone bath.

Graphene is grown on top of a copper foil by chemical vapor deposition in Cambridge. The growth process has been described elsewhere [**?**]. Figure II.7 shows a scheme of the graphene transfer from the Cu onto the YBCO. We protect the copper side supporting graphene with a drop of polymethyl methacrylate (PMMA) resist. The other side of the copper foil might contain carbon residues which are removed with a wet tissue. The Cu foil is put at the surface of a periodic acid-Schiff bath for one night which is enough for the bath to fully dissolve the copper. The graphene covered by PMMA is then transferred to a deionized water bath to neutralize the acid. The graphene is then transferred on top of the previously patterned YBCO. The sample is heated at 70 °C for 5 minutes to remove the water trapped between the graphene and the YBCO. The layer of PMMA resist is then dis-

solved in an acetone bath. Raman spectroscopy is usually done to verify the good graphene deposition. A typical Raman spectrum is shown on figure II.9.

The last step to obtain the YBCO/graphene junction is an optical lithography to define the graphene channels between the superconducting electrodes. The lithography parameters are given in appendix B. The parts of graphene non covered by resist are etched in a plasma for 30 seconds at 150 V, 30 W, 100 sccm O_2 in 100 mT [**?**]. The plasma machine is the model RIE NE 110 from Nextral. The graphene etching from the desired areas can be check by Raman spectroscopy. The remaining resist is removed in an acetone bath.

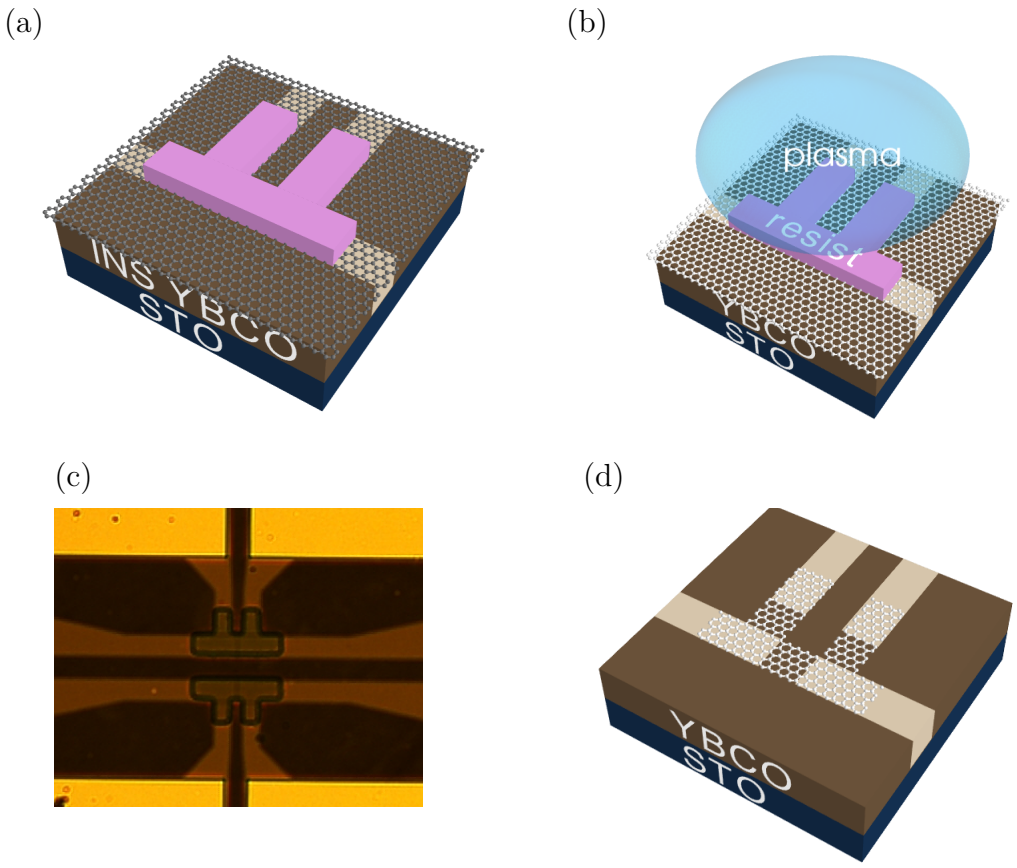

Figure II.8 – Scheme of the different steps used to obtain a graphene junction between the superconducting YBCO electrodes. (a) An optical lithography step allows to define the junction pattern with a graphene protective resist layer. (b) A plasma etch the graphene part non-covered by the resist. (c) Optical image of the graphene covered by resist after the graphene lithography and the plasma on a device. The graphene on YBCO (without the resist) has a very small optical contrast. (d) Schematic of the final device with graphene connecting YBCO superconducting electrodes. The device geometry of the sample prepared by optical lithography and e-beam lithography allows for example to do two and four points measurements in order to measure the graphene channel.

A schematic of the final YBCO/graphene junction device is shown on figure III.1a. Four superconducting YBCO electrodes (bright color) are connected through three graphene channels (white).

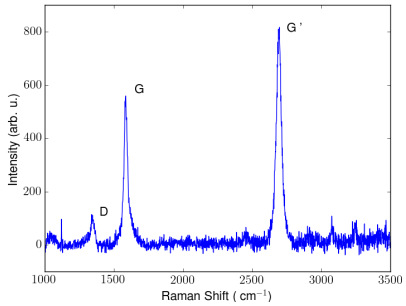

Figure II.9 – Typical Raman spectra obtained on our devices. The G and G' peaks are characteristics of graphitic structures. Their ratio is a signature of the number of graphene layers, here it is a single graphene layer.

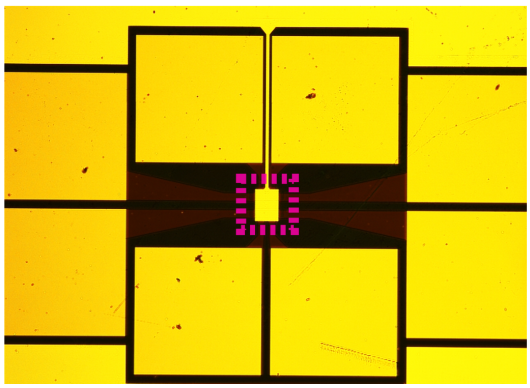

Figure II.10 – Microscope view of a graphene YBCO junction with a top gate. The graphene junction (shown on figure II.8c) is hidden under the central gold electrode (outlined with a pink dashed line).

II.1.5 Top gate fabrication

The YBCO/graphene samples are lying on an 500 μm thick STO substrate. We used the STO as a back gate for the devices prepared by optical lithography, these measurements are presented in the chapter 3. We also develop a process to fabricate a top gate for the small junction, these measurements are presented in chapter 4. We use a 45 nm layer of Al_2O_3 as a dielectric, the dielectric constant of Al_2O_3 is about 9 [**?**].

The Al_2O_3 growth is made in two stages: first a 1 nm layer of Al is deposited by evaporation and oxidized in the room atmosphere, second 45 nm of Al_2O_3 are deposited by Atomic Layer Deposition (ALD). The ALD process principle is decribes on figure II.11. The deposition is made with Bruno Dlubak in our laboratory.

Al_2O_3 is etched by the traditional optical lithography developers we use (MF 319 or MF CD 26). We therefore use electron beam lithography to define the gate electrodes even if the pattern is large enough that it could be performed by optical lithography. The lithography is performed by Christian Ulysse in the C2N laboratory. The electrode design avoids as much as possible overlaps between the top gate electrode and the bottom YBCO electrode to prevent possible short-cut. The overlap area is about 3 600 μm^2. The gate itself covers all the graphene parts on top of insulating YBCO and on top of superconducting YBCO, the electrodes will be used either as a junction or as a probe. A picture of a YBCO/graphene device with a top gate is shown on figure II.10.

II.2 Graphene characterization

We fabricate devices complementary to the YBCO/graphene junctions to characterize our $SrTiO_3$ and Al_2O_3 gates capacities as well as the graphene doping at zero gate voltage via Hall effect measurements. The device is schematically shown on figure II.12a, it consists of a graphene sheet on top of an insulating YBCO substrate. As explained in the previous section II.1.3, we use oxygen ions irradiation to render the whole YBCO sample insulating.

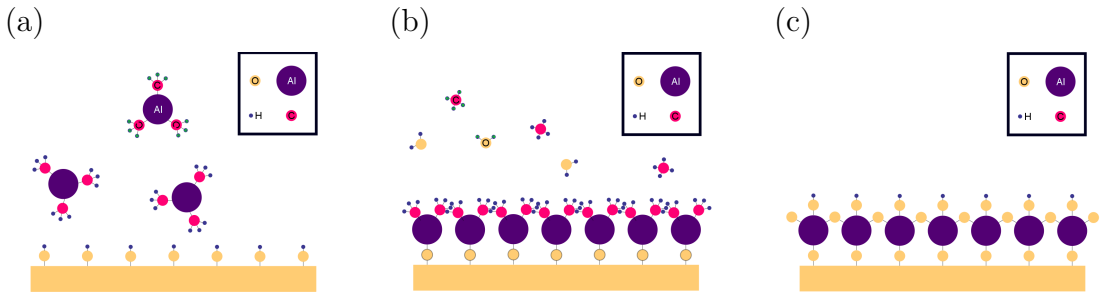

Figure II.11 – Atomic layer deposition of an alumina barrier which will be used as a dielectric for the top gate. In practice, a 1 nm alumina layer is deposited as a seed layer before the ALD deposition. (a) In the first cycle, trimethylaluminum (TMA) is injected in the ALD chamber, TMA will attach to the $Al-H$ terminations of the seed layer. (b) Once all the $Al-OH$ terminations have been replaced by $Al-O-Al-C_2H_6$ groups, H_2O is injected into the chamber. This oxidize the $Al-C_2H_6$ terminations into Al_2O_3. (c) At the end of this cycle, all the terminations are of the $Al-OH$ type, there are no more $Al-O-Al-C_2H_6$ terminations. The surface is chemically identical to the first step and the next TMA pulse will again fix into this Al_2O_3 layer.

Graphene on top of this insulating YBCO substrate is patterned into a Hall bar shape. The sample fabrication was made as close as possible to the fabrication of the YBCO/graphene junction such that the doping and the capacitance of both type of samples are similar. We also fabricated a top gate on one of the Hall bar. The top gate fabrication method is the same as for the top gate on the YBCO/graphene junctions described in the section II.1.5. All the other lithographic steps are made by optical lithography.

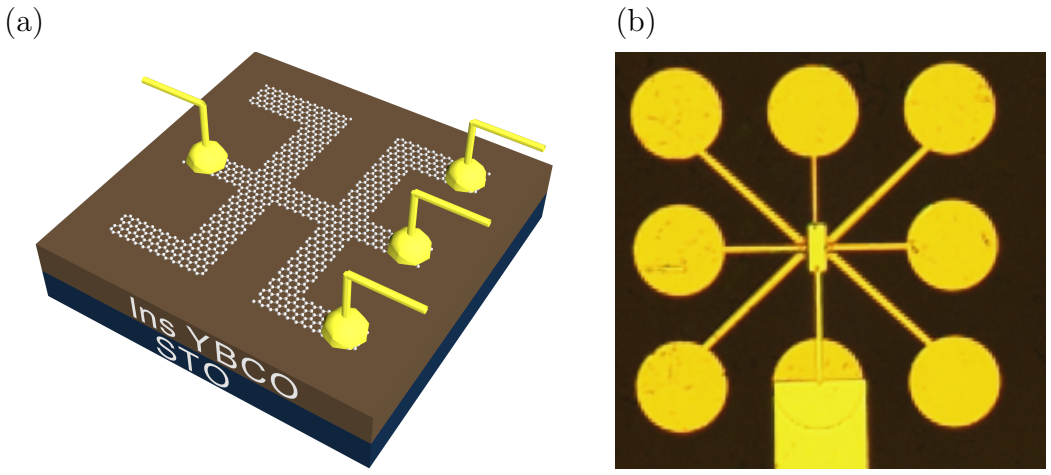

Figure II.12 – (a) Schematic view of the Hall bar device without the top gate. The graphene shape allows to measure the longitudinal and transverse resistance as a function of magnetic field from which we deduce the graphene carriers density for different gate voltages. (b) Microscopic picture of a Hall bar device with a top gate.

We first deposit alignment markers on the insulating YBCO substrate. We deposit 20 nm of Ti and 100 nm of Au before lifting off the metal on top of the resist with acetone. Graphene is then transferred onto the sample as already described in the section II.1.4 for YBCO/graphene junctions.

We pattern optical lithography resist into a Hall bar shape. The graphene part non covered by resist are etched in an oxygen plasma for 30 seconds at 150 V, 30 W, 100 sccm O_2 in 100 mT [**?**]. The resulting graphene Hall bar shape is depicted on figure II.12a. Six electrodes connect a central graphene part with a rectangular shape. The electrodes design allows to measure in four probe measurement both the graphene longitudinal resistance as well as the graphene transverse resistance.

The last lithographic step is the deposition of metallic electrodes to connect the graphene to the sample holder. We deposit after an ionic scouring 20 nm of Ti and 100 nm of Au by evaporation. The ionic scouring improves the electrical contact between the graphene and the metal. The Ti layer ensures a better adhesion of the metal on the substrate. Without this layer all the Au would be removed when put in the acetone bath. The final device is visible on figure II.12. We describe in the chapters 3 and 4 the measurement on this device of the gate capacities and of the graphene doping.

To conclude, we have fabricated superconducting YBCO/graphene planar junctions using oxygen ion irradiation to define YBCO superconducting electrodes followed by the transfer of CVD graphene onto the YBCO substrate. We used Al evaporation and atomic layer deposition to grow alumina on these junctions which we can use for electric gating. We fabricated a graphene Hall bar to characterize the graphene and the gate properties.

III – Study of the graphene/$YBa_2Cu_3O_7$ interface: superconducting pairs tunneling

The electrical current is carried by normal electrons and holes in graphene but it is carried by Cooper pairs in proximitized superconducting graphene. The proximity effect and the conversion from a supercurrent to a normal current occurs through the Andreev reflection process. To study experimentally the Andreev reflection one has to measure the superconductor/normal material (S/N) interface conductance. The aim of this chapter is to study the conductance of the normal graphene/superconducting graphene interface.

For this purpose, we fabricated graphene junctions between superconducting YBCO electrodes to measure the normal graphene/superconducting graphene interface conductance. The planar device consists of superconducting electrodes embedded inside an insulating YBCO matrix. The distance between superconducting electrodes range from 1 to 5 microns. The electrodes are connected by a graphene sheet as shown on figure III.1, the device fabrication is detailled in the chapter 2. We perform interface conductance measurements which we analyze as a function of the YBCO graphene contact transparency on figure III.2. A description of the transport measurement set-up is given in the appendix A. We discuss the gate voltage modulation of the conductance of a device with transparent contacts. A theoretical model taking into accounts the effect of a potential barrier at the superconductor/graphene interface allows to compute numerically the superconductor graphene structure conductance. We compare the transparent device behavior to this model on figure III.12. We then discuss the values of the different parameters entering the numerical simulation. We also discuss the physical origin of the potential barrier at the interface. We can separate the contribution of the Cooper pairs and of the normal electrons to the conductance from the numerical simulation, this highlight the modulation of the Andreev reflection with the barrier height. The results of this chapter are published in [**?**].

III.1 Experimental conduction measurement

We perform three terminal measurements to isolate the conduction of a single YBCO/graphene interface. The measurement geometry is depicted on figure III.1. We first analyze the contribution from the different layers to the measured conductance. We then discuss the different contributions weights and the conduction versus bias voltage behaviors as an indication of the YBCO/graphene interface transparency. We use an STO back gate to modulate graphene carrier density on our graphene YBCO junction. We characterize our graphene residual doping and our gate electrical capacity on a graphene Hall bar. We then describe the conductance dependance on gate voltage.

III.1.1 Contributions to the measured conductance

Our device is shown schematically on figure III.1a, it consists of four superconducting YBCO electrodes inside an insulating YBCO matrix. The superconducting electrodes are covered by a 4 nm Au layer, a sheet of graphene makes the bridge between the superconducting electrodes. In our measurement geometry, the current crosses the following layers: YBCO, Au, graphene, Au, YBCO. Depending on the quality of the contact between layers and on the layer's resistance, different conduction behaviors are expected as a function of bias voltage and gate voltage. We measure the graphene/Au/YBCO interface in a three probe geometry

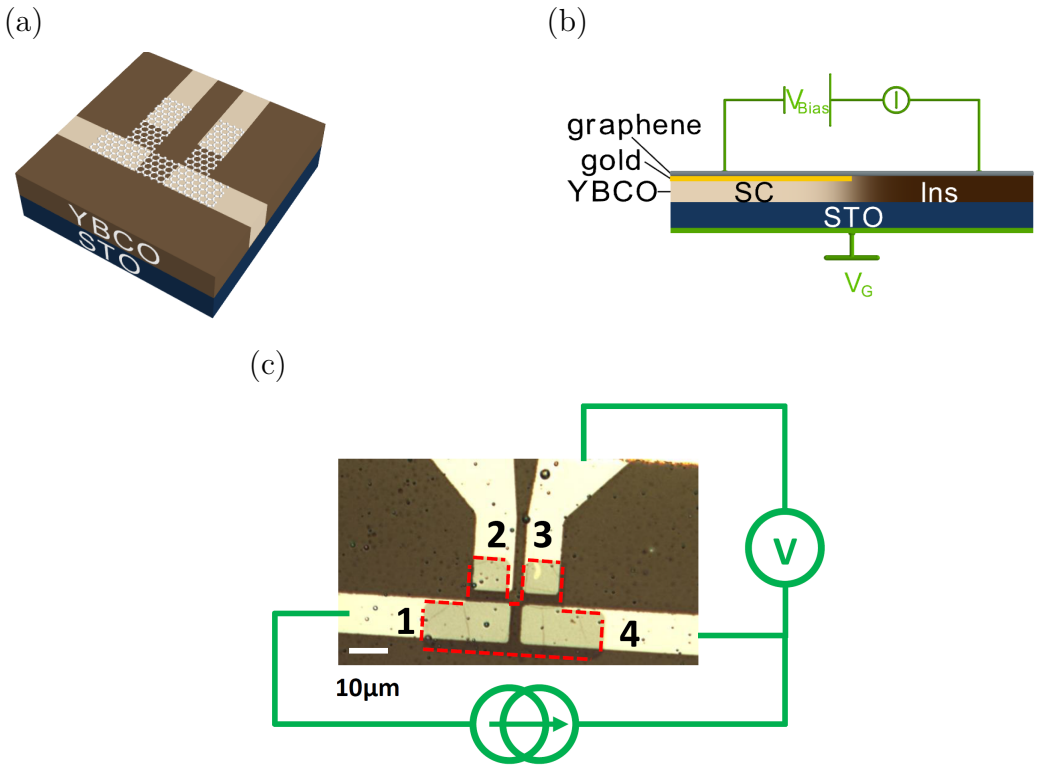

Figure III.1 – (a) Schematic of the experimental device used to study YBCO graphene interface conductance. Four YBCO electrodes (in beige on the figure) with a gold coating are separated by 5 μm width insulating YBCO parts (in brown). They are connected through a piece of graphene (in white). (b) Side view schematic of the sample. The STO is used as a gate at low temperature. The dramatic reduction of STO dielectric constant with increasing temperature makes the gate ineffective at higher temperature. A thin layer of gold improves the contact between graphene and YBCO. (c) Microscopic image of a YBCO graphene sample. The experimental wiring in green is used to measure the YBCO graphene interface conductance. The current is injected between electrodes 1 and 4, the corresponding voltage is measured between electrode 3 and 4. The differential conductance is measured with the delta mode of the Keithley current source as explained in appendix A.

shown on figure III.1c.

The YBCO and Au resistances are both smaller than 5 Ω. They are negligible compared to the graphene sheet resistance which is about 1 kΩ [**?**, **?**]. The graphene resistance was measured on the Hall bar device described in the section III.1.3. Growing the Au in the same PLD chamber as the YBCO allows to have good contacts of the order of $10^{-7} - 10^{-6}$ Ω.cm^2. The Au/YBCO resistance was measured in vertical devices without graphene, these devices structure and the measurement scheme are described elsewhere [**?**]. A conservative estimate of the contact area between gold and YBCO of 10×10 μm^2 gives a Au/YBCO resistance smaller than 1 Ω. The Au layer plays a crucial role to improve the contact between graphene and YBCO. The same type of YBCO/graphene devices without the Au layer had resistances higher than 10 MΩ. Considering earlier experiments and theory, the 4-nm Au interlayer is thin enough to be fully superconducting with a d-wave order parameter:

1. Experimentally, STM measurements on polycrystalline Au deposited on c-axis YBCO showed that the penetration length of superconductivity into Au is 30 nm (see e.g. [**?**]). Since in our experiment the Au layer thickness is one order-of-magnitude smaller (4 nm), we do not expect a strong suppression of the induced order parameter.

2. Theoretical studies on the proximity effect between d-wave superconductors and diffusive normal-metals show that, when the c-axis is perpendicular to the superconductor/metals interface (as in our experiment), the condensate penetrating the normal-metal decays and preserves the d-wave symmetry over the length scale of the normal-metal electronic mean free path (see e.g. [**?**]). The mean free path in polycrystalline Au is typically of the order of tens of nm (see e.g. [**?**]), that is, one order-of-magnitude longer that the thickness of the Au layer in our experiments. From this, we expect that the d-wave symmetry is preserved at the gold-graphene interface.

Similarly, if the contact between gold and graphene is good, the graphene on top of the superconducting YBCO is thin enough to be considered a part of the superconductor as well. This was experimentally demonstrated by scanning tunneling experiments [**?**]. Thus, when the graphene/gold contact is transparent, the dominant contribution to the conductance comes from the interface between normal graphene lying on the insulating parts of YBCO and graphene which becomes superconducting by the proximity effect on top of the superconducting YBCO. The contacts quality between the superconducting stack and the graphene determines the conduction behavior from tunneling - with a dip at zero bias - to transparent behavior - with a zero bias conductance peak. A tunneling behavior always reflect a high graphene YBCO resistance [**?**, **?**]. As explained in the introduction chapter, a zero bias conduction enhancement in a graphene superconductor structure might be due either to specular Andreev reflection [**?**] or to Andreev bound states [**?**]. We did not find a correlation between the measured conductance behaviors (ZBCP or tunnel) and the corresponding resistance values. This is certainly because of a non homogeneous electrical contact over the whole graphene gold interface area.

In the transparent case - when there is a good contact between YBCO and Au, and a good contact between Au and graphene - we measure the superconducting graphene/normal graphene interface in the geometry of figure III.1c.

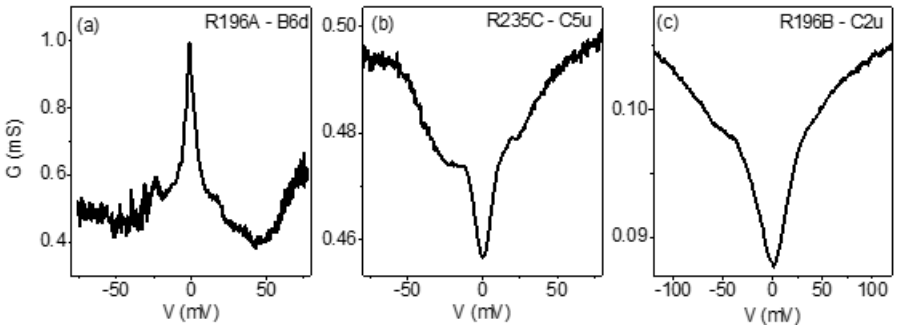

Figure III.2 – Differential conductance of different devices measured with the geometry of figure III.1c. (a) R196A-B6D presents a transparent behavior with a doubling of the conductance at zero voltage compared to high voltage. (b) R235C-C5U presents a tunnel behavior although it has a comparable resistance (of about 1 kΩ) as R196A-B6D at high bias. (c) R196B-C2U presents a tunnel behavior, its larger resistance at high bias of about 10 kΩ reflects a less good contact between the gold and the graphene than the device R196A-B6D.

III.1.2 Effect of the interface transparency

We present on figure III.2 different devices differential conductance as a function of the bias voltage, they show either a tunnel or a transparent behavior. These devices were fabricated and measured by Fabian Cuellar. Some examples of the obtained results are discussed below.

The R235C-C5U and R196B-C2U devices present a dip of the conductance at zero bias attributed to particle tunneling through the superconductor/graphene interface. This type of behavior is interpreted as reflecting a low transparency between the graphene and the gold. These devices conductance showed a poor gate voltage dependence as expected when the gold/graphene interface resistance is the principal contribution to the measurement. We show on figure III.3 how the conductance dip of the device R235C-C5U is flattened by ther-

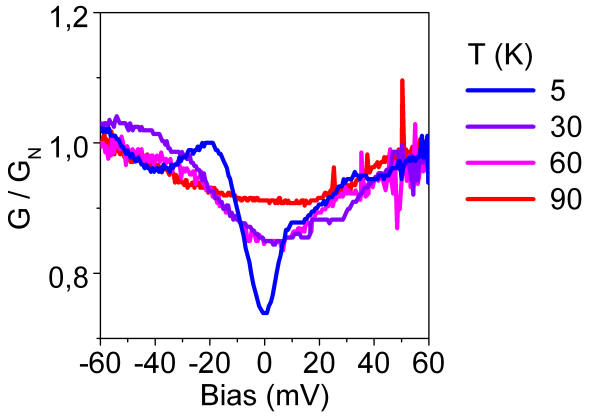

Figure III.3 – Differential conductance of the device R235C-C5U for different temperatures. The conductance dips flattens when the temperature increases, it is almost flat above the YBCO critical temperature.

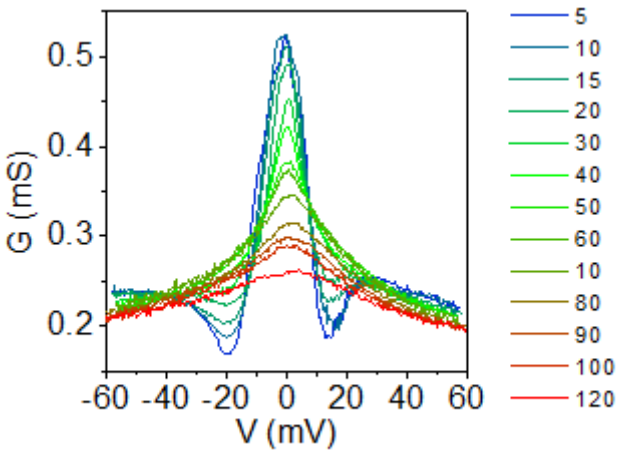

Figure III.4 – Differential conductance of the device R196A-B1U as a function of temperature. The conductance is typical of a transparent device with a conductance enhancement at low bias. As the temperature is increased the peak is flattened until the conductance becomes flat above the YBCO critical temperature.

mal effect. The dip disappear above the YBCO critical temperature.

The R196A-B6D and R196A-B1U (on figure III.2 and III.4) device conductance's show a zero bias conductance peak (ZBCP) reflecting a transparent interface and Andreev bound states at the superconductor interface. We show on figure III.4 how the conductance peak of this device R196A-B1U is flattened by thermal effect. The peak is broadened with increasing temperature and becomes flat above the YBCO critical temperature. This is characteristic of a proximity effect between a d-wave superconductor and a normal material. Furthermore, this conductance enhancement does not depend on magnetic field contrary to what would be expected if it was due to a supercurrent. We therefore interpret this peak as an Andreev reflection signature.

As shown on figure III.2, the resistance of the device R196B-C2U is higher (10 kΩ) compared to the resistance of the device R196B-B6D (1 kΩ). This is expected for two similar devices where one is transparent and the other one tunnel. The resistances of the devices R196B-B6D (ZBCP), R196A-B1U (ZBCP) and R235C-C5U (tunnel) are all of the same order of magnitude (1 kΩ). These three devices have different conduction behaviors but similar resistances. This suggests a non-homogeneous contact between the gold and the graphene. In other words, the conductivity of the device R196B-B6D is higher than the conductivity of the device R235C-C5U but the contact area of R196B-B6D is smaller such that they have a comparable resistance. This reduction of the contact area might be due to electrical contact inhomogeneities. This inhomogeneities come from different factors, as for instance resist residues preventing an homogeneous contact between gold and graphene.

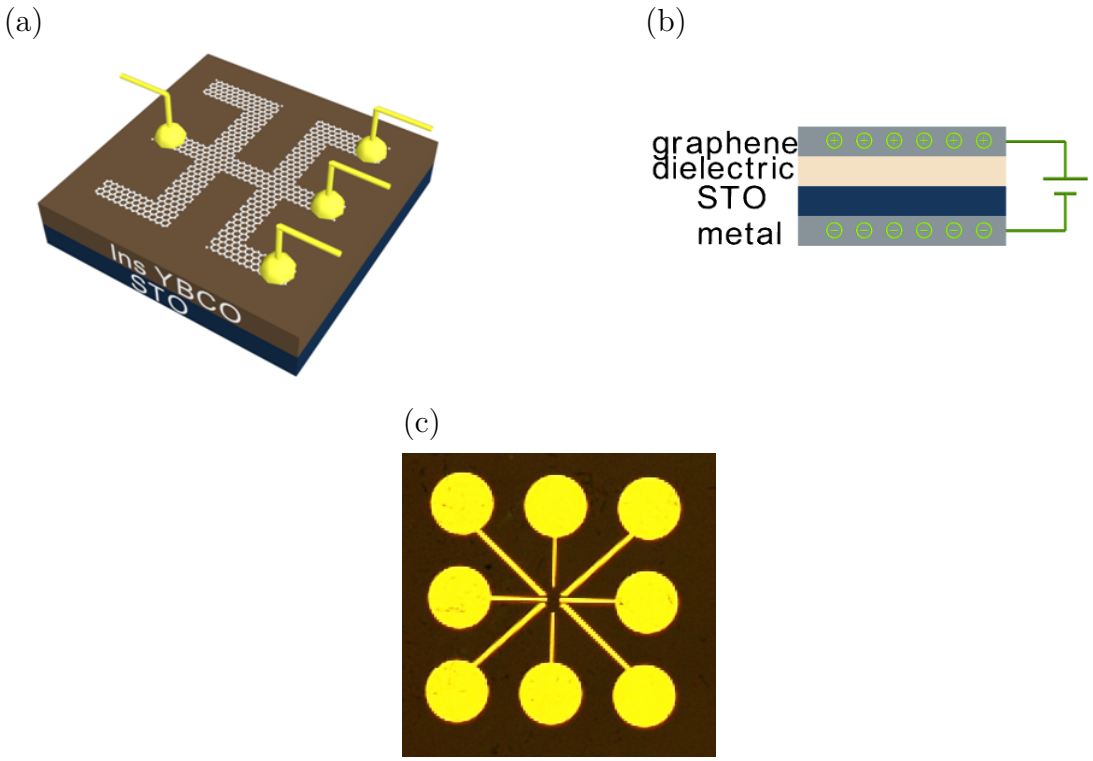

Figure III.5 – (a) Scheme of the Hall bar device used to measure the STO/irradiated YBCO stack capacitance. (b) Side view of the gate consisting of STO (bottom) and insulating YBCO (top), charges accumulate in the graphene on the application of a gate voltage. (c) Microscopic view of the Hall bar.

III.1.3 Back gate characterization

We fabricate and measure the residual graphene doping and the capacitance of the back gate of a Hall bar device. Since the fabrication techniques are similar for the Hall bar and for the YBCO/graphene junctions, the residual doping and capacitance of both devices should be the same. The fabrication of the Hall bar is described in chapter 2.

The measurement is done by applying a constant current of 50 μA between the central electrodes. The sample temperature is close to 3.3 K so that the $SrTiO_3$ dielectric constant is about 10 000 [**?**]. We measure the transverse resistance R_{xy} as a function of the out of plane magnetic field B_z as shown on figure III.6a. We extract the graphene charge density from this curve. The carrier density is indeed related to the magnetic field and to the transverse resistance through:

$$n = \frac{1}{e}\frac{\partial B_z}{\partial R_{xy}}.$$

We repeat the measurement of R_{xy} vs B_z at different gate voltages to obtain the doping

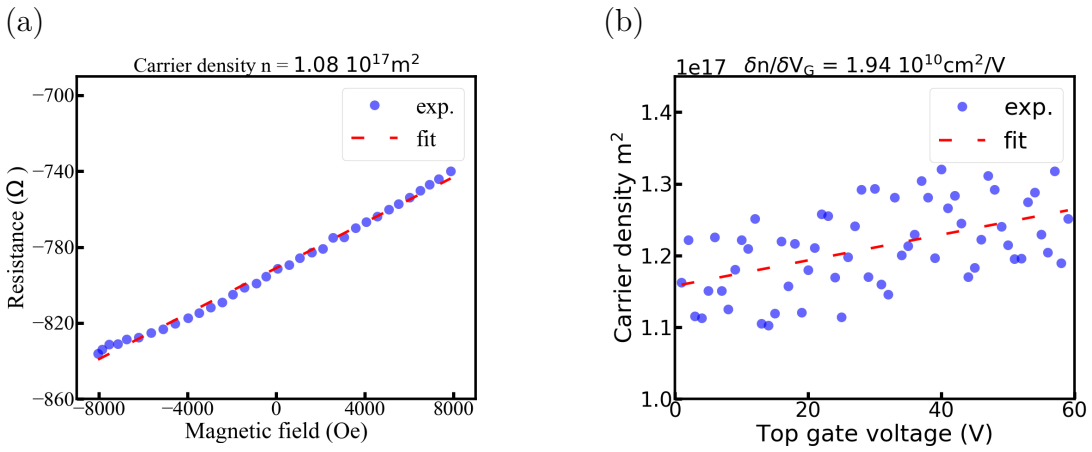

Figure III.6 – (a) The transverse resistance of graphene as a function of magnetic field when no gate is applied, the dashed line is a linear fit which gives a carrier density of $n(0) = 1.08 \times 10^{13}$ cm^{-2}. (b) The graphene carrier density as a function of the back gate voltage, the dashed line is a linear fit which gives a a capacitance $\partial n/\partial V_G = 1.94 \times 10^{10}$ cm^{-2}.V^{-1}.

variation with gate voltage shown on figure III.6b. Our device capacitance is given by:

$$C = \frac{\partial n}{\partial V_G}.$$

We obtain a negative doping at zero gate voltage of 1×10^{13} cm^{-2} and a capacitance of $\partial n/\partial V_G = 1.94 \times 10^{10}$ cm^{-2}.V^{-1}. This value is comparable the estimated one using a plane capacitor model taking $\varepsilon_{YBCO} = 10$ and $\varepsilon_{STO} = 1 \times 10^4$. We can use this values to deduce the relation between gate voltage, charge carrier density and Fermi energy as done in a next section (on figure III.11).

Note that the migration of oxygen vacancies in $SrTiO_3$ resulting in a change of the substrate capacitance has been discussed recently [**?**]. However, this migration happen at much larger electric field (100×10^3 V.cm^{-1}) than the one we applied (1×10^3 V.cm^{-1}). Also it should have no effect on the capacitance and doping effect when sweeping the gate voltage in one direction only [**?**].

III.1.4 Gate voltage dependence of the experimental conductance

We focus in the following on the behavior of the device R196A-B1U, which shows a high transparency. We first describe how the conductance evolves with gate voltage as shown on figure III.7.

The figure III.7a shows the differential conductance of the device R196A-B1U mapped as a function of bias voltage (horizontal axis) and gate voltage (vertical axis). The conductance is strongly modulated by the gate voltage. The conductance g on this figure is normalized by the high temperature conductance ($g(V) = G(V, T = 4K)/G(V, T = 120K)$). The

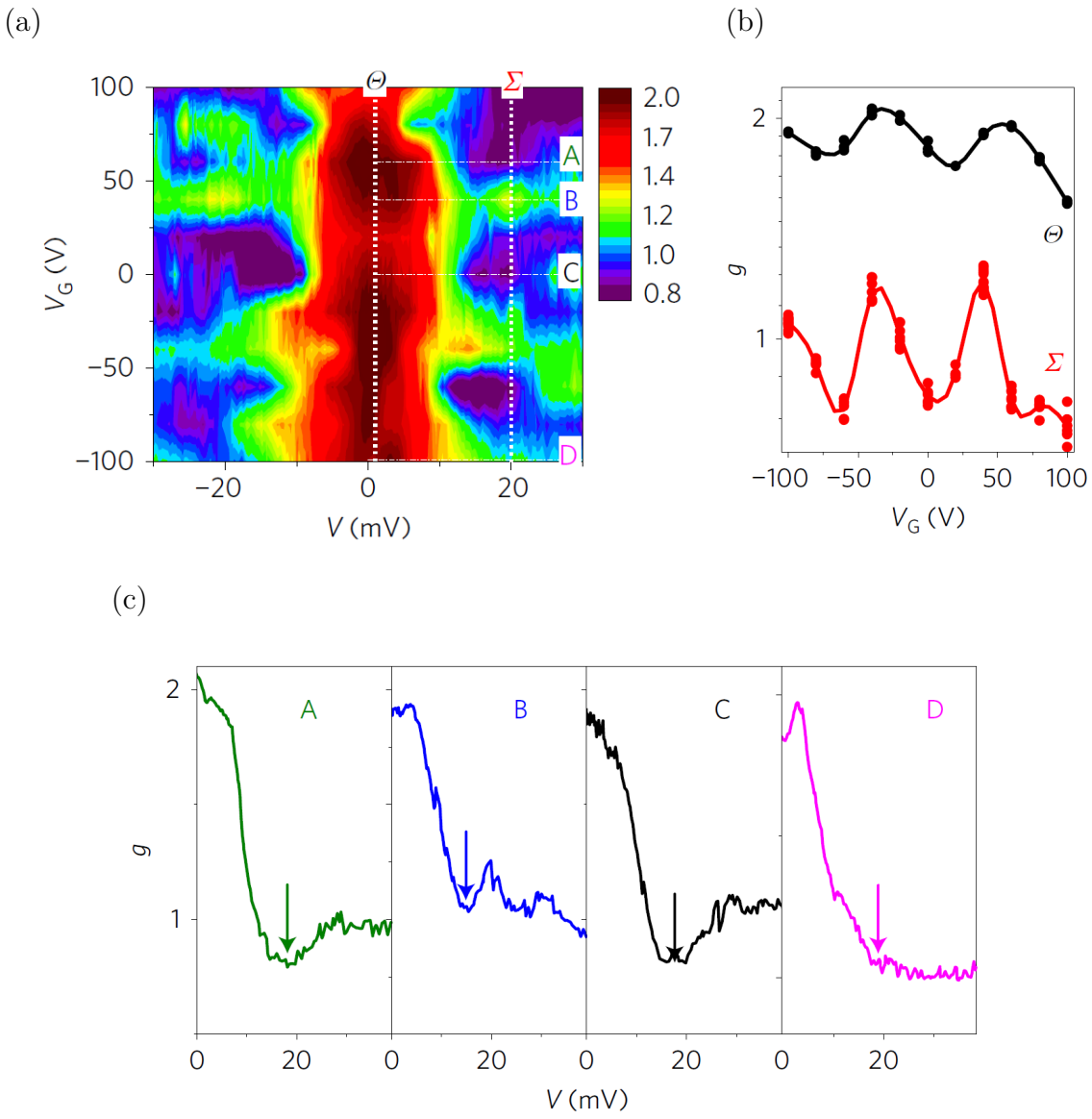

Figure III.7 – (a) Experimental conductance as a function of bias (horizontal axis) and gate voltage (vertical axis) (b) Cuts of the experimental conductance at constant bias along the line denoted θ and Σ in (a). (c) Cuts of the experimental conductance at constant gate along the line denoted A, B, C, D in (a).

conductance shape is significantly modulated by the gate, but note that our electrical gate capacity is not sufficient to cross the Dirac point. We recognize the zero bias conductance enhancement (in red) which was already present at zero gate on figure III.4. The two dips of figure III.4 around ± 20 mV appears in purple at zero gate voltage on figure III.7a. As the gate is varied, the conductance at bias voltage ± 20 mV change from this dips at gate 0 V into secondary maxima (green) at gate ± 40 V before appearing again around gate ± 80 V. At biases below 20 mV, the conductance has a weaker and less clear behavior as a function of the gate voltage. One can nevertheless see a modulation of the gate voltage at biases above 20 mV where secondary minima and maxima alternate as the gate voltage is varied. As shown on the mapping cuts at constant bias, the gate voltage dependence has a relatively well defined period of about 40 V. The differential conductance dependence with gate voltage at biases above 25 mV is shallower and more difficult to interpret.

The conductance enhancement at zero bias voltage is characteristic of bound states appearing at the interface between a normal material and a d-wave superconductor [**?**]. In a graphene/superconductor structure, a peak at zero bias could as well be due to Specular Andreev Reflection (SAR). This peak at zero bias is not due to SAR for the following reasons. Specular Andreev reflection should happen specifically at the charge neutrality point for Fermi energy smaller than the superconducting gap: $E_f < \Delta$ and the conductance enhancement should thus disappear with gate voltage. Since $E_f = \hbar v_F \sqrt{\pi n}$, this is equivalent to a graphene carrier density $n < n_{SAR}$, with

$$n_{SAR} = \frac{1}{\pi}\left(\frac{\Delta}{\hbar v_F}\right)^2 = 3 \times 10^{10}\ \mathrm{cm}^{-2}$$

where Δ is the YBCO superconducting gap and v_F the graphene Fermi velocity. We are not in this condiction, our graphene doping is about 10^{13} cm^{-2} and the peak at zero bias does not disappear when the gate voltage is varied as shown on figure III.7.

III.2 Experimental data analysis

The conductance oscillatory behavior with gate voltage shown on figure III.7 suggests electronic interferences inside a potential barrier in the graphene sheet. We therefore consider in the following the effect on the conductance of a potential barrier of height U_0 between the normal part of graphene and the superconducting part of graphene as was done in the theoretical articles of Bhattacharjee, Sengupta [**?**, **?**] and Linder and Sudbo [**?**, **?**]. We first describe the theoretical model and the principle of the calculation, we then explain how the model parameters where measured or estimated with different experiments. The energy barrier is depicted on figure III.9. The intermediate region where the barrier is located is denoted (N'), this part of graphene has a different doping $U_0 + E_f$ than both the normal part of graphene (N) with Fermi energy E_f and the superconducting part of graphene (S) with Fermi energy E'_f. The experimental origin of such a barrier encompasses different factors which are discussed in the section III.2.3. These experimental factors are the fringe field induced charge accumulation due to our capacitor geometry, as well as the width of the boundary between irradiated and unirradiated YBCO which might lead to different local

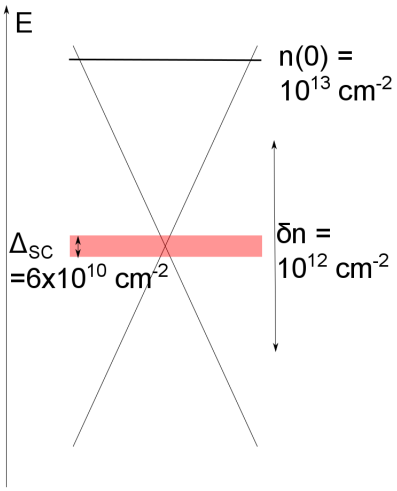

Figure III.8 – Schematic of the graphene band structure close to the Dirac point with the different energy and the corresponding graphene doping of our devices. The energy are not to scale. The Specular Andreev reflection regime (in red) corresponds to $E_f < \Delta$ and a doping $n < 3 \times 10^{10}$ cm^{-2}. The doping without applied gate voltage measured with our Hall bar is about 10^{13} cm^{-2}. The doping variation δn with 100 V applied on the back gate is about 10^{12} cm^{-2}. This shows that the back gate would allow to escape the SAR if the initial graphene doping would be in the SAR.

graphene doping on irradiated and unirradiated YBCO.

III.2.1 Theoretical model

The potential barrier between the two graphene parts is depicted on figure III.9. The conductance of the barrier will present oscillations as a function of gate voltage due to electronic interferences between particles reflected at each interface of the barrier. The particles flowing through the barrier experience a phase shift proportional to the barrier width and height, in the same way photons experience a phase shift when crossing a Fabry-Perrot interferometer. This is the main effect of an infinitely sharp barrier, whereas for an oblique barrier there would also be a fast decay of the transmission away from normal incidence. This unitary transmission is the Klein tunneling introduced in the first chapter [**?**, **?**]. Electron/hole pairs are responsible for the transport when the bias voltage is below the superconducting gap, this is discussed in section III.2.4 (on figure III.16). The electron/hole pairs experience a Klein tunneling when crossing this NN'S potential step. The phase shift χ acquired when crossing the barrier depends on the barrier height U_0, this height is experimentally shifted by the gate voltage.

$$\chi = kw = (U_0 - E_f)w/\hbar v_F,$$

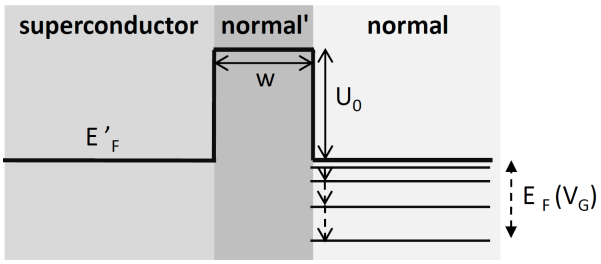

Figure III.9 – Schematic of the potential barrier between superconducting graphene (S) - left side - and normal graphene (N) - right side. Graphene on superconducting YBCO (S) becomes superconducting by the proximity effect, whereas it stays normal (N) on top of insulating YBCO. When no gate voltage is applied, the dopings in (N) and (S) are different because of the work function difference between insulating and superconducting YBCO. The graphene doping in the regions (N') and (N) vary with gate voltage. However graphene doping is fixed in (S) because the superconducting YBCO screens the gate electric field. The doping variation in (N') is associated with a Fermi vector variation which changes the phase shift electrons acquiere when crossing the barrier. The origin of the barrier is explained in the section III.2.3.

where w is the width of the (N') region, $v_F \sim 10^6$ m.s^{-1} the graphene Fermi velocity and E_f the graphene Fermi energy in the normal part.

The interface conductance calculation is made by matching the electronic wave functions on both sides of the interface from which one deduces the electron probability to cross the barrier. The theoretical calculation details are in the appendix of [**?**]. The formula linking the conductance to the probability of crossing the barrier is:

$$g(eV/\Delta, \chi, E_f/\Delta, E'_f/\Delta, \alpha) = \int_{-\pi/2}^{\pi/2} d\theta [\cos\theta(1 - |r(eV/\Delta, \chi, E_f/\Delta, E'_f/\Delta, \alpha)|^2) + \cos\theta_A |r_A(eV/\Delta, \chi, E_f/\Delta, E'_f/\Delta, \alpha)|^2]$$

where θ is the angle between the incoming electron wave-vector and the interface, E_f the Fermi energy in normal graphene (N), E'_f the Fermi energy in superconducting graphene (S), α the angle between the d-wave nodes of the superconducting order parameter and the S-N' interface, Δ the superconducting energy-gap, and χ the phase shift acquired by an electron while crossing the intermediate region (N').
The expression inside the integral of the equation III.2.1 is analytic and only the integral has to be computed numerically. We use a standard python library (scipy) to calculate the conductance numerically for different bias voltage V and gate voltage V_G. The relation between gate voltage and phase shift is

$$\chi = (U_0 - \beta V_G) w / \hbar v_F,$$

with $\beta = \partial E_f / \partial V_G$ a parameter known from Hall effect measurement. The parameters of the simulation are α the angle between the order parameter node and the interface, the doping

of the graphene E_F in the (N) and E'_f in the (S) region, the width of the intermediate region w and the superconducting gap Δ.

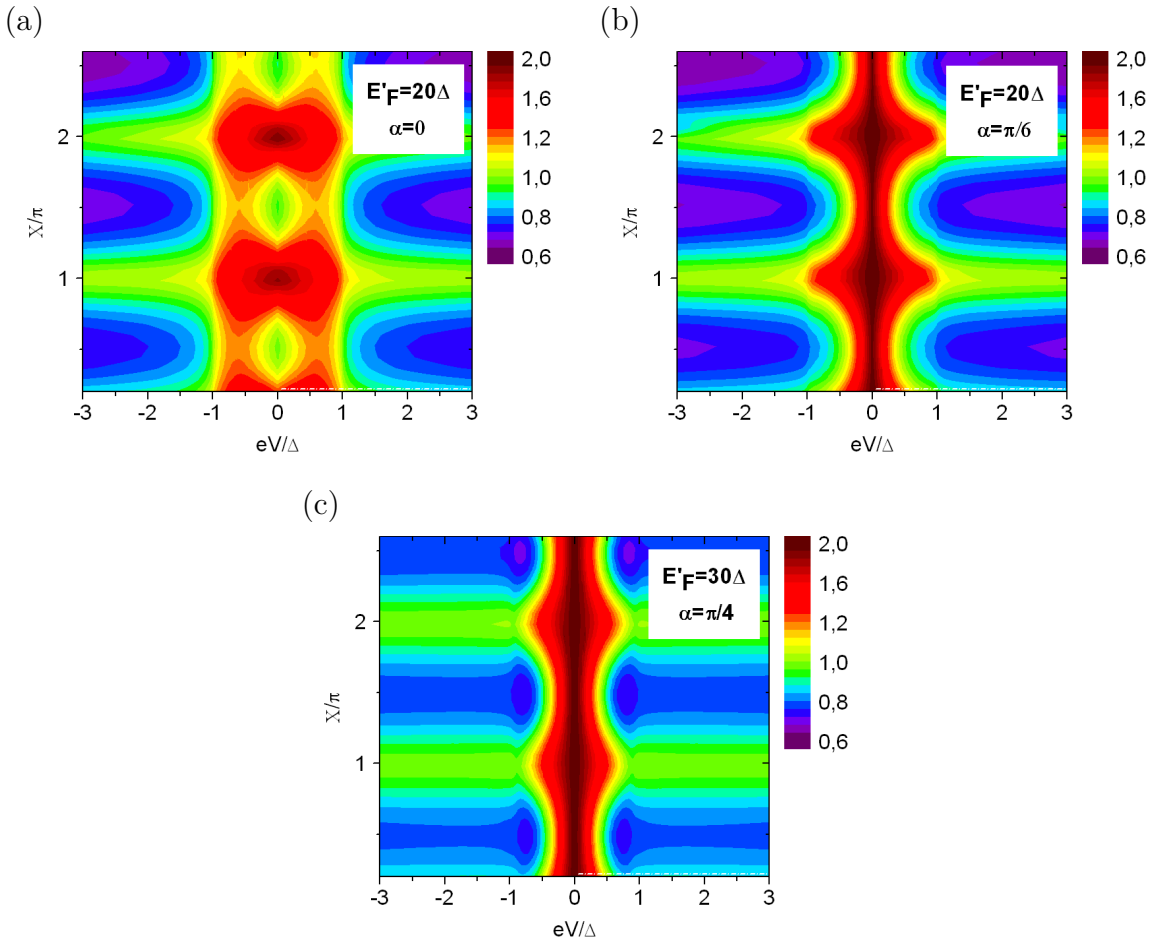

Figure III.10 – Theoretical conductance of a d-wave superconductor/graphene interface with a potential barrier in between. The conductance is mapped as a function of the bias voltage V applied on the interface and of the phase shift χ acquiered by electrons crossing the barrier. The different panels corresponds to different Fermi energies in the superconducting region $E'_f(0)$ and different angles α between the superconducting order parameter and the interface. Panel (a) corresponds to $\alpha = 0$ and $E'_f(0) = 20\Delta$. Panel (b) corresponds to $\alpha = \pi/6$ and $E'_f(0) = 20\Delta$. Panel (c) corresponds to $\alpha = \pi/4$ and $E'_f(0) = 30\Delta$. The simulations other parameters are fixed on all panels to $E_f(0) = 15\Delta$, $\beta = 5\Delta/3\pi$,w = 60nm. These are representative examples of the possible interface conductance. The differences between these curves and the experimental data of figure III.7a is underlined in the text.

We present on figure III.10 simulation mappings of the conductance as a function of the bias voltage and of the phase shift. We present simulations for different dopings E'_F and different angles α between the d-wave nodes and the interface. When the superconducting node is aligned with the interface ($\alpha = 0$, figure III.10a) the conductance has a shallow dip

at zero bias for the phase shift around 0.5π and 1.5π and 3π. Indeed, the carriers normal to the interface are the one carrying the current, since they are insensitive to the d-wave nodes, the conductance is almost the same as for an s-wave superconductor with the same gap (figure 10 of [?] and figure 3 and 4 of [?]). When the superconducting nodes make a $\pi/6$ angle with the interface (figure III.10b), the conductance has a peak at zero bias but no dips when the bias is around the superconducting gap.

III.2.2 Comparison between experiment and simulation

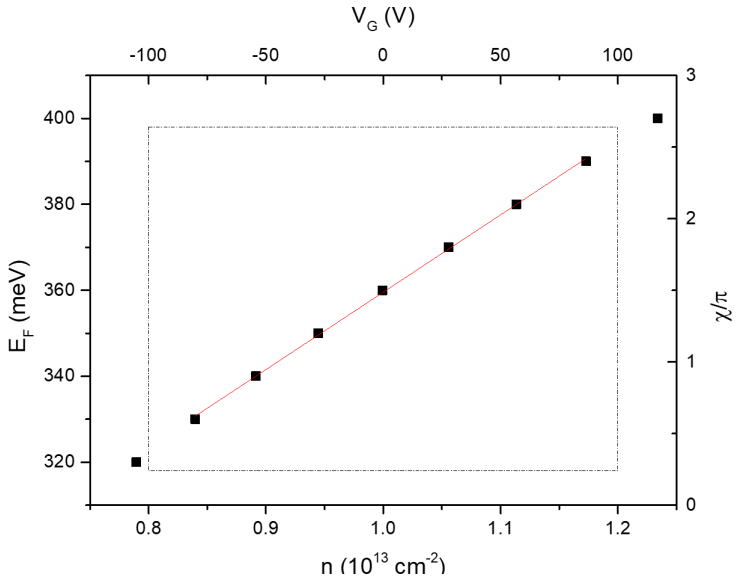

Figure III.11 – Relation between the back gate voltage, the carrier density and the graphene Fermi energy as deduced from the Hall bar measurement shown on figure III.6. The relation between the gate voltage and the phase χ is deduced from equation III.3 with a barrier width of 60 nm.

The parameters of the simulation are α the angle between the order parameter node and the interface, the doping of the graphene E_F in the (N) and E'_f in the (S) region, the width of the intermediate region w, the superconducting gap Δ.

The superconducting gap $\Delta \sim 20$ mV is known from the position of the conductance dips around zero-bias. That is in good agreement with expectations for YBCO along the c-axis [?].
From the Hall bar measurements shown in section III.1.3, we know the variation of Fermi energy E_f with gate voltage V_G:

$$\partial E_f / \partial V_G = 4 \times 10^{-4} \text{ eV/V},$$

or in an equivalent manner $\partial n / \partial V_G = 2 \times 10^{10}$ cm^{-2}/V. From the same measurement, we also know that the graphene doping without applied gate voltage is

$$n(0) = \left(\frac{E_f(0)}{\sqrt{\pi} \hbar v_F} \right)^2 = 10^{13} \text{ cm}^{-2},$$

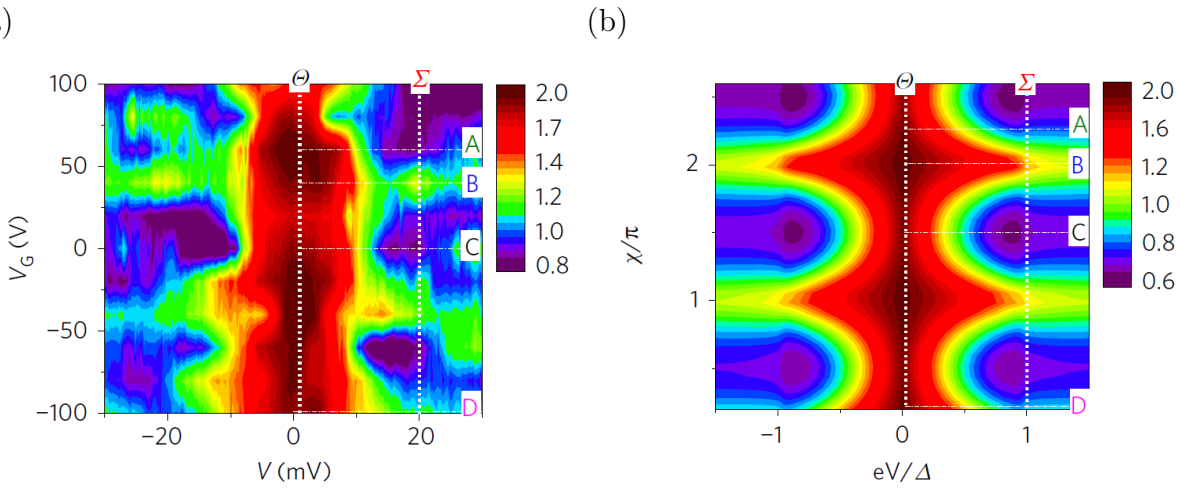

Figure III.12 – (a) Experimental conductance as a function of bias (horizontal axis) and gate voltage (vertical axis). (b) Theoretical conductance as a function of bias (horizontal axis) and phase shift acquired while crossing the barrier χ (vertical axis).

or $E_f(0) = 350$ meV. From the relations $E_f = \hbar v_F \sqrt{\pi n}$, we obtain $E_f(V_G)$ as shown on figure III.11. One sees that, in a very good approximation, E_f is proportional to V_G (red curve) within the experimental window (dashed rectangle).
From the above, and considering equation III.3, it follows that the phase shift χ must be proportional to V_G. Note that this prediction is consistent with the periodic modulation by V_G observed in conductance measurements (see figure III.7b). Thus, from simple inspection of figure III.7b, we obtain the relationship between the phase shift χ, V_G, E_F and n, which is represented by the red line in figure III.11. From the proportionality factor $\partial\chi/\partial E_F \sim 3\pi/100$ meV^{-1} and equation III.3, we estimate $w = \hbar v_F \partial\chi/\partial E_F \sim 60$ nm. The origin of the intermediate region is discussed in the section III.2.3. This intermediate region is attributed to our gate geometry and to the width of the superconductor to insulator transition.
The angle α and the Fermi energy E'_f are free parameters chosen to match the details of the experimental conductance curves.

We compare on figure III.12 and III.13 the conductance of the device to the theoretical model prediction taking into account the potential barrier at the interface. The figure III.12b shows the theoretical conductance of the SN'N structure with the parameters which we found to be the most adapted to reproduce the experimental conductance: $\Delta = 20$ meV, $E_f(0) = 15\Delta$, $E'_f = 20\Delta$, $\beta = 5\Delta/3\pi$, w = 60 nm, $\alpha = \pi/4$.

The doping E'_f in the superconducting region is chosen to reproduce the dips appearing around $\pm$ 20 mV at zero gate voltage. A higher doping $E'_F = 30\Delta$ for example on figure III.10c do not show these dips. This doping is consistent with the graphene doping from gold contact [?, ?]. Angles α far from $\pi/4$ do not show the peak at zero bias - figure III.10a - or would not show the dips around the superconducting gap for example $\alpha = \pi/6$

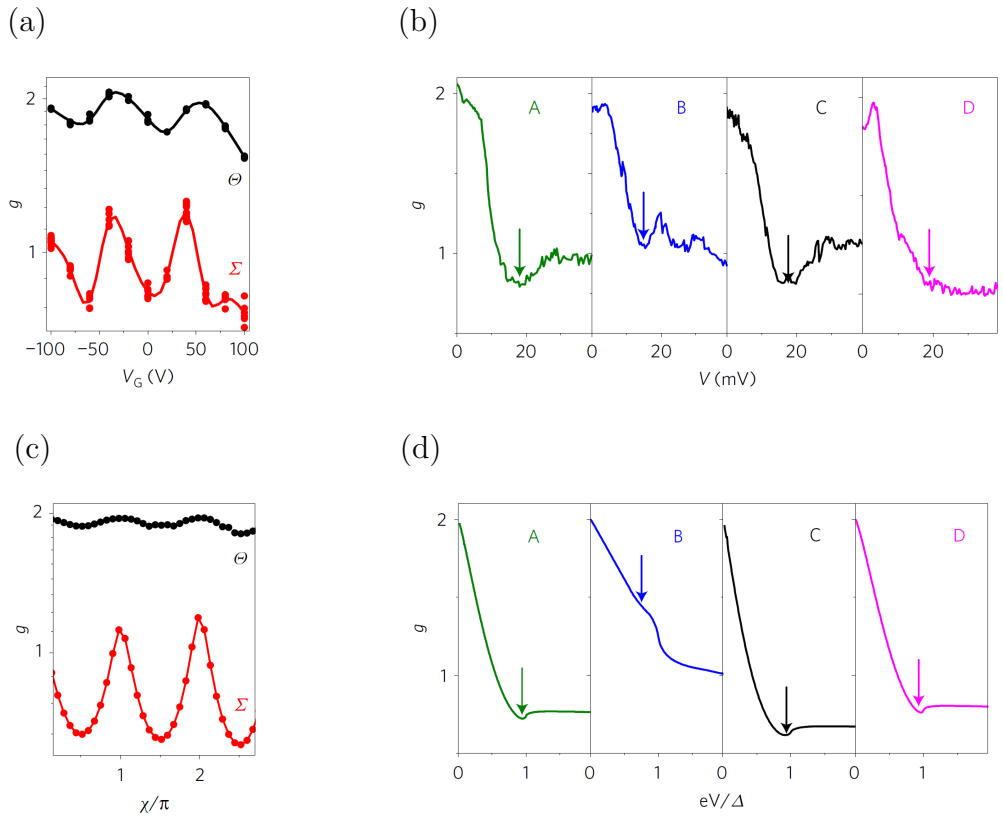

Figure III.13 – (a) Cuts of the experimental conductance at constant bias along the line denoted θ and Σ in figure III.12a. (b) Cuts of the experimental conductance at constant gate along the line denoted A, B, C, D in figure III.12a. (c) Cuts along the line θ and Σ of the theoretical conductance shown on figure III.12b. The simulation parameters are $E'_f(0) = 20\Delta$, $\alpha = \pi/4$, $E_f(0) = 15\Delta$, $\beta = 5\Delta/3\pi$, w = 60 nm. (d) Cuts along the line A, B, C, D of the theoretical conductance.

on figure III.10b. Indeed, the current is dominated by carriers close to normal incidence. For $\alpha = 0$ such normally incident carriers are not sensitive to the order parameter nodes, this is the reason for the suppression of the bound states at zero bias shown on figure III.10a.

On the contrary, the angle $\alpha = \pi/4$ reproduces many of the experimental conductance features. One recognizes on figure III.12 the peak at zero bias (in red) due to bound states at the interface between the d-wave superconductor and graphene. The dips around $eV = \pm\ \Delta$ are present at zero gate voltage, they disappear as the gate is varied and transform into secondary maxima, before appearing again around $\chi = 3\pi$ and $\chi = 0.5\pi$. At biases below -1.5Δ and above 1.5Δ, the conductance bias dependence is much weaker but it is still periodically modulated with the gate voltage. The periodic structure is striking on the line cuts at constant bias shown on figure III.13a. The periodicity subsists until the normal state (above 1.5Δ). These oscillations above the superconducting gap are the usual interferences associated with Klein tunneling in npn structures. The oscillations above 1.5Δ (not shown)

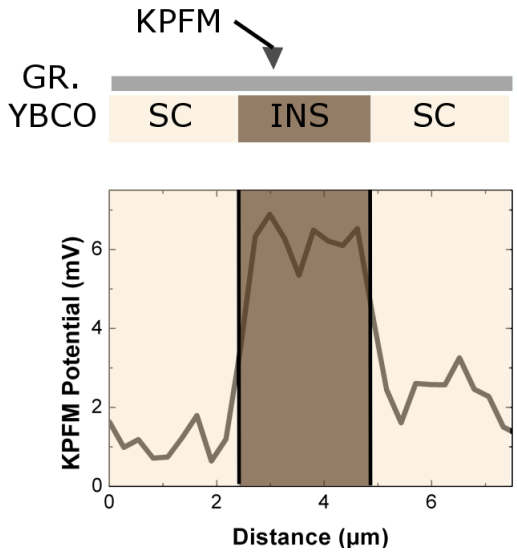

Figure III.14 – Work function difference between graphene and the KPFM tip as a function of the tip position, the image is taken by Kelvin Probe Force Microscopy. The graphene work function is higher on superconducting YBCO (S) (below 2.5 μm and above 5 μm) than on insulating YBCO (N).

are difficult to observe experimentally in our system. At low temperature, this is due to the limits of the theoretical model which considers a square barrier in the N' region whereas at high bias the barrier is probably trapezoidal. It is tempting to do the same experiment at higher temperature where the YBCO is non superconducting, one would then observe this usual Klein tunneling due to the npn structure. Unfortunately, the STO dielectric constant decreases drastically when the temperature is raised, making our gate ineffective experimentally. We estimate $\partial n/\partial V_G = 5 \times 10^8$ cm^{-2}/V at high temperature for a STO dielectric constant of 500 [**?**]. The gate is thus 20 times less effective than at low temperature which makes the theoretical period of this oscillation 800V which is not a value one can reasonably reach experimentally.

III.2.3 Origin of the potential barrier

To understand the origin of the barrier U_0, we start from the hypothesis that graphene doping is different i) on top of Au (region S), ii) on top of insulating YBCO (region N), and iii) in an intermediate region N' in between S and N. Following theory and experiments, particularly work related to Klein tunneling in graphene [8], that situation implies a potential step for electron traveling from S to N across N'.

Since Au and (insulating) YBCO are very different, it is straightforward that doping is different in "S" and "N". Indeed graphene doping is strongly dependent on the electronic and structural properties of the underlying substrate [9] and hence different doping in "S" and "N" is expected as shown on figure III.14 at room temperature.

The reason why a region N' exists with different doping as in N is not as straightforward.

Various non-exclusive explanations are plausible.

The most plausible one is that the cross-section of the device can be viewed as two contiguous capacitors having the same lower plate (back of the STO substrate covered with silver paste) but different top plates and dielectric media (see figure III.15). The first capacitor (left) has superconducting YBCO/Au as top plate and STO as the dielectric medium. At variance, in the second capacitor (right) graphene is the top plate, and the dielectric media are STO in series with irradiated YBCO. In this configuration, strong fringe field exists at the boundary between both capacitors (which corresponds to the S/N interface, see figure III.1b). Because of the fringe fields, the excess charge in the S/N interface is locally different from that induced far from it. We performed calculations using finite element software (COMSOL) from which we found that the excess charge strongly decays within the first 100 nm from the S/N interface. This effect supports the existence of an intermediate N' region at the S/N interface.

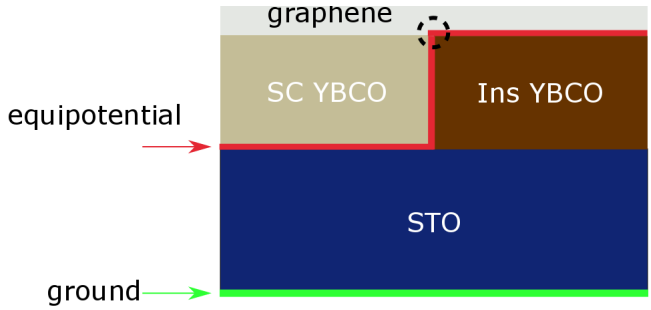

Figure III.15 – Scheme of the gate. The green and red lines indicate the equipotential associated with the ground and the gate respectively. The dashed circle depicts the edge of the equipotential where charge accumulation occurs due to stray field.

In addition to the above, the concomitance of two effects cannot be excluded:

1. The 4 nm Au layer covering superconducting YBCO forms a step with respect to uncovered, irradiated YBCO. Thus, one expects graphene to be locally corrugated and possibly "suspended", which should lead to different local doping in that region and further from the step.

2. The electronic properties of the irradiated YBCO are different within few nm of the Au step and further from it, since the boundary between irradiated and unirradiated YBCO is not sharp, but has a $\sim$ 10 nm scale characteristic size. This may lead to different local graphene doping within that region between irradiated and unirradiated YBCO.

III.2.4 Further implications

One can theoretically express - as in equation III.2.1 - the conductance of the interface as a function of the probabilities for an electron coming from the graphene side to be reflected or transmitted at the interface. The probability for an electron coming from the graphene

(a) g_A, Cooper pairs only.

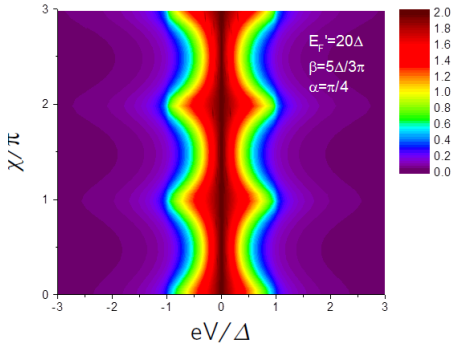

(b) g_N, normal electrons only.

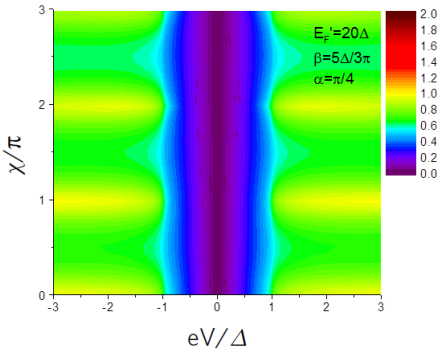

(c) $(g_A - g_N)/(g_A + g_N)$.

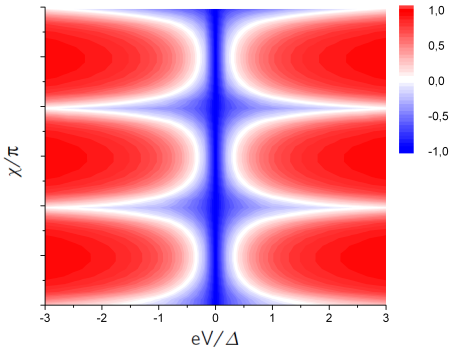

Figure III.16 – Comparison of the normal electrons and Cooper pairs contributions to the conductance. The parameters are the same as in figure III.13: $E'_f(0) = 20\Delta$, $\alpha = \pi/4$, $E_f(0) = 15\Delta$, $\beta = 5\Delta/3\pi$, w = 60 nm. At low bias (a) the Cooper pairs dominate the transport, while at high bias (b) mostly normal electrons carry the current. The ratio between the two contributions (c) shows that the transition from one regime to the other is modulated both by the gate voltage and the voltage bias. One notice in (b) that oscillations due to Klein tunneling are present at high bias as expected for normal electrons.

side to be reflected is $|r|^2$ and the probability that an electron coming from the graphene side experiences an Andreev reflection is $|r_A|^2$. By current conservation, the probability that this electron is transmitted as an electron is thus $1 - |r|^2 - |r_A|^2$. Since this process describes an electron entering directly the superconductor, such a transmitted electron has necessarily an energy higher than the superconducting gap. Note that the current carried by these electrons is usually called an excess current [**?**]. The contribution of the Cooper pairs to the total current is proportional to $2|r_A|^2$. It is due to electron scattered through the Andreev reflection process. The factor 2 comes from the conversion of one electron into one pair of charges. We can thus separate the total conductance g into two parts g_A and g_N: $g = g_A + g_N$. With,

$$g_A(eV/\Delta, \chi, E_f/\Delta, E'_f/\Delta, \alpha) = 2\int_{-\pi/2}^{\pi/2} d\theta \cos\theta_A |r_A(eV/\Delta, \chi, E_f/\Delta, E'_f/\Delta, \alpha)|^2$$

$$g_N(eV/\Delta, \chi, E_f/\Delta, E'_f/\Delta, \alpha) = \int_{-\pi/2}^{\pi/2} d\theta [\cos\theta(1 - |r(eV/\Delta, \chi, E_f/\Delta, E'_f/\Delta, \alpha)|^2) - \cos\theta_A |r_A(eV/\Delta, \chi, E_f/\Delta, E'_f/\Delta, \alpha)|^2]$$

g_A is the conductance due to Cooper pairs and g_N the conductance due to normal carriers (which thus have an energy higher than the superconducting gap). We plot both g_A, g_N, and their ratio $(g_A - g_N)/(g_A + g_N)$ on the figure III.16. This ratio is equal to 1 when only Cooper pairs transport the current and to -1 when only normal electrons carry the current. This shows how the Andreev reflection is theoretically modulated by the gate voltage. This illustrate how the potential barrier modulates periodically the probability of Andreev reflection.

III.3 Conclusion

We have fabricated YBCO/graphene devices by oxygen ion irradiation, we obtained transparent YBCO/Au/graphene interfaces. We measured the interface conductance between YBCO and graphene, in the case of a transparent interface the conductance measures the superconducting graphene/normal graphene interface. We have shown that the interface conductance modulation with gate voltage is due to electronic interferences inside a potential barrier at the interface and we interpret this modulation as Klein tunneling of Cooper pairs through this barrier.

IV – Transport through nanometric graphene/$YBa_2Cu_3O_7$ junctions

In the previous chapter, we measured the conductance of a graphene/YBCO interface by studying the transport across micrometric graphene/YBCO junctions. In this chapter, we measure graphene/YBCO junctions with nanometric distances between the superconducting electrodes. These distances range from 50 nm to 700 nm, they are of the order of the graphene superconducting coherence length such that the transport is coherent in the graphene channel. The junction fabrication process is described in chapter 2.

The nanometric graphene/YBCO junction geometry is depicted on figure IV.1. Four superconducting YBCO electrodes are separated by an insulating YBCO matrix. The superconducting electrodes are connected by a graphene sheet. The device allows doing measurement in two, three and four point configurations. Four point measurements are sensitive to the whole graphene structure consisting of a part of the graphene on the superconducting YBCO electrodes, the YBCO/Au/graphene interface and the graphene bridge. Three point measurements allowing to measure one YBCO/Au/graphene interface. Two point measurements are sensitive to the whole graphene structure consisting of the YBCO electrodes, the graphene on the superconducting YBCO electrodes, the YBCO/Au/graphene interface and the graphene bridge.

(a) Two points measurement.

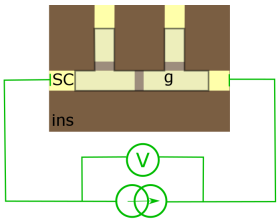

(b) Four points measurement.

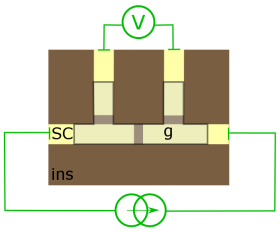

Figure IV.1 – Schematic of the YBCO/graphene junctions with the measurement geometry. Brown corresponds to insulating YBCO, yellow corresponds to superconducting YBCO, pale gray corresponds to graphene. (a) Two probe measurement geometry, (b) four probe measurement geometry.

We used a top gate to modulate the carrier density on these devices. The top gate allows to cross the Dirac point. We first estimate our top gate capacity by Hall bar measurement. We then present measurements of the YBCO/graphene device in four point measurements. The conduction measurements present two type of behaviors: i) an alternation of peaks and dips at zero bias voltage depending on the gate voltage and ii) conductance oscillations with bias and gate voltage. We compare the behavior i) to the conductance of the interface between a d-wave superconductor and graphene calculated numerically, indeed the YBCO/graphene interface contributes to the four probe geometry. We then show (ii) conductance oscillations as a function of the voltage across the junction in different measurement geometries (two, three and four points). The conductance oscillations depend strongly on the gate voltage. We interpret these conductance oscillations as McMillan-Rowell resonances inside the graphene channel. In summary, our experiments show (i) hints of a crossover from specular Andreev reflection to Andreev retro reflection and (ii) coherent transport across

hundreds of nanometers in graphene.

IV.1 Conduction of the YBCO/graphene junction: channel and interface contribution

We fabricate a top gate on top of our YBCO/graphene junctions as explained in chapter 2. We characterize our top gate via Hall effect measurement. A YBCO/graphene device with a top gate is depicted on figure IV.2c. The top gate enables us to cross the charge neutrality point. We performed two, three and four points measurements. In four point measurements, we observed either a quasiparticle tunneling conductance behavior or a conductance behavior which drastically changed with gate voltage. The quasiparticle tunneling behavior is attributed to at least one dirty interface. We interpret the second behavior as a conduction dominated by the graphene/Au/YBCO interface. We thus compute numerically the conductance of a d-wave superconductor/graphene interface.

IV.1.1 Top gate characterization

We characterize the capacity of our top gate on a Hall bar (shown on figure IV.2a) by measuring the charge carrier density n for different gate voltages V_G. The capacity of the top gate $\beta = \partial n/\partial V_G$ is extracted from a linear fit of the charge carrier density versus gate voltage curve shown on figure IV.2b, we obtain $\beta = 5.2 \times 10^{11}$ cm^{-2}.V^{-1}. This value is compatible with the one estimated for a parallel plate capacitor model taking 9 for the Al_2O_3 dielectric constant. The top gate is sufficient to cross the Dirac point with a gate voltage lower than 5 V both for the graphene Hall bars and the graphene/YBCO junctions. A typical resistance versus gate voltage curve is shown on figure IV.3. We can apply a voltage of 10 V with a leakage current lower than 1 nA on 87 % of our YBCO graphene samples.

We often convert the applied gate voltage into graphene's Fermi energy in this chapter. The graphene Fermi energy E_f is related to the carrier density n by the formula $E_f = \hbar v_F \sqrt{\pi n}$. The carrier density is proportional to the gate voltage V_G: $n = \beta|V_G - V_D|$ such that $E_f = \hbar v_F \sqrt{\pi\beta|V_G - V_D|}$, with V_D the gate voltage corresponding to the charge neutrality point. We calculated above the relation between graphene carrier density and gate voltage for the top gate: $\beta = \partial n/\partial V_G \sim 5 \times 10^{11}$ cm^{-2}.V^{-1}.

IV.1.2 Devices with a quasiparticle tunnelling conductance behavior

The YBCO/graphene nanometric devices showed different type of conductance behaviors. These behavior changes are due to the different transparencies of the graphene/superconductor interfaces. The typical conductance of the graphene/YBCO junction measured in four points displays a tunneling conductance behavior. This behavior is due to at least one of the graphene/YBCO contact being non-transparent. We observed mostly tunnel type conductance because it is hard to have two transparent contacts on the same device. As shown on figure IV.4a, the dip at zero bias voltage flatten when increasing the sample temperature

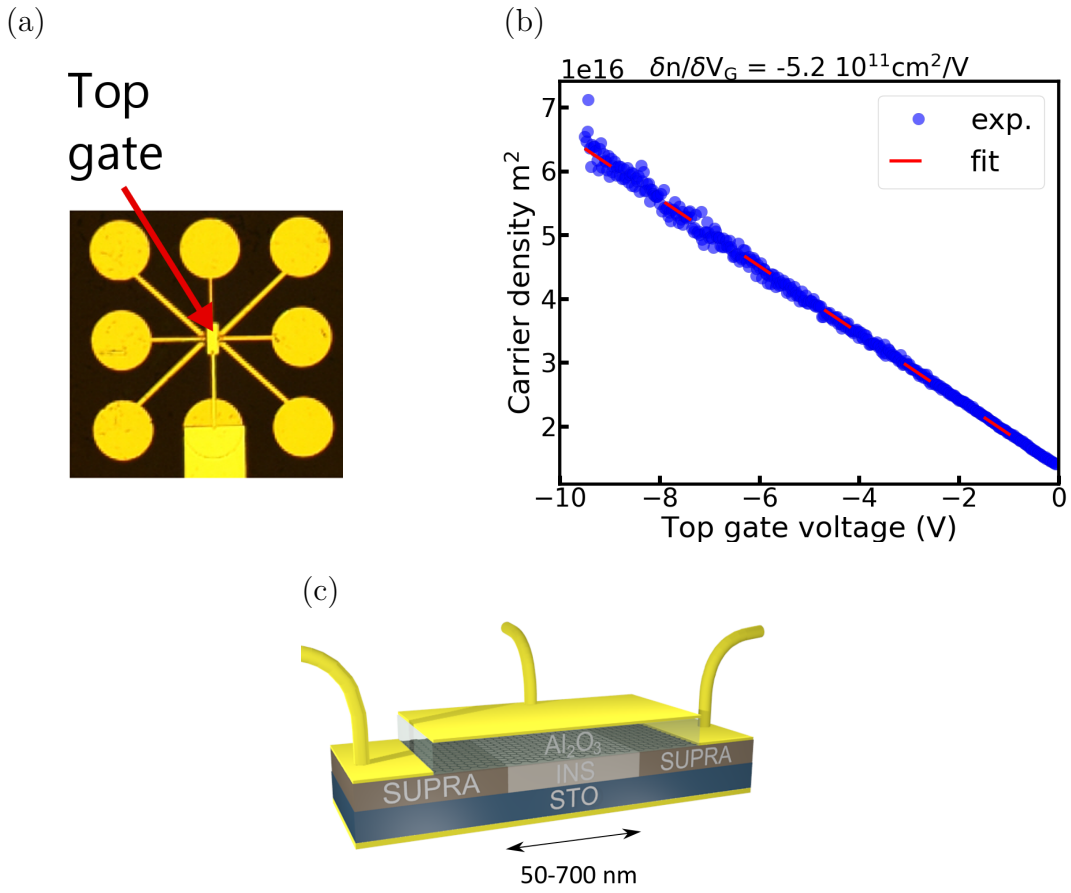

Figure IV.2 – (a) Microscope picture of the graphene Hall bar with an Al_2O_3 top gate. (b) The graphene carrier density as a function of the top gate voltage obtained from the Hall bar measurement, the dashed line is a linear fit. (c) Schematic view of a YBCO/graphene junction with an alumina top gate, the top gate extends over the whole graphene area. The graphene is connected to superconducting electrodes and is responsible of the transport over the insulating YBCO part. Only two superconducting YBCO probes are represented, the real device possess four probes. A schematic of the four probe device without the top gate is shown on figure IV.1.

above the YBCO critical temperature. We measured a transparent behavior on some sample as shown on figure IV.4b. This is more easily achieved in a three point configuration than in two or four points because one can then isolate the contribution of one transparent interface to the conduction omitting the other interface which might have a tunnel behavior.

We present on figure IV.5 the gate voltage dependent measurement of a device showing a tunnel behavior. We normalize the conductance with respect to the conductance at high bias. A gate voltage shifts the graphene sheet resistance independently of the bias voltage in general, thus we could expect that the conductance of our device does not depend on gate voltage after normalization. Instead, the normalized conductance dip in the

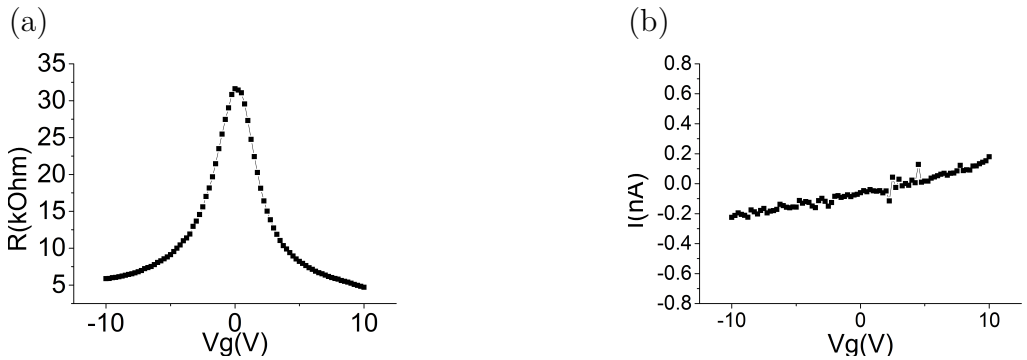

Figure IV.3 – (a) Experimental resistance versus gate voltage curves for a graphene Hall bar and (b) the leakage current from the gate. The leakage current is always below 10^{-9} A, such that the leakage current does not disturb the resistance measurements which use a current around 1 μA.

tunnel regime is larger when the graphene is close to the charge neutrality point. In the Blonder-Tinkham-Klapwijk formalism [**?**], this behavior indicates a lower transparency of the graphene superconductor interface close to the charge neutrality point. Two factors can contribute to the increase of the normalized resistance close to the charge neutrality point.

First, this can be due to an increase of the interface resistance. Indeed, the top gate covers graphene both on top of the insulating YBCO and on top of the superconducting YBCO as shown on figure IV.2c. The gate voltage shifts both the Fermi energy $E'_f \propto \sqrt{|V_G - V'_D|}$ of graphene on superconducting YBCO and the Fermi energy $E_f \propto \sqrt{|V_G - V_D|}$ of graphene on insulating YBCO. Since superconducting and insulating YBCO dopes graphene differently $V_D \neq V'_D$, the Fermi vector mismatch E'_f/E_f increases when $|V_G - V_D|$ decreases. The relation

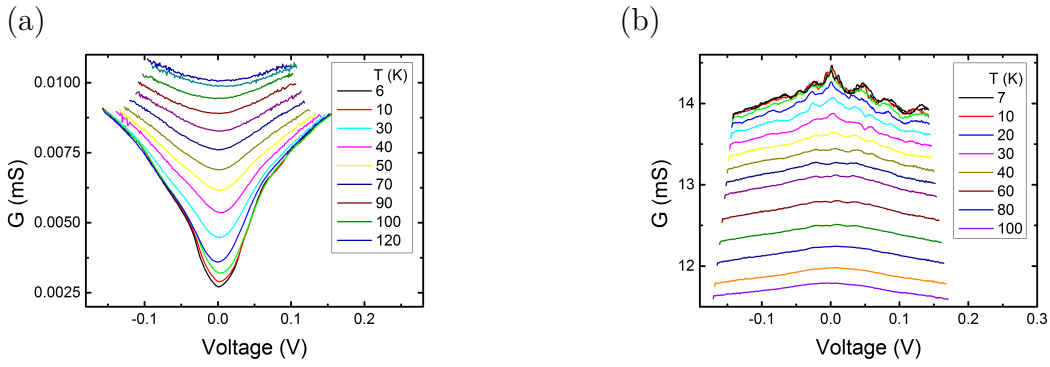

Figure IV.4 – Experimental conductance curve of YBCO graphene junction. (a) Conductance curves at different temperatures on a device measured in two points, the channel width is 200 nm. This tunnel type of conductance is attributed to a low contact transparency between the graphene and the YBCO. (b) Conductance curves versus temperature measured in three points showing a high transparency, the channel width is 150 nm.

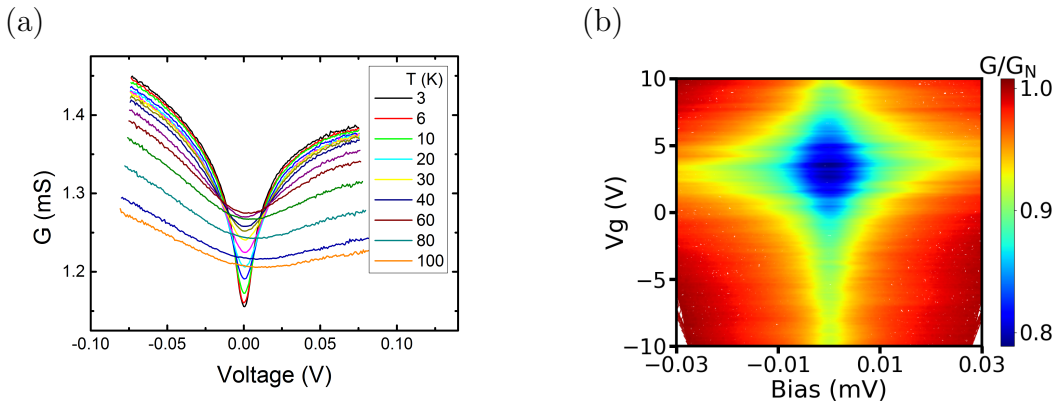

Figure IV.5 – Experimental conductance curves of a YBCO/graphene device, the distance between superconducting electrodes is 700 nm. (a) Differential conductance versus bias voltage at different temperatures measured in a four points configuration, no gate voltage is applied. (b) Mapping of the differential conductance normalized at high voltage as a function of bias and gate voltage of the same device.

linking the incident angle θ and refracted angle θ' of an electron crossing the superconducting graphene/normal graphene interface is:

$$E'_f sin(\theta') = E_f sin(\theta).$$

If the Fermi energy inside the step is higher than the Fermi energy before the step, then electrons with an incidence angle higher than $\theta_c = \arcsin(E_f/E'_f)$ will be reflected. This diminishes the conductance across the step. The top gate voltage shifts both E_f and E'_f but the ratio E'_f/E_f decreases when E_f approaches the charge neutrality point such that the θ_c decreases and the conductance diminishes.

Second, this can be due to an increase of the graphene sheet resistance. Indeed, the graphene mean free path depend on the carrier doping as shown in [**?**] (figure IV.6). The mean free path has a minimum at the charge neutrality point and has an approximately linear dependence with gate voltage. The proximitized graphene superconducting coherence length ξ is proportional to the square root of the mean free path. The coherence length thus decreases when the gate voltage increases with respect to the neutrality point.

$$l_{mfp} = \frac{2D}{v_F}$$

$$\xi = \sqrt{\frac{\hbar D}{k_B T}}$$

$$\xi = \sqrt{\frac{\hbar v_F}{2k_B T}}\sqrt{l_{mfp}}.$$

Our measurements show that the graphene between the superconducting electrodes does not become fully superconducting by proximity effect. Instead, a finite graphene part of

width ξ adjacent to the electrodes become superconducting if the interface is transparent. Hence by tuning the mean free path with a gate voltage, one adjusts this superconducting graphene width and thus the conductance G of the non-superconducting graphene part: $G = w/(\rho(L - 2\xi))$. This effect is not present at high bias where the transport is dominated by normal electrons: $G_N = w/(\rho L)$. So the normalized conductance below the superconducting gap $g = G/G_N = L/(L-2\xi)$ decreases when ξ decrease close to the charge neutrality point.

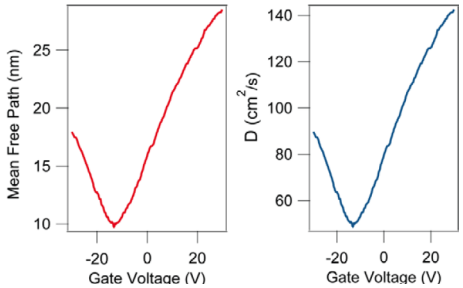

Figure IV.6 – Graphene mean free path l_{mfp} and diffusion coefficient D evolution with carrier densities as measured in [**?**], $l_{mfp} = 2D/v_F$. The diffusion coefficient is minimum at the charge neutrality point (CNP). The graphene superconducting coherence length ξ is also minimum around the charge neutrality point since $\xi \propto \sqrt{l_{mfp}}$. The diminution of ξ might explain the normalized resistance increase observed on figure IV.5b around the CNP.

IV.1.3 Experimental results on the conduction around the charge neutrality point

Some devices measured in a four probe geometry in which the graphene/YBCO interfaces were transparent showed an interesting behavior when crossing the Dirac point. The figure IV.7a shows cuts of the differential conductance as a function of bias voltage for different gate voltages for one of these devices. A peak in the conductance is visible at high positive and high negative gate voltage while the peak height decreases and alternates with a dip in the conductance close to the charge neutrality point. We show a zoom of these conductance peaks or dips on the figure IV.7b.

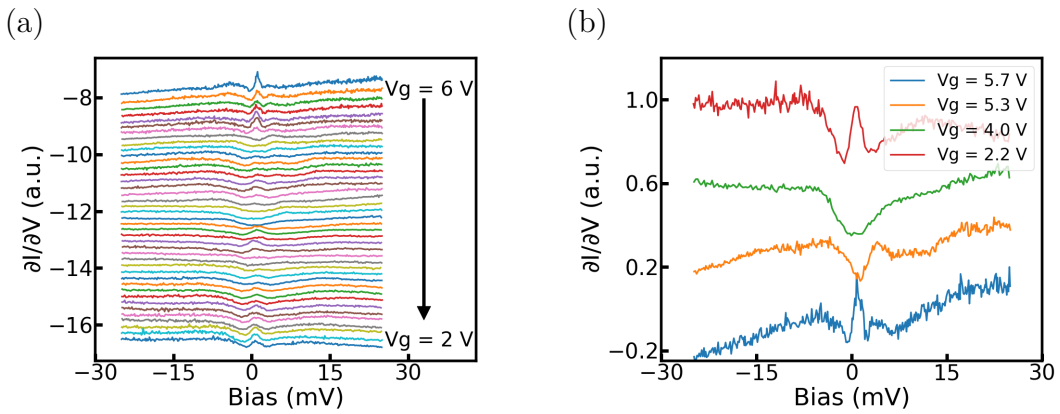

Figure IV.7 – Experimental conductance of a YBCO/graphene device, the gap between superconducting electrodes is 350 nm. (a) Differential conductance as a function of bias voltage for different gate voltages. The curves are normalized by the conductance at high bias and they are shifted for clarity. (b) Differential conductance as a function of bias voltage and gate voltage. The curves at normalized by the conductance at high bias and they are shifted vertically for clarity.

The change of the conductance bias dependence with gate voltage does not originate from the graphene bridge. Indeed, a graphene based Josephson junction would also present a peak in the conductance modulated with gate voltage but the device of figure IV.7 shows no sign of Josephson effect. The conductance behavior shown on figure IV.7 can originate from the graphene/superconductor interface because, as shown on figure IV.1b, the four point geometry measures the graphene channel in series with two YBCO/graphene interfaces. Depending on their respective conductance's, the YBCO graphene interface might have a dominant contribution to the conductance. For the YBCO graphene device presented on figure IV.7, the conduction behavior is inverted around the charge neutrality point compared with the conductance at high carrier concentration. As shown in the introduction, this change of behavior is one of the characteristics of the specular Andreev reflection. It is thus tempting to link the observed conductance behavior with the conductance of a superconductor graphene interface in the regime of specular Andreev reflection [**?**]. We compare in the next section these conductance behaviors with the theoretical differential conductance of various d-wave superconductor graphene interfaces.

IV.1.4 Model with a graphene/superconductor interface

We calculate the conductance of a d-wave superconductor/graphene interface as a function of the bias voltage and of the normal graphene Fermi energy E_f. The calculation is a simplification of the one of chapter 3 [**?**, **?**] where we considered the conductance of a d-wave superconductor/graphene interface with an energy barrier between the two conductors. The physical parameters entering the model are:

- $\Delta E_f/\Delta V_G$ the Fermi energy variation with gate voltage,
- E'_f the Fermi energy of the superconducting graphene part,
- α the angle between the d-wave order parameter and the interface,
- Δ the d-wave superconducting gap.

We use the same value as in chapter 3 for the Fermi energy of the superconducting graphene part $E'_f = 20\Delta$. We vary the normal graphene Fermi energy between $\Delta E_f = \pm\, 4\Delta$ to highlight the specular Andreev reflection regime. Experimentally, $\Delta E_f = 400$ meV $\sim \pm\, 6\Delta$.

We show on figure IV.8 the superconductor/graphene interface conductance calculated numerically for various values of the angle α between the interface and the d-wave order parameter node. In all cases, the specular Andreev reflection regime is visible as a conduction behavior change far from the charge neutrality point and around the charge neutrality point. For angles different from $\pi/4$, the conductance drops for $|E_f| < \Delta$. This conductance drop is also present in the s-wave case [**?**, **?**]. The angle $\alpha = \pi/4$ is peculiar, the peak at zero bias is always present but its width reduces until being infinitely thin at the neutrality point. Experimentally, the smearing due to finite temperature and local inhomogeneities in the graphene dopings would lead to a decrease or flattening of the peak close to the neutrality point.

The conductance as a function of bias voltage for $\alpha = 3\pi/20$ (shown on figure IV.8b) would be the one closest to the experimental conductance cuts shown on figure IV.7b. The theoretical conductance has a rounded peak at high Fermi energy and decreases at low (non-zero) Fermi energy. The discrepancies might be due to the difference between the model which considers a single graphene/superconductor interface and the measurement which consist of two superconductor/graphene interfaces in series with a normal part of graphene.

Another source of discrepancy is the graphene doping inhomogeneities which we estimate in the following. We plot on figure IV.9 the resistance versus gate voltage of the device shown on figure IV.7. A resistance maxima corresponding to the charge neutrality point is visible on the raw data. We model the experimental curve of figure IV.7 with a Lorentzian curve in order to obtain the charge neutrality point gate voltage $V_D = 3.5$ V and the curve full width at half maximum $\delta V_G = 1.8\ V$. We deduce from the Lorentzian curve width that the graphene Fermi energy dispersion can be as large as 100 meV. The conduction of the YBCO

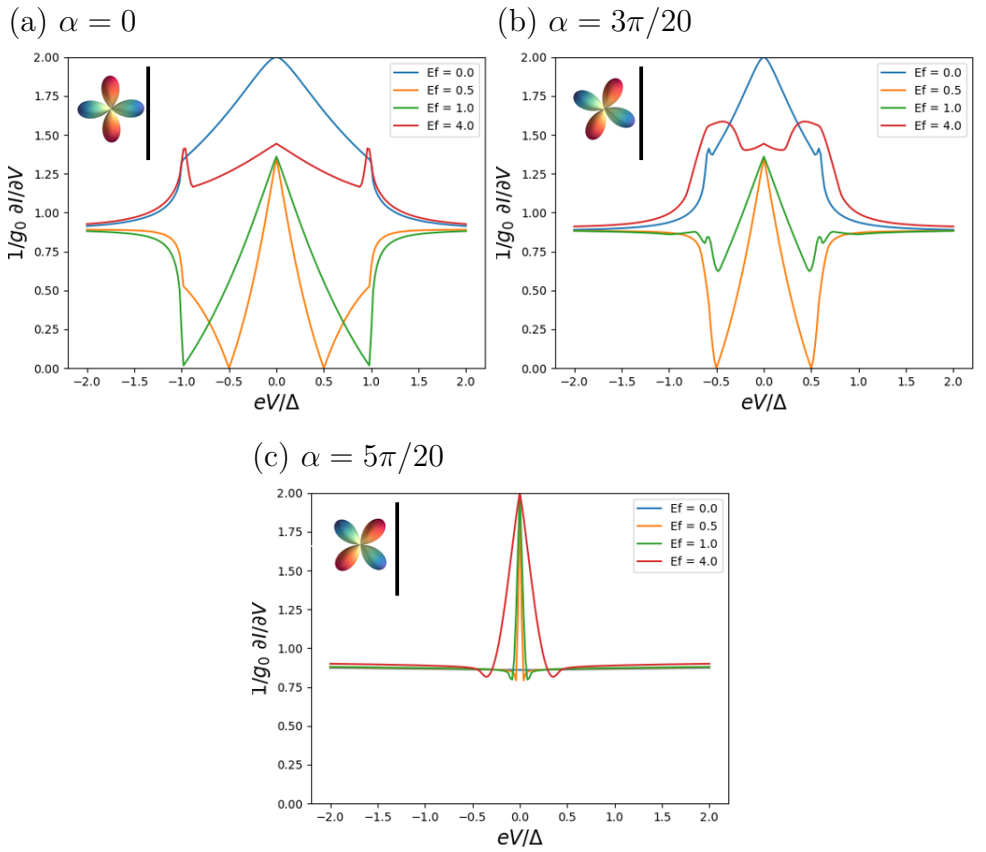

Figure IV.8 – Simulation of the differential conductance of a single transparent d-wave superconductor/graphene interface. The conductance is normalized with respect to the interface conductance when the superconductor is in the normal state, thus the conductance is flat at high bias. The angle between the d-wave order parameter and the interface is (a) $\alpha = 0$, (b) $\alpha = 3\pi/20$, and (b) $\alpha = 5\pi/20$. The specular Andreev reflection regime is visible either as an abrupt decrease of the conductance for $\alpha = 0$, $\alpha = 3\pi/20$, or as decrease of the zero bias conductance peak width around the charge neutrality point for $\alpha = 5\pi/20$.

graphene device is an average of different conduction channels with different Fermi energies. This may explain the quantitative differences between the experiment shown on figure IV.7 and the simulation shown on figure IV.8.

To summarize, we have measured YBCO/graphene junctions with a quasiparticle tunnelling behavior which we attribute to the contact transparency between YBCO and graphene. We have measured YBCO/graphene junctions which conductance behavior is similar to the theoretical conduction of a superconductor graphene junction in the specular Andreev regime.

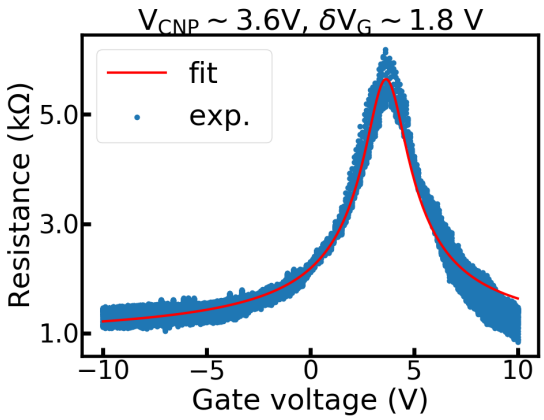

Figure IV.9 – Resistance for bias voltage smaller than 10 mV as a function of gate voltage. The Lorentzian curve (red) is a guide to the eye, its full width at half maximum of 1.8 V gives $\delta E_f \leq 100$ meV.

IV.2 Oscillations of the conductance

IV.2.1 Differential conductance oscillations with the bias voltage

We observed oscillations of the conductance in devices with transparent interfaces. These oscillations happen for voltages higher than the YBCO superconducting gap as shown on figure IV.10 and IV.11. These oscillations were measured on devices in two, three and four point measurements. As shown on figure IV.10c and IV.11a, these oscillations are suppressed with increasing temperature which indicates that the oscillations are linked to superconducting properties. We extract from a linear fit of the oscillations maxima and minima the oscillation period for all the devices. We plot on figure (shown in the section IV.2.4) the oscillation period for devices without a top gate (black triangle) and the oscillations period for devices with a top gate (black circle). In both cases, the oscillations period scales with the distance between electrodes, i.e. the oscillations happen in the graphene channel whose width changes from device to device and not inside the superconducting YBCO which geometry is fixed. As shown on figure, the oscillations period depends on the type of device (with or without top gate) which suggests an effect of the alumina top gate on the graphene properties.

We estimate the uncertainty in the voltage period by comparing the oscillation period measured manually to the oscillation period measured through an FFT, the uncertainty range is below 10 mV. We estimate our uncertainty on the graphene width to be about 50 nm. This uncertainty on the graphene width comes from the oxygen irradiation width which was estimated to be about 50 nm for our irradiation parameters for example in the thesis of J. Trastoy [**?**]. The resolution of the electron beam lithography should be smaller than 10 nm, it is negligible compared to the irradiation resolution.

As was already the case for the measurement on wide junctions presented in chapter 3, the correlation between the device resistance and the conductance behavior is rather poor. This is due to an inhomogeneous contact area between the graphene and the superconducting YBCO. The graphene channel width varies from device to device but this alone would not be

sufficient to explain these behavior discrepancies between devices with similar conductance.

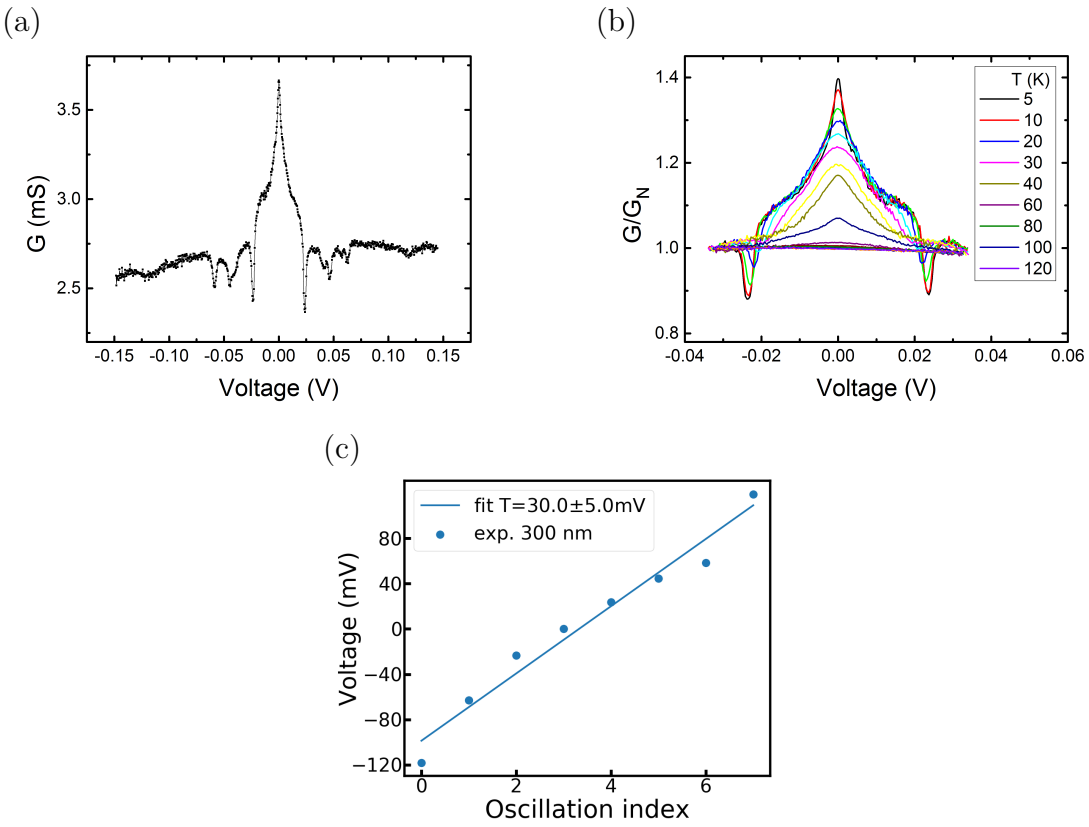

Figure IV.10 – Experimental conductance curve a YBCO/graphene device, the gap between the superconducting electrodes is 300 nm. (a) G(V) curves showing conductance oscillations, the sample is measured in a three points geometry. (b) Differential conductance normalized at high bias of the same device measured at different temperatures. (c) Position of the oscillation minima and maxima, the linear fit of the resonance in bias voltage gives a period of 30 mV.

IV.2.2 Conductance oscillations with gate voltage

The oscillations are strongly dependent on gate voltage. This indicates that the oscillations arise in the graphene channel. These oscillations are washed away by increasing the temperature. The conductance as a function of temperature drops above the superconducting transition temperature because the measurement geometry includes a superconducting YBCO electrode. The oscillations and their periods dependence on magnetic field is weak.

We present on figure IV.11 measurements of one particular junction where the gap between the superconducting electrodes is of 300 nm. The conductance oscillations become fainter and fainter as the temperature is increased as seen on figure IV.11a. There is a dip at zero bias in the differential resistance for all gate voltages as visible on figure IV.11b. The oscillations in the differential conductance depend on both the gate voltage and the bias voltage as seen on figure. The dependence with gate voltage is more pronounced above ± 40 mV which is around the YBCO superconducting gap. This suggest that the particles path leading to interferences is different in the superconducting state.

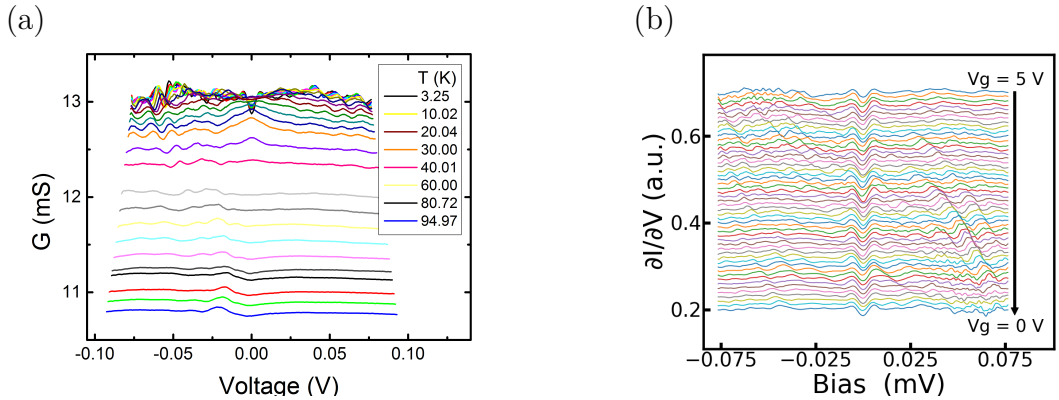

Figure IV.11 – Experimental conductance curves for a YBCO/graphene device whose channel width is 300 nm. We measure the device in a three points geometry. (a) Differential conductance versus bias voltage at different temperatures. (b) Differential conductance for different gate voltage as a function of the bias voltage of the same device measured in three points. The curves are vertically shifted for clarity.

IV.2.3 Mechanisms leading to oscillations in superconductor/normal metal stacks

We review and analyze the different phenomena that can lead to resonances and thus to oscillations in the conductance of a superconductor/normal material junction:

1. They are the multiple Andreev reflections (MAR) which are due to electrons oscillating in the normal material between two superconductors before the electrons reach an energy sufficient to enter the superconductor (figure IV.13a). The conductance maxima are located at biases $eV_n = 2\Delta/n$ with n the number of bounces the particles made

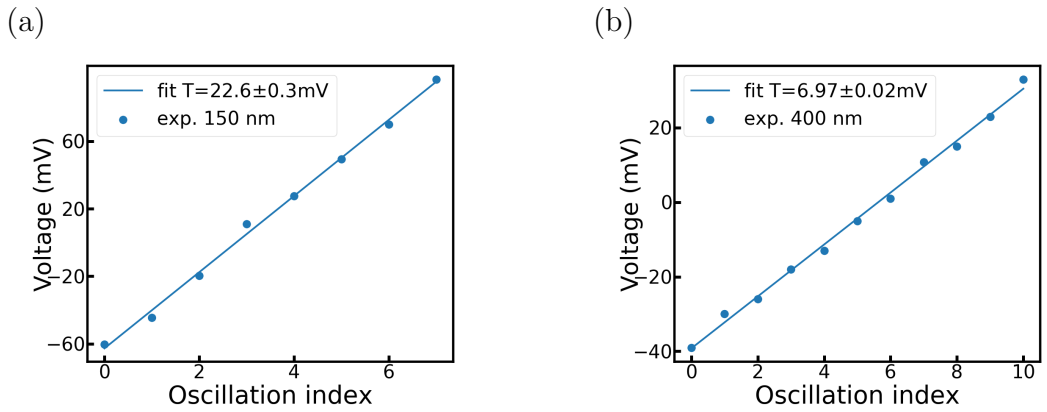

Figure IV.12 – Oscillation minima and maxima as a function of the oscillation index for two devices with a top gate measured in three point geometry. The line is a linear fit used to extract the voltage period. The oscillations scales linearly with bias voltage, the distance between superconducting electrodes is (a) 150 nm and (b) 400 nm. The oscillation period is (a) 22.6 mV and (b) 7 mV.

before crossing the junction and Δ the superconducting gap. The voltage at which resonances appear are smaller than $2\Delta/e$. These MAR are known to be precursors of the Josephson current in a device, they appear around the superconducting branch of the IV characteristics [**?**, **?**]. The resonances should not depend on the graphene's doping or length but only on the energy difference of the particles before and after entering the normal material eV. They were already observed in graphene superconductor junctions [**?**] and indeed no gate voltage dependence was observed.

2. They are also Tomasch resonances [**?**, **?**] which correspond to quasi-particle interferences inside the superconductor. The scheme of Tomasch interferences is shown on figure IV.13b. An electron impinging on the superconductor can be Andreev reflected as a hole, in which case a pair of quasi-particles enters the superconductor. The quasi-particle pair is then reflected at the insulator interface. When the pair impinges on the normal material it can either be transmitted or reflected, if the pair is reflected, it will then again be reflected on the insulating interface etc. All the quasi-particle pair trajectories interfere among themselves which results in the Tomasch resonances. The Tomasch resonances are appearing in the differential resistance of a sample at the bias voltages:

$$eV_n = \sqrt{\Delta^2 + \left(\frac{nhv_F^S}{2d_S}\right)^2},$$

with v_F^S the superconductor Fermi velocity, d_S the superconductor thickness and Δ the superconducting gap, n is the number of round trips. In the case of a graphene superconductor junction, these resonances frequencies and amplitudes should not depend on the graphene's doping or on the gate voltage since they are involving only

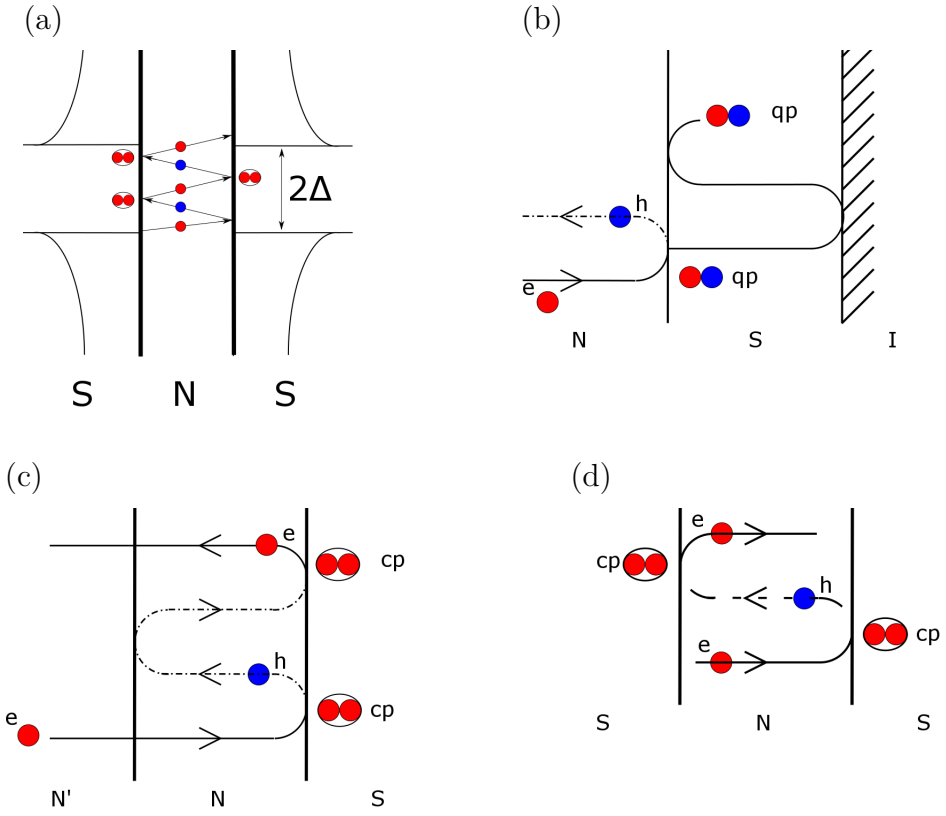

Figure IV.13 – Different mechanisms responsible for interferences in superconductor/normal junction. (a) Multiple Andreev Reflections are reflections of normal particles with sub gap energies inside an SNS junction. Electrons (in red) and holes (in blue) are converted into each other at each Andreev reflection, they gain the energy eV each time they cross the normal material. An electron entering the normal material from the left has to bounce several times on the interfaces before acquiring an energy higher than 2Δ and entering the superconductor on the right. The resonance condition is $eV = 2\Delta/n$ with n the number of round trip inside the normal material. (b) Tomasch resonances are quasiparticle interferences happening inside a superconductor in contact with a normal metal and an insulator. In our case, the interfaces would be with graphene (normal, N) on one side and with STO (insulator, I) on the other side. The resonance condition is $eV = \sqrt{\Delta^2 + \left(\frac{nhv_F^S}{2d_S}\right)^2}$ with v_F^S the Fermi velocity, d_S the thickness of the superconductor and n is the number of round trip inside the superconductor. (c) McMillan-Rowell resonances are normal particle interferences inside a normal metal in contact with a superconductor. Electrons (respectively holes) are Andreev reflected at the superconductor interface into holes (respectively electrons). Since an electron can only interfere with an electron and not with a hole, McMillan-Rowell resonances require classically two round trips inside the normal metal. (d) In our case, N' is also a superconductor, particles can be Andreev reflected at both interface such that one round trip is sufficient for interferences. The resonance condition is thus $eV = \frac{nhv_F^N}{2d_N}$ with v_F^N the Fermi velocity, d_N the width of the normal material and $2n$ the number of round trips.

the superconductor. The Tomasch resonances do not scale linearly with the oscillation index n.

3. Another source of oscillations in the conductance of a normal material/superconductor stacks are McMillan-Rowell resonances [**?**]. These resonances happen in the proximitized normal material. In this case, the particles are not normally reflected on the superconductor, but Andreev reflected such that this phenomenon shows a transfer of correlations from the superconductor to the normal material. When the particle is Andreev reflected on the superconductor it changes nature from electron to hole such that it cannot interfere with the incoming particle. It thus has to be reflected once normally and then Andreev reflected for interferences to occur. This process involves four crossings of the normal material and the voltages associated with the resonances are:

$$eV_n = \frac{nhv_F^N}{4d_N},$$

with v_F^N the Fermi velocity in the normal material, d_N the normal material thickness, and $n/2$ the number of round trip. In our case the situation is slightly different because we are looking at oscillations possibly in a normal material between two superconductors, thus the particles can in principle be Andreev reflected at each interface. An electron from the graphene impinging on the superconductor can be Andreev reflected as a hole on the first interface, the hole travels until the second interface where it is Andreev reflected as an electron which can now interfere with the incoming electron. This process analogue to the McMillan-Rowell resonance implies only one round trip in the normal channel thus the condition to have a resonance becomes:

$$eV_n = \frac{nhv_F^N}{2d_N}.$$

As shown in the appendix C, this equation is valid for a superconductor/graphene/superconductor junction. The authors of [**?**] found a larger Fermi velocity in InAs-GaSB when deduced from the McMillan-Rowell oscillation period compared to the Fermi velocity deduced from Shubnikov de Haas oscillations. They attribute this deviation to their relatively small Fermi energy $E_f/\Delta \sim 20$. The original calculation of Rowell [**?**, **?**] suppose $E_f/\Delta \to \infty$, so it is possible that deviations from equation IV.7 and the McMillan-Rowell theory appear at lower Fermi energy.

IV.2.4 Comparison between the mechanisms and the experiments

We rule out the possibility that the observed oscillations are multiple Andreev reflections because the observed resonances appear mainly for bias voltage higher than twice the superconducting gap contrary to what happens in multiple Andreev reflections. In addition, the frequency of the multiple Andreev reflections should be independent of the graphene channel, it depends only on the superconducting gap and on the interference index: $eV = 2\Delta/n$.

We compare on figure the oscillation frequencies obtained in devices of different graphene widths with the theoretical frequencies associated with Tomasch resonances. The Tomasch resonances are not periodic, we therefore calculate a pseudo-period range as the minimum and maximum voltage difference between two successive resonances. The pseudo-period range from 7 mV to 18 mV for a YBCO thickness of 50 nm and a YBCO Fermi velocity of 5×10^7 m.s^{-1}. We do not think that the oscillations we observe could be explained by Tomasch resonances. First, the experimental oscillations seem to be periodic with a period systematically higher than the theoretical pseudo-period. Second, contrary to the experimental case, the theoretical pseudo-period does not depend on the graphene channel width since the effect is occurring in the superconductor solely. Third, the range of variations of the experimental oscillation period - about 40 mV - is much higher than the range of variations of the theoretical oscillation period - about 10 mV. We do not think that a systematic effect could explain all these discrepancies.

The bias and gate voltage dependance of the oscillations are compatible with McMillan-Rowell resonances:

1. The conductance oscillations shown on figure IV.10 and IV.11 are periodic in bias voltage as shown on figure IV.12. We plot the oscillation period as a function of graphene width for the different devices on the figure. The oscillation period decreases when the graphene bridge length increases.

2. The observed oscillations dependence on gate voltage implies that they are occurring in the graphene channel. The expected superconducting coherence length in graphene is of several hundreds of nanometers [**?**] such that these oscillations could be due to Cooper pairs or quasi-particle interferences between the superconducting electrodes (McMillan-Rowell oscillations).

We therefore compare on figure the experimentally measured oscillation frequencies with the theoretical frequencies associated to McMillan-Rowell resonances. There is a systematic shift between the theoretical and experimental values in the case of the devices without a top gate. However, the variation range of both theoretical and experimental frequencies seems compatible. The systematic shift can be explained by different factors including our measurement geometry and the Fermi velocity of graphene on YBCO. The theoretical oscillation periods for a graphene Fermi velocity of $v_F = 1.5 \times 10^6$ m.s^{-1} gives the best agreement with the experimental points with a top gate as shown in figure. The theoretical oscillation periods for a graphene Fermi velocity of $v_F = 5 \times 10^6$ m.s^{-1} gives the best agreement in the case of devices without a top gate as shown in figure. As shown in [**?**], graphene Fermi velocity depends on the substrate graphene is lying. It varies between 1×10^6 m.s^{-1} for graphene on SiC and 3×10^6 m.s^{-1} for suspended graphene [**?**]. Therefore, graphene Fermi velocity might be modified by the top gate dielectric. A possible explanation in addition to a renormalization of graphene Fermi velocity is that the measured voltage period is larger than the theoretical one because we are measuring an additional resistance (the YBCO/Au/graphene interface for example) in series with the graphene bridge. This additional resistance would increase the measured period by a constant proportionality factor but would not change the

global decrease of the oscillation period with the graphene bridge length.

In summary, the experimental oscillations period decreases with increasing graphene channel width. As shown on figure, the experimental points follow the theoretical trend. The discrepancies between the oscillation period of the devices with and without a top gate could come from a change in graphene Fermi velocity on YBCO. Indeed, the theoretical curve for $v_F = 1.5 \times 10^6$ m.s^{-1} (respectively $v_F = 5 \times 10^6$ m.s^{-1}) is the closest to the experimental points with a top gate (respectively without a top gate). The agreement between experiment and theory indicates that the oscillations come from McMillan-Rowell resonances.

IV.3 Conclusion and outlook

We have measured the conduction across nanometric YBCO/graphene junctions. These junctions conductance showed both tunnel type conductance and oscillations of the conductance as a function of both bias voltage and gate voltage. We interpret these conductance oscillations as McMillan Rowell interferences inside the graphene channel. It is not straightforward to study the interplay between McMillan-Rowell resonances and their gate voltage dependance in graphene. This is possible in the framework developed by Linder and Sudbo in [?] as shown on figure IV.14. The authors of [?] study the conduction across a superconductor/graphene interface with a finite width potential barrier in between. In principle, the theory [?] is not bound to Fermi energy higher than the superconducting gap contrary to the usual McMillan Rowell theory [?, ?]. We intend to compare this model with our experiment in the near future.

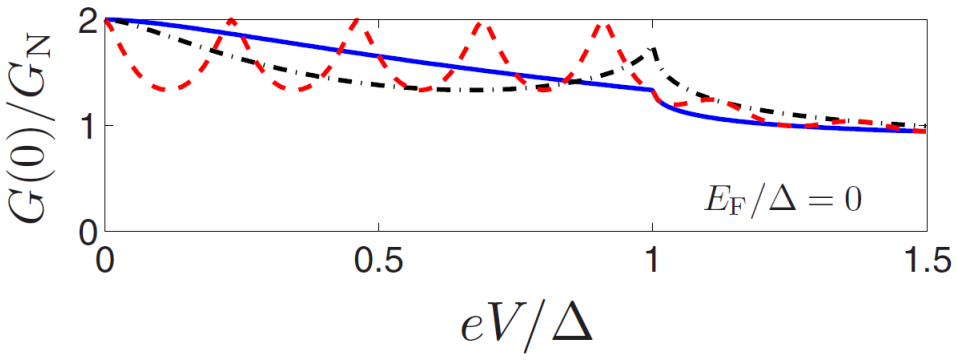

Figure IV.14 – Theoretical conductance of a graphene/superconductor structure with a finite width potential barrier in between. The conductance oscillation with bias voltage correspond to McMillan-Rowell resonances. Image adapted from [?].

The next step in the experimental study of these YBCO/graphene nanometric junctions is to look for a supercurrent in the hundred's millikelvin range. We estimate in the following the critical current these junctions might sustain. The size of our junctions (50-700 nm) is of the order of the superconducting coherence length in graphene. The coherence length is

given by $\xi = \sqrt{\frac{\hbar D}{k_B T}}$, thus ξ is of the order of 270 nm at 4 K and about 3 μm at 20 mK. Dubos et. al. [**?**] calculate for a normal metal in contact with two superconductors the product $I_C R_N/\Delta$ as a function of the temperature $k_B T$, of the superconducting gap Δ and of the Thouless energy $E_{th} = \hbar D/L^2$ with L the junction length. In our case, $k_B T/E_{th} \sim 0.03 - 0.3$ at 4 K for junction size between 50 nm and 200 nm. According to [**?**], the critical current should then not limited by thermal effects but by the Thouless energy. It was recently shown in [**?**] that the critical current in graphene is reduced compared to a normal metal with the same parameters (E_{th}, R_N, T). We estimate our Thouless energy to be between 0.6 meV and 10 meV for junction size between 50 nm and 200 nm. We deduce from the graph 2 of [**?**] that $I_C R_N/\Delta$ is between 0.1 and 0.03. For a normal state resistance of 1 kΩ and a superconducting gap of 30 meV, this condition leads to a critical current between 3 μA and 90 nA. The difficulties to observe a supercurrent comes on the one side from the low temperature required which implies to work in the millikelvin range in a radio frequency shielded environment and on the other side from the ratio of junctions with transparent to non transparent interfaces which require to measure different junctions to find a junction with transparent interfaces.

V – Towards BSCCO/BSCCO Josephson junction

We developed an exfoliation process to fabricate $Bi_2Sr_2CuO_{6+x}$ (BSCCO) junctions. These are intended to be ϕ-Josephson junction where the order parameters on the side of the junction are misaligned by an angle ϕ as shown on figure V.1b. The π-junction principle is described in the introduction and in the literature [**?**]. The ϕ-junction principle is very similar, the critical current behavior of a normal Josephson junction with magnetic field can be described as $I_c = sinc(\Phi/\Phi_0)$ with Φ_0 the elementary flux quantum. In a ϕ-Josephson junction, the critical current evolves as a function of magnetic field of flux Φ as $I_c = sinc(\Phi/\Phi_0 + \phi)$. We did not measure a supercurrent in these BSCCO junctions yet.

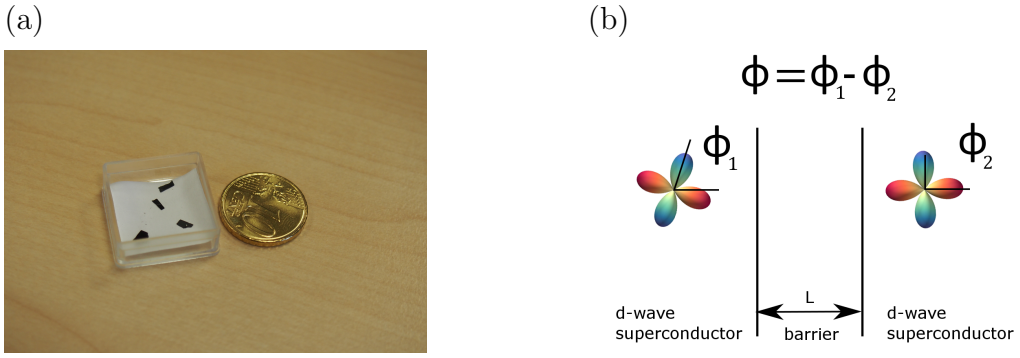

Figure V.1 – (a) Microscope picture of the BSCCO single crystals before we exfoliate them onto SiO_2. (b) Schematic principle of a ϕ-junction. The superconducting order parameters on the two side of the junction are misaligned by an angle ϕ which results in a current spontaneously circulating inside the junction.

V.1 Bilayer exfoliation process

We use the "scotch tape method" [**?**] to exfoliate BSCCO few layers onto an SiO_2 substrate. The scotch is the E-mask RP 301 by the brand Nitto. The BSCCO was provided to us[1] under the form of single crystal of typically 3×3 mm^2 shown on the picture V.1. The exfoliated BSCCO density is large enough that is possible to randomly superimpose BSCCO layers by exfoliating several times BSCCO onto the same SiO_2 substrate. Statistically one sample out of three possess a junction. In other words, we need to exfoliate the BSCCO three times onto the first BSCCO flakes layer to obtain a superposition. The superposition process success rate is thus about 33 %.

We describe the junction fabrication procedure in the following. The fabrication process is illustrated on figure V.2. We start by exfoliating BSCCO onto a 5×5 mm^2 SiO_2 sample. We take several pictures - shown on figures V.2a, V.2b - of the BSCCO flakes produced by this first exfoliation with an optical microscope. We then rotate our scotch tape with respect to the sample compared to the first exfoliation. The crystalline angle of the BSCCO deposited during the second exfoliation are thus doing an angle of about 90 ° with the axes of the previously deposited BSCCO. Once we did this second exfoliation, we do another

[1] by Kees van der Beek who works in the Laboratoire des solides irradiés

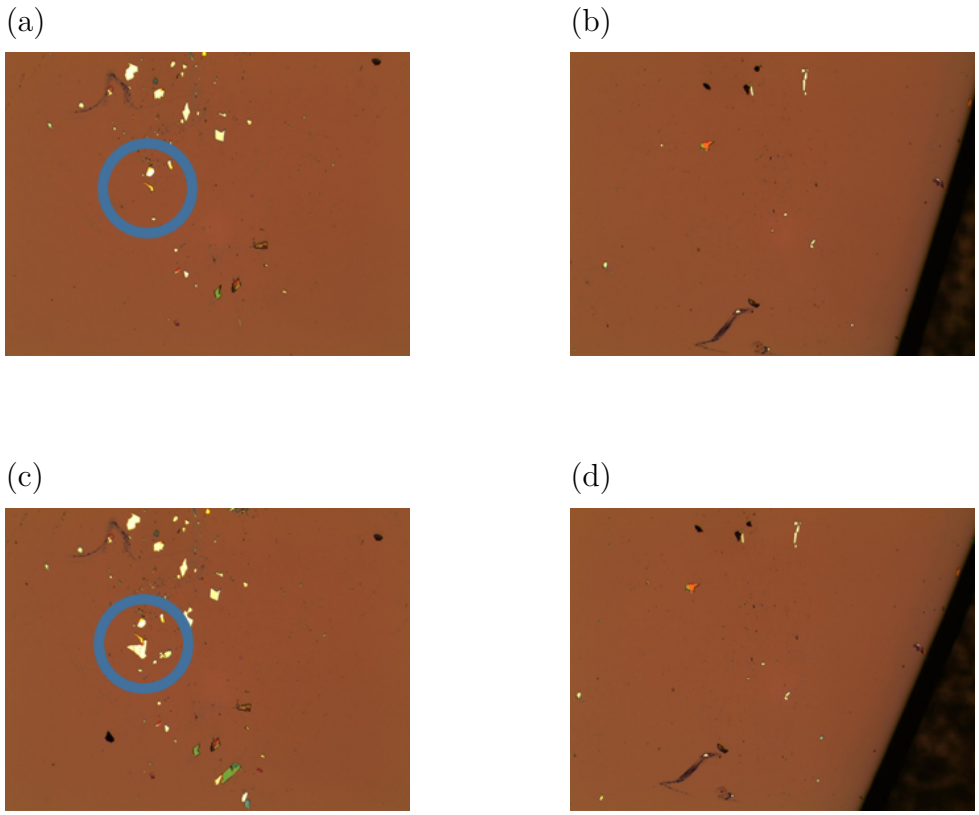

Figure V.2 – Microscope pictures of the BSCCO exfoliation process. (a), (b) are pictures taken at different positions on the substrate after seven BSCCO exfoliations. (c), (d) are pictures of the same positions after eight exfoliations. One notice between (a) and (c) the appearance of a new flake superposed on an old one, this superposition is inside the blue circle on the pictures. Other flakes are appearing in other pictures but these flakes are not superposed to previously exfoliated ones.

cartography of the sample with the microscope shown on figure V.2c, V.2d. We compare the pictures after one and two exfoliations to look for new flakes and overlaps between old and new flakes. We repeat these steps until we find a BSCCO superposition, an example is shown on the figures V.2a, V.2c. Using a new scotch piece significantly helps the BSCCO deposition onto the SiO_2 and thus increase the superposition rate.

V.2 Electrode deposition on BSCCO by laser lithography

The superposition's position, orientation and shape depend on the sample since the superposition's are produced by mechanical exfoliation. We use a laser lithographic setup Dilase 650 from KLOE design. The laser lithography set-up and the lithography parameters are described in chapter 2. After the lithography, a plasma step, with parameters 150 sccm O_2, 21 sccm Ar, 400 mT, 600 W, 80 °C during 2 minutes, clean the resist openings in order to

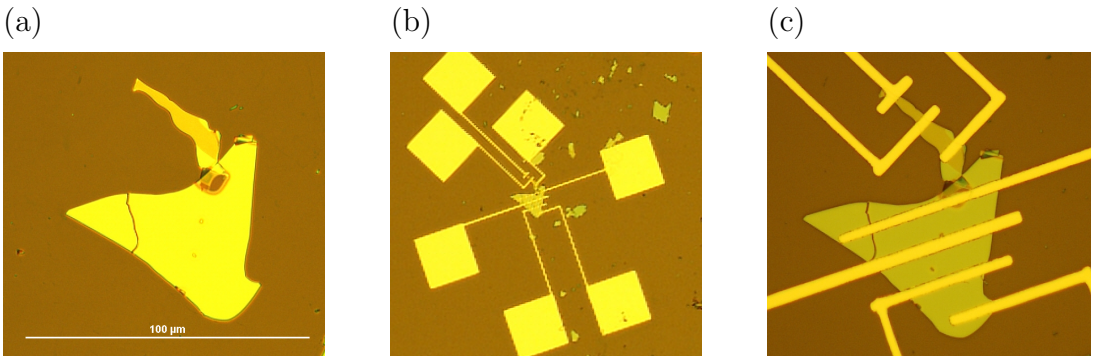

Figure V.3 – Microscope pictures of the same BSCCO junction that is used to explain the exfoliation process on figure V.2. (a) Zoom on the junction, this picture is used to design the lithographic mask numerically. The overlap between both flakes is clearly visible as a change of the optical contrast of the top BSCCO layer (on the bottom of the picture) from yellow to brown when the top flake superposed with the bottom flake. (b) Deposition of electrodes onto the junction. The electrodes design allow to perform four points measurements with the junction in between. (c) Zoom on the junction electrodes. Three electrodes on the bottom flake and four electrodes on the top flake should allow to check that the top flake is superconducting by four point measurements and to measure the junction itself in four point measurements with two electrodes on each flakes. Care has been taken that the electrodes do not overlap with the superposing region.

improve the contact between BSCCO and metal. We clean the sample with an ionic scouring at 200 V, 110 mA for 1 min before depositing 20 nm of Ti and 80 nm of Au by evaporation. The metal on top of the resist is removed in acetone with a pipette, a picture of the final device is visible on figure V.3c.

V.3 First BSCCO flakes measurement

Only few measurements on BSCCO flakes were made because of the difficulty to obtain a good contact between our metallic electrodes and the BSCCO. We connected successfully a single BSCCO flake with the lithography process described above. The flake showed a superconducting transition around 80 K when measured in a four probe geometry. The resistance showed an increase when a magnetic field orthogonal to the CuO_2 plane was applied as expected from [**?**, **?**].

We also measured a BSCCO/BSCCO junction in a four probe geometry. Unfortunately, the contact resistances and the junction resistance were in the MΩ range. The junction resistance displays an increase when a magnetic field orthogonal to the junction is applied. It is not possible to conclude if this behavior comes from the junction or the contacts because of the high contact resistance. These measurements are presented on figure V.4.

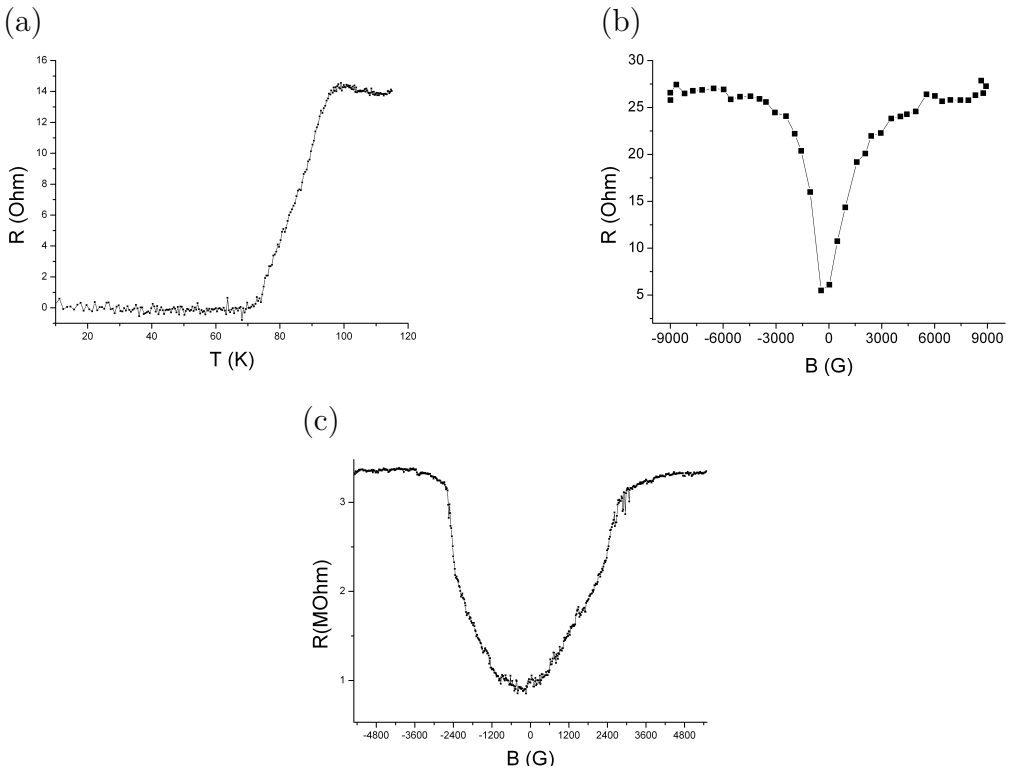

Figure V.4 – (a) Resistance versus temperature of a single BSCCO flakes measured in a four point geometry. The BSCCO becomes superconducting between 75 and 90 K. (b) Resistance versus magnetic field measurement of the same sample. There is an abrupt increase of the resistance with increasing magnetic field. The magnetic field is orthogonal to the junction. (c) Resistance versus magnetic field of a BSCCO/BSCCO superposition. Even though it was not possible to measure a critical current from the IV characteristics, the resistance versus field displays a decrease in resistance at zero field. This could be due to the superconducting properties of the BSCCO.

VI – Conclusion

We have presented the fabrication methods and the electrical measurements of junctions between YBCO and graphene. We fabricated junctions with spacing between electrodes of about 5 μm by optical lithography and spacing between 50 nm and 700 nm by electron-beam lithography. We eventually achieved good contact transparencies between YBCO and graphene. We also fabricated top gates on these YBCO graphene devices by using ALD to deposit alumina on the graphene and electron-beam lithography to deposit the metallic electrodes. Our devices showed different conduction regimes depending on the distance between superconducting electrodes and on the measurement geometry. In large junction – about 5 microns' width – we measured the differential conductance of a single YBCO/graphene interface. We observed conventional quasiparticule tunneling for low transparency junctions and d-wave Andreev bound states for high transparency ones. In the latter case, the modulation with gate voltage evidenced tunneling of superconducting pairs in the regime in which one has Klein tunneling for normal carriers. In shorter junctions with good transparencies, we measured oscillations of the differential conductance as a function of both bias voltage and gate voltage. These oscillations are interpreted as McMillan-Rowell resonances inside the normal part of the graphene channel. These oscillations indicate that the proximity effect in the graphene extends between the two YBCO electrodes.

Future experiments on these subjects could explore different paths. For the YBCO/graphene junctions, measuring more junctions in the 0.1 K range might lead to observe a supercurrent. A next step would be to build YBCO/graphene π-junctions. This could be done using a YBCO twin crystal or by using a scheme similar to the one used in [**?**] with niobium and described in the figure 3 of the introduction. All these possibilities would be easier if the superconducting coherence length in graphene would be longer. This can be done by lowering the temperature or by improving the graphene quality. The best graphene quality achieved use graphene encapsulation between HbN or the suspension of graphene between two pillars. These techniques are not compatible with the transfer of graphene onto YBCO. However, it could be possible to exfoliate BSCCO onto such structures. Hence, obtaining low contact resistance between BSCCO and graphene would be a tedious but interesting goal. Among them, it would be satisfying to complete the path toward BSCCO ϕ-junctions. It would be necessary to improve the BSCCO junctions fabrication in order to achieve better metal/BSCCO contacts and possibly better contact between the two BSCCO flakes.

Given the advance of the published research in the last years on magnetic field focusing in graphene and on superconductor/graphene junctions [**?**, **?**, **?**], it now becomes reasonable to consider an angle resolved study of Andreev reflection in superconductor/graphene junction. Studies about magnetic field focusing in graphene and studies about crossed Andreev reflection suggest that the fabrication techniques are compatible. Combining these fabrication techniques would enable to study magnetic field focusing from graphene onto a superconducting reflector. One would then access the angle dependence of the Andreev reflection in graphene and have a clear signature of the specular Andreev reflection. In particular, the study about magnetic field focusing through a pn junction [**?**] used a hBN encapsulated graphene with a spacing between metallic electrodes about 1 μm according to figure 1c of [**?**]. Two works demonstrated edge contact to hBN encapsulated graphene [**?**, **?**] with electrode size of respectively 100 nm and 2.4 μm. Theoretically, if one would build a superconducting edge between two metallic electrodes of the device used in reference [**?**], it would be possible

to study the transition from retro reflection at low temperature to normal specular reflection above the superconducting temperature. It would also be interesting to study experimentally the angle dependence of the Andreev reflection when the graphene Fermi energy is varied.

A – Description of the low temperature transport set-up

We use a cryostat SHI 950T from the Janis research company. The sample is in a Helium gas environment such that some Helium liquefy at the cryostat's bottom at low temperature. A cryocooler chill down a cold finger connected to the inside of the chamber through a copper thermal strap. It takes typically about 3 hours to cool down a sample from 300 K to 5 K and 5 hours to heat up the sample from 3.2 K to 276 K. To reduce the heating time, the heat up procedure is to turn the compressor off and stabilize the temperature of the sample at 300 K with the heaters.

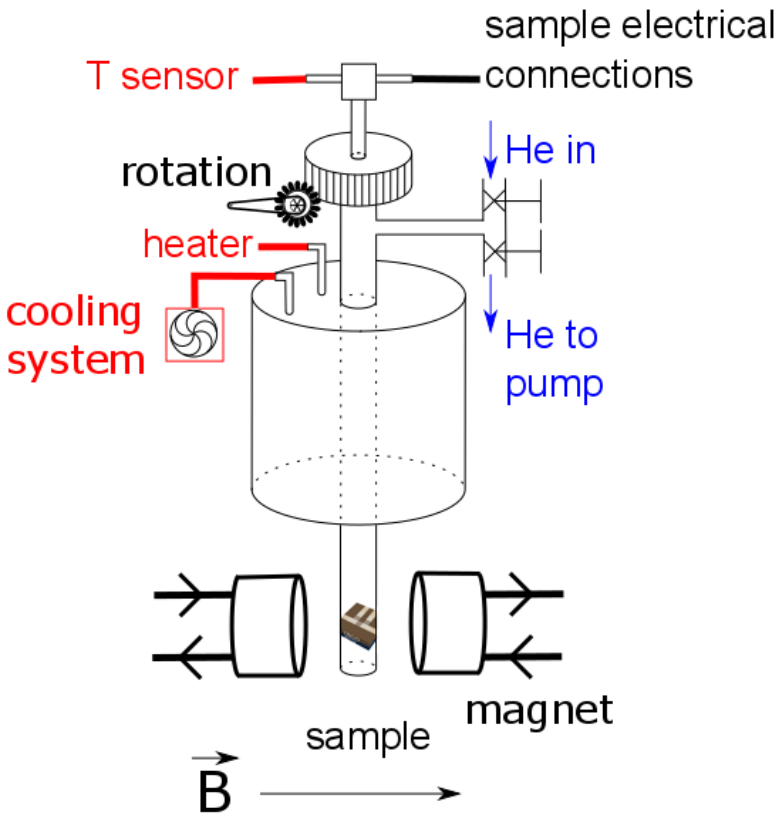

Figure A.1 – Experimental set-up we use to study electronic transport. A cryostat is cooled down up to 3.2 K by a cryocooler. The temperature is stabilized by two heaters. Two coils outside the cryostat and a magnetic field sensor allow to stabilize the magnetic field from 0 Oe to 9000 Oe in "garfield". A motor and a cogwheel can rotate the sample from 0° to 360° with respect to the vertical direction.

An electromagnet made of two water-cooled coils surround the cryostat tube, the elec-

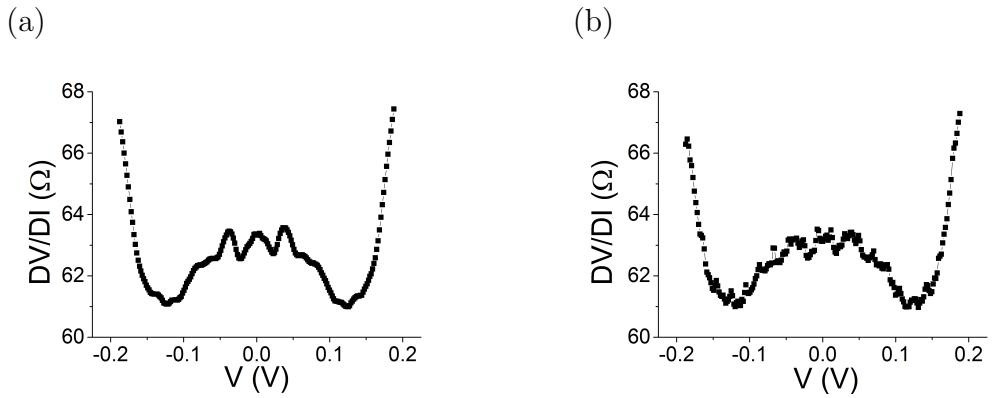

Figure A.2 – Comparison of two methods to measure experimentally the differential resistance of a device. The measured sample is a YBCO graphene junction. (a) $\partial V/\partial I$ measured in the Keithley delta mode. (b) $\partial V/\partial I$ calculated numerically by differentiating the I(V) curve from the same measurement. The two signals are similar but the noise is reduced in the delta mode.

tromagnet is the 3472-70 model from GMW associate. This magnet allows to apply up to 9 000 Oe in or out of plane. A mechanical motor can rotate the sample up to 360 °. The field stabilization with a feedback loop reach a field precision of about ± 10 Oe. This stabilization could be improved either by pushing aside the coil or by changing the current amplifier [1].

The temperature is controlled by the Lake Shore 336 temperature controller via two heaters inside the cryostat. The base temperature the system can reach is about 3.2 K. A feedback loop allows to tune the temperature continuously from 3.2 K to 300 K with a precision about 0.01 K. Both the compressor and the heater are computer controlled via Labview programs.

Two cables containing each 10 wires allow to connect the sample to the electrical apparatus. We use gold wires to connect the sample to the measuring chip. Aluminium wires tend to deoxygenate the YBCO under the contact. This loss of oxygen turns the YBCO into an insulator and the device is not measurable anymore.

The gate voltage is controlled by a Keithley 2450 Source meter. We limit the leakage current to 1 μA such that even if the gate is leaking, the leakage current will not damage the sample. The source allows to impose up to 200 V when the interlock is ON. We always shorten the gate wire before connecting them to our sample since residual tension might be present if the source meter does not receive an instruction.
To perform superconducting junction spectroscopy, we usually measure the differential conductance of our devices. We measure the sample differential conductance using the delta mode from the Keithley 6220 current source and the Keithley 2182-A nanovoltmeter. The

[1] Another experiment in our lab uses the same electromagnet at room temperature. They got around the magnetic field noise by controlling directly the current with an external current source without a feedback loop.

two apparatus are connected by an RS 232 cable which allow the current source to calculate directly the differential conductance through the formula:

$$\frac{dV}{dI}(I_0) = \frac{V(I_0 + \delta I) - 2V(I_0) + V(I_0 - \delta I)}{4\ \delta I}.$$

As shown on figure A.2, this reduces the noise in the differential conductance compared to the numerical derivative of the IV characteristic. The current source is connected to the sample via a triax cable. The voltmeter is connected to the sample via a Keithley cable (2107-4). A homemade box makes the connection between this cables and the cables going into the cryostat, they allow to choose which contact on the device are used for the different purposes (voltage measurement, gate, current source).

B – Lithographic recipes

Lithography is a process in which resist is patterned into a desired shape on a substrate in order to serve as a mask either for substrate etching or for material deposition. We use lithography for different purposes. We use it to etch specific parts of a material, for example to pattern graphene with a plasma, or to remove gold with ion beam etching. We also use a lithographic process to deposit metallic electrodes onto the sample, for example gold electrodes on the graphene to fabricate a Hall bar. The resists used in lithography are either sensitive to UV-light as in optical and laser lithography or they are sensitive to electrons as in electron beam lithography.

The recipes for the different lithography used in this thesis are given in the table B.1. Metallic deposition on graphene for the Hall bar or BSCCO flakes is facilitated when the resist has inward inclined borders. For material etching by plasma or ion beam etching, the resist border are straight. The inclined borders allow to remove only the metal on top of the resist and not the metal on top of the substrate with a pipette in acetone. The inclined resist borders are obtained by hardening the upper part of the resist in chlorobenzene for 12 minutes, such that the resist upper part is less solvable in the developer than the resist lower part.

	border removal	resist	spin coating	heating	exposure time	developer time	ionic scouring
YBCO	yes	SPR	4000 rpm 30 s	90°C 60 s	10 s	MF319 15 s	no
graphene	no	SPR	4000 rpm 30 s	90°C 60 s	10 s	MF319 40 s	no
top gate	no	PMMA	4000 rpm 30 s	100°C 120 s		MIBK 45 s	no
Hall bar graphene	no	SPR	6000 rpm 30 s	95°C 60 s	10 s	MF319 40 s	no
Hall bar electrodes	no	SPR	6000 rpm 30 s	110°C 60 s	10 s	MF319 20 s	yes
BSCCO	no	SPR	4000 rpm 30 s	95°C 60 s		MFCD26 45 s	yes

Table B.1 – Parameters used for the different lithographies.

C – McMillan-Rowell resonance equations

We review the McMillan-Rowell oscillation periodicity in the following. In the McMillan-Rowell process, an electron of wave vector k_e crosses the normal part, it is Andreev reflected as a hole of wave vector k_h on the superconducting side, it crosses the normal part, it is reflected as a hole on the other side, it crosses the normal part, it is Andreev reflected on the superconducting side as an electron, it crosses the normal part, it is reflected as an electron on the other side and it can then interfere with the initial incoming electron. The phase accumulated by the electrons on the path is $2k_e d$, and the phase accumulated by the holes on the path is $-2k_h d$. The excitations energy in the normal metal are small compared to the Fermi energy such that:

$$\begin{aligned} E_e &= \frac{\hbar^2(k_F + k_e)^2}{2m}, \\ E_e &\sim \frac{\hbar^2 k_F^2}{2m} + \frac{\hbar^2 k_F k_e}{m}, \\ E_e &\sim \hbar v_F k_F/2 + \hbar v_F k_e. \end{aligned}$$

In the same way for a hole,

$$E_h \sim -\hbar v_F k_F/2 - \hbar v_F k_h.$$

Hence,

$$\begin{aligned} \varphi &= |k_e - k_h| 2d, \\ \varphi &= \frac{4dE}{\hbar v_F}. \end{aligned}$$

This expression is modified when the McMillan-Rowell resonances occur in a normal metal between two superconductors. In that situation, the electron crosses the normal material, it is Andreev reflected on one superconductor as a hole, the hole crosses the normal material, it is then Andreev reflected as an electron on the other superconductor and it can then interfere with the initial incident electron. The phase accumulated by the electron on its path is the $k_e d$ and the phase accumulated by the hole on its path is then $-k_h d$. Hence,

$$\begin{aligned} \varphi &= |k_e - k_h| d, \\ \varphi &= \frac{2dE}{\hbar v_F}. \end{aligned}$$

Because graphene dispersion relation is linear, the equations describing McMillan-Rowell oscillations are the same:

$$E_{e/h} = \pm \hbar v_F (k_F + k_{e/h}),$$

thus

$$\begin{aligned} \varphi &= |k_e - k_h| d, \\ \varphi &= \frac{2dE}{\hbar v_F}, \end{aligned}$$

and the oscillation period is given by

$$\Delta E = \frac{h v_F}{2d}.$$

David Perconte **8 mars 2018**

Sujet : Effet de proximité entre un supraconducteur à haute température critique et du graphene

Résumé : Nous avons fabriqué des jonctions YBCO graphène, nous avons étudié dans un premier temps le transport électronique à l'interface entre ces deux matériaux ainsi que le mécanisme - la réflexion d'Andreev - par lequel un courant porté par des électrons est transformé en courant par des paires de Cooper. Nous avons observé des interférences électroniques en fonction du niveau de dopage du graphène. Ces interférences correspondent au tunneling de Klein d'électrons normaux quand l'énergie de ces électrons dépassent le gap supraconducteur. A plus basse énergie, ce sont les paires de Cooper qui passent la barrière par effet tunnel de Klein. Dans un deuxième temps, nous avons fabriqué des jonctions YBCO graphène dont la taille est comparable à la longueur de cohérence du graphène. Nous avons observé d'une part un comportement tunnel de la conductance dans le cas où l'interface graphène YBCO est sale. Dans le cas où l'interface YBCO graphène est propre, nous avons observé des oscillations de la conductance de la jonction en fonction de la tension de biais ainsi que de la tension de grille. Ces oscillations semblent provenir d'interférences électroniques dans le canal de graphène entre les électrodes supraconductrices. Enfin, nous présentons une nouvelle méthode de fabrication de jonction π à base de BSCCO.

Mots clés : Supraconducteur, graphene, tunneling de Klein, interférences électroniques

Subject : Proximity effect between a high temperature superconductor and graphene

Abstract: We have fabricated YBCO graphene junction. We studied the electronical transport at the interface between these two materials as well as the mechanism - the Andreev reflexion- by which a current carried by electrons is transformed into a current carried by Cooper pairs. We observed electronic interferences as a function of graphene doping. This modulation comes from the presence of a potential barrier at the interface between YBCO and graphene in which the particles are circulating before being transmitted or reflected. These interferences correspond to Klein tunneling of normal electrons when their energy is higher than the superconducting gap. At lower energy, Cooper pairs can traverse the barrier by Klein tunneling. We later fabricated YBCO graphene junctions which size is comparable to the graphene coherence length. We observed tunnel conductance when the interface between graphene and YBCO is opaque. In the case when the interface is transparent, we observed oscillations of the junction conductance as a function of the bias voltage and of the gate voltage. These oscillations seem to originate from electronic interferences inside the graphene channel between the superconducting electrodes. We also propose an experimental method to fabricate ϕ junction based on BSCCO.

Keywords : Superconductor, graphene, Klein tunneling, electronic interferences